Exploring Electron and Phonon Transport at the Nanoscale for Thermoelectric Energy Conversion

by

Austin Jerome Minnich

Submitted to the Department of Mechanical Engineering
in partial fulfillment of the requirements for the degree of

Doctor of Philosophy

at the

MASSACHUSETTS INSTITUTE OF TECHNOLOGY

June 2011

Author .....
Department of Mechanical Engineering
May 20, 2011

Certified by .....
Gang Chen
Carl Richard Soderberg Professor of Power Engineering
Thesis Supervisor

Accepted by .....
David E. Hardt
Chairman, Department Committee on Graduate Students

Exploring Electron and Phonon Transport at the Nanoscale for Thermoelectric Energy Conversion

by

Austin Jerome Minnich

Submitted to the Department of Mechanical Engineering
on May 20, 2011, in partial fulfillment of the
requirements for the degree of
Doctor of Philosophy

Abstract

Thermoelectric materials are capable of solid-state direct heat to electricity energy conversion and are ideal for waste heat recovery applications due to their simplicity, reliability, and lack of environmentally harmful working fluids. Recently, nanostructured thermoelectrics have demonstrated remarkably enhanced energy conversion efficiencies, primarily due to a reduction in lattice thermal conductivity. Despite these advances, much remains unknown about heat transport in these materials, and further efficiency improvements will require a detailed understanding of how the heat carriers, electrons and phonons, are affected by nanostructures.

To elucidate these processes, in this thesis we investigate nanoscale transport using both modeling and experiment. The first portion of the thesis studies how electrons and phonons are affected by grain boundaries in nanocomposite thermoelectric materials, where the grain sizes are smaller than mean free paths (MFPs). We use the Boltzmann transport equation (BTE) and a new grain boundary scattering model to understand how thermoelectric properties are affected in nanocomposites, as well as to identify strategies which could lead to more efficient materials.

The second portion of the thesis focuses on determining how to more directly measure heat carrier properties like frequency-dependent MFPs. Knowledge of phonon MFPs is crucial to understanding and engineering nanoscale transport, yet MFPs are largely unknown even for bulk materials and few experimental techniques exist to measure them. We show that performing macroscopic measurements cannot reveal the MFPs; instead, we must study transport at the scales of the MFPs, in the quasi-ballistic transport regime. To investigate transport at these small length scales, we first numerically solve the frequency-dependent phonon BTE, which is valid even in the absence of local thermal equilibrium, unlike heat diffusion theory. Next, we introduce a novel thermal conductivity spectroscopy technique which can measure MFP distributions over a wide range of length scales and materials using observations of quasi-ballistic heat transfer in a pump-probe experiment. By observing the changes in thermal resistance as a heated area size is systematically varied, the thermal conductivity contributions from different MFP phonons can be determined. We present

the first experimental measurements of the MFP distribution in silicon at cryogenic temperatures.

Finally, we develop a modification of this technique which permits us to study transport at scales much smaller than the diffraction limit of approximately one micron. It is important to access these length scales as many technologically relevant materials like thermoelectrics have MFPs in the deep submicron regime. To beat the diffraction limit, we use electron-beam lithography to pattern metallic nanodot arrays with diameters in the hundreds of nanometers range. Because the effective length scale for heat transfer is the dot diameter rather than the optical beam diameter, we are able to study nanoscale heat transfer while still achieving ultrafast time resolution. We demonstrate the modified technique by measuring the MFP distribution in sapphire. Considering the crucial importance of the knowledge of MFPs to understanding and engineering nanoscale transport, we expect these newly developed techniques to be useful for a variety of energy applications, particularly for thermoelectrics, as well as for gaining a fundamental understanding of nanoscale heat transport.

Thesis Supervisor: Gang Chen
Title: Carl Richard Soderberg Professor of Power Engineering

Acknowledgments

Many theses' acknowledgements begin with a statement like, "This thesis could not have been completed without..." Having just finished this thesis, I can confirm that this statement, while cliché, is absolutely true. Without the help of many people I would not have been able to complete my thesis, and I'd like to gratefully acknowledge their help here.

First, I would like to thank my advisor, Professor Gang Chen. I am very fortunate to have been able to work for Gang. He routinely goes above and beyond what is expected of an advisor, from meeting with students as often as they like, to reading drafts of papers quickly and giving insightful suggestions, to teaching students how to give a good presentation. I am particularly thankful to Gang for helping me to develop as an independent researcher by giving me almost complete freedom to choose my research topics. Without his help, I would not have been able to secure a faculty position straight from graduate school.

Next, I'd like to thank my thesis committee members, Millie Dresselhaus, Keith Nelson, and Evelyn Wang. All took significant amounts of time to give me advice on my research and career paths, as well as to write reference letters for my faculty applications. I'm particularly grateful to Millie for her quick response time and helpful comments on the several papers we have written together over the years. Keith, and members of his lab, have been great collaborators, and they have provided very useful insight into my work with ballistic transport and ultrafast experiments. I am also grateful to Evelyn for sharing her perspective as a young faculty member with me.

I'd like to thank several former members of the NanoEngineering group: Qing Hao, Sheng Shen, and Aaron Schmidt. Qing Hao and Sheng Shen were extremely helpful and kind to me when I first arrived in the group in 2006. Qing taught me much of what I know about the practical details of running experiments. Sheng was my officemate for three years and remains a great friend. Aaron and I started working together two years after I arrived in the group, when I was learning to use the pump-probe system. From the beginning, Aaron was very patient and spent quite a lot

of time teaching me how to use the system. After he returned to Boston following his postdoc, he again spent a significant amount of time helping us fix the system so that we could take reliable data. In particular, the silicon measurements of chapter 5 could not have been acquired without his help. Qing, Sheng, and Aaron will make excellent professors and I very much look forward to working with them again as a colleague.

I am very lucky to work with a great group of people, the NanoEngineering group of MIT. The collegial atmosphere in our group made life at MIT much more enjoyable. My labmates were also a great resource, and I greatly benefitted from the communication and collaboration with them.

I am happy to have worked with two members of Keith Nelson's group, Jeremy Johnson and Alexei Maznev. I have really enjoyed discussing our joint work and know that the quality of my work is higher because of my interaction with them.

I'd like to thank Kurt Broderick, a staff member at MTL; and Mark Mondol, who runs the electron-beam lithography machine at MIT. Both provided invaluable help in fabricating samples.

I'm grateful to the Department of Defense and the National Science Foundation for their financial support of my PhD.

I am really lucky to have had a great group of friends during my time at MIT. Their presence made my time here much more meaningful and enjoyable. In particular I'd like to acknowledge my very close friends Josh Taylor, Allison Beese, Priam Pillai, Eerik Hantsoo, Matthew Branham, Kit Werley, Janice Cho, Albert Leung, and Jack Chu. I will really miss them as we all head out of Boston.

Finally, I am very grateful for my wonderful fiancée, Song Yi Kim, and my family members. There were many times during my PhD when I felt so discouraged and frustrated that I wasn't sure I was capable of finishing. During these times, the encouragement and support of my family was really what kept me going and ultimately enabled me to succeed. I am particularly indebted to Song Yi, and my mom, dad, and sister, for their love and support.

Contents

List of Figures

List of Tables

Chapter 1

Introduction

1.1 Nanoscale heat transfer and thermoelectrics

Nanoscale heat transfer, where energy is transported over scales comparable to the heat carrier wavelengths and mean free paths (MFPs), is a topic of considerable interest.[1–7] Transport at these fundamental length scales can deviate strongly from the predictions of diffusion theory,[8,9] and materials structured at these length scales have demonstrated properties that are unachievable in bulk materials.[10–17] These materials have applications in all areas of the energy field, from solar photovoltaics to thermoelectric waste heat recovery to batteries, to name just a few.

Thermoelectric energy conversion is one technology that has benefited significantly from the proper application of these nanoscale effects. Thermoelectrics are capable of converting heat directly into electricity, and can also act as solid state refrigerators or heat pumps which do not use any moving parts or environmentally harmful fluids.[2,18–23] Because of their reliability and simplicity they are used extensively in fields such as space power generation and a variety of cooling applications.[24] While their low efficiency compared to that of mechanical cycles presently restricts their applications, there is a considerable interest in applying newly developed materials to waste heat recovery applications in cars or industry.[24,25] This could make a sizeable contribution to solving the energy challenge as over two-thirds of the energy presently produced is rejected as waste heat,[26] corresponding to almost 26 million barrels of oil

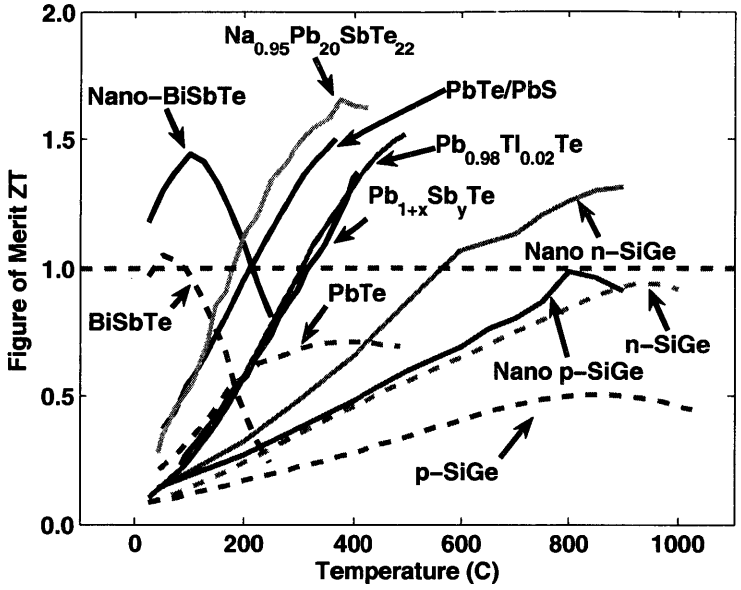

Figure 1-1: Figure of merit ZT of current state of the art thermoelectric materials versus temperature. The dashed lines show the maximum ZT values for bulk state of the art materials, and the solid lines show recently reported ZT values, many of which were obtained in bulk nanostructured materials. (From Ref. [23]. Material properties: BiSbTe, Ref. [14]; $Na_{0.95}Pb_{20}SbTe_{22}$, Ref. [31]; PbTe/PbS, Ref. [32]; $Pb_{0.98}Tl_{0.02}Te$, Ref. [33]; $Pb_{1+x}Sb_yTe$, Ref. [34]; n-SiGe, Ref. [16]; p-SiGe, Ref. [17]).

per day. There is also interest in using thermoelectrics for solar thermal applications, where solar energy is used to create a temperature difference across a thermoelectric material.[27–30]

The energy conversion efficiency of a thermoelectric material is determined by the figure of merit $ZT = S^2\sigma T/k$, where S is the Seebeck coefficient, or the voltage generated per unit temperature difference, σ is the electrical conductivity, k is the thermal conductivity, and T is the absolute temperature at which the properties are measured.[18,19] To obtain a high energy conversion efficiency, we want ZT as high as possible, meaning the material should possess a high electrical conductivity, high Seebeck coefficient, and low thermal conductivity.

These material properties do not often occur in nature. Metals have very high electrical conductivity but also very high thermal conductivity. Glasses are the opposite, having very low thermal conductivity but also very low electrical conductivity.

The best materials turn out to be heavily doped alloyed semiconductors, which have low thermal conductivity but electrical properties that can be partially tuned by doping.[18] However, the thermoelectric properties are highly interdependent, so that changing one property results in an adverse change in the other two properties so that ZT remains constant.

Nanostructuring allows this coupling to be partially broken. In nanostructured materials, numerous interfaces are able to scatter heat-carrying phonons, or lattice vibrations, so that the thermal conductivity is reduced significantly while electrical properties are minimally affected. Indeed, remarkably low thermal conductivities in nanostructures such as nanowires, superlattices, and nanocomposites have recently been reported.[13,14,35,36] Increases in the figure of merit have been reported in some of these materials, including superlattices,[10] quantum dots,[11] nanowires,[12,13] and nanocomposites.[14–17] Some of the reports made in recent years are shown in Fig. 1-1. Many different material systems exhibit enhanced figures of merit, and most have broken the ZT $\approx$ 1 barrier which was previously the maximum ZT of any material for over fifty years.

1.2 Outline of the thesis

Despite these advances, much remains unknown concerning the precise mechanisms by which the heat carriers in thermoelectric materials, electrons and phonons, are affected by nanostructures. For electrons, the primary challenge is to understand how electrically charged defects such as grain boundaries scatter electrons and alter the electrical conductivity and Seebeck coefficient. While grain boundaries in technologically important materials such as silicon have been extensively studied,[37–40] the magnitude of the grain boundary potential as well as the energy dependence of the potential are essentially unknown in nanostructured thermoelectrics.

For phonons, the challenges are even greater because we still do not know basic quantities like phonon MFPs even in bulk materials. Our basic understanding of phonon transport is still based on simple relaxation time models which were developed

50 years ago.[41,42] The ability to engineer new materials at the nanoscale thus requires a more complete knowledge of the basic physics of phonon transport.

The purpose of this thesis is to explore the physics of nanoscale transport in thermoelectric materials and to determine how we can use nanoscale effects to engineer more efficient thermoelectric devices. Chapter 2 studies electron and phonon transport in nanocomposite thermoelectric materials. We use modeling and materials characterization to understand how carriers are affected by grain boundaries in materials where the grain sizes are smaller than mean free paths (MFPs). We develop a model to calculate the electrical and thermal transport properties of bulk and nanocomposite thermoelectric materials using the Boltzmann transport equation (BTE). By incorporating a new grain boundary scattering model we are able to explain how the thermoelectric properties are affected in nanocomposites as well as to identify strategies which could lead to more efficient thermoelectric materials.

These types of nanoscale scattering models, while useful, cannot directly provide information about how heat carriers are affected by nanostructures. The second portion of the thesis focuses on determining how to more directly measure properties of the heat carriers like the phonon MFP distribution. In chapter 3, we show that in order to extract this information it is not sufficient to simply measure macroscopic transport properties; we must study transport at the length scales of the heat carriers themselves. In the quasi-ballistic regime, where transport occurs over scales comparable to heat carrier MFPs, diffusion theory becomes invalid due to a loss of local thermal equilibrium. The manner in which the transport deviates from diffusion theory reveals very useful information about the underlying heat carrier distribution. To explore this concept, in this chapter we numerically solve the frequency-dependent phonon Boltzmann transport equation, which is valid over length and time scales smaller than the phonon MFPs and relaxation times, respectively, unlike Fourier's law. These numerical results confirm that by studying the quasi-ballistic regime, we should be able to extract information about phonon relaxation times and MFPs.

The rest of the thesis focuses on experimentally measuring MFPs using our ultrafast pump-probe experiment in the Rosenhow-Kendall laboratory. Chapter 4 briefly

discusses the modifications that were made to the system to make it more stable, robust, and automated. These modification greatly simplify the task of data collection.

In chapter 5, we introduce a new technique to measure MFP distributions. By observing the changes in thermal resistance as a heated area size is systematically varied, the thermal conductivity contributions from different MFP phonons can be determined. Using this technique, we measure the MFP distribution of phonons in silicon for the first time, obtaining good agreement with first-principles calculations.

In chapter 6, we develop a modification of this technique which permits us to study transport at scales smaller than the diffraction limit of approximately 1 micron, which is the smallest length scale that can be typically achieved optically. This is important as many technologically relevant materials like thermoelectrics have MFPs in the deep submicron regime. To access these length scales, we use electron-beam lithography to pattern nanoscale metal absorbers with diameters down to tens of nanometers. By using these nanoscale absorbers as heaters, we are able to investigate phonon transport in a larger range of materials and length scales. We apply this technique to measure the MFP distribution in sapphire. The spectrally resolved information which can be determined using our technique is extremely useful both fundamentally and for technological applications which involve nanoscale transport.

Finally, chapter 7 examines possibilities for future work and concludes the thesis.

Chapter 2

Carrier transport in thermoelectric nanocomposites

2.1 Background

The first topic we consider is electron and phonon transport in nanocomposites. The term "nanocomposite" has been used to describe several different types of structures. The original concept was for either nanoparticles embedded in a host or a heterostructure geometry with nanoparticles of different materials adjacent to each other.[43,44] For the heterostructure geometry, when the two materials are the same, the nanocomposite is essentially a material with nanometer sized grains. Because the structures in the material have dimensions typically in the tens to hundreds of nanometers, length scales can be smaller than carrier mean free paths, resulting in modified transport properties compared to those of the bulk material.

Nanocomposite thermoelectric materials, which we also call nanocomposites for simplicity, have attracted much attention recently due to experimental demonstrations of improved thermoelectric properties over those of the corresponding bulk material.[14–17,31,32,45,46] These materials have an important advantage over other nanostructured materials in that they can be produced in large quantities and in a form that is compatible with existing thermoelectric device configurations. The primary mechanism that leads to ZT improvement is a reduction in lattice thermal conduc-

tivity due to additional phonon scattering at grain boundaries. However, a potential barrier which forms at the grain boundary (GB) leads to a reduced electrical conductivity but possibly higher Seebeck coefficient. Nanocomposites are commonly created using either a ball milling and hot pressing technique[14–17] or with thermal processing methods.[31,32,45,46]

$Si_{0.8}Ge_{0.2}$ nanocomposites with improved thermoelectric properties over those of the bulk were recently reported.[16,17] To better understand the reported data and to gain insight into the carrier transport in these materials, we calculate the thermoelectric properties of these materials using the Boltzmann transport equation (BTE). To perform the calculation for the complex nanostructured material, we split the computation into two easier parts: first, calculating the properties of the bulk material; second, adding to this calculation a GB scattering rate which accounts for the additional nanoscale scattering.

For the first task, fortunately the theory for modeling bulk thermoelectric materials using the BTE is well developed and the calculation is straightforward. If the relaxation time approximation can be used, the thermoelectric properties can be expressed as integrals of a relaxation time;[47–49] standard expressions for the relaxation time of various scattering mechanisms are given in the literature.[48–50] For the cases that we study here the relaxation time approach is a good approximation. A similar approach was taken by Vining[51] and Slack and Hussain,[52] and we follow their work closely with a few important exceptions which will be described later.

For the second task, we need to obtain an additional relaxation time τ_{GB} (or equivalently a scattering rate τ_{GB}^{-1}) to account for the strong GB scattering mechanism in these materials. Once determined, this scattering rate can be added to the other scattering rates using Matthiessen's rule and the thermoelectric properties are calculated in the usual manner.

GB scattering has been of great interest, particularly for device applications involving polycrystalline silicon. Mayadas and Shatzkes obtained a scattering rate from a series of delta function potentials.[53] Their model is commonly used to calculate the resistivity of polycrystalline materials. We will show that this model is

not physically consistent for thermoelectric materials. Many other models for grain boundary scattering in polycrystalline materials attempt to obtain I-V characteristics by considering thermionic field emission and tunneling processes.[37–40] However, this framework neglects the energy relaxation of charge carriers and can result in unrealistically large Seebeck coefficients, especially in nanocomposites. For this reason, we focus on calculating GB scattering rates, allowing all the properties to be determined in a self-consistent manner.

The organization of chapter 2 is as follows. First, in Section 2.2, the basic theory of calculating thermoelectric properties using the Boltzmann equation is briefly discussed. In Section 2.3, the code which implements this calculation is validated by calculating the thermoelectric properties of bulk $Si_{1-x}Ge_x$ alloys and comparing the results to experimental data. Section 2.4 introduces models for phonon and electron GB scattering. We apply the models to $Si_{0.8}Ge_{0.2}$ nanocomposites in Section 2.5 and compare the results to recently reported experimental data[16,17] and new mobility measurements. Finally, in Section 2.6, we use the model's predictions to help determine which strategies will be most effective in further improving the figure of merit in these materials.

2.2 Theory

The thermoelectric properties of $Si_{1-x}Ge_x$ can be calculated using the BTE. If all the scattering mechanisms are elastic, the relaxation time approximation (RTA) may be employed, thereby simplifying the solution.[48–50,54] If some scattering mechanisms are inelastic, then a relaxation time cannot be strictly defined. For $Si_{1-x}Ge_x$, the only inelastic scattering mechanism is due to optical phonons, where the interaction energy $\hbar\omega_{op}$, ω_{op} being the optical phonon frequency, is on the order of k_BT at room temperature. Fortunately, for practical use of $Si_{1-x}Ge_x$ we are mostly interested in much higher temperature ranges at which optical phonon scattering can be considered approximately elastic, and we may use the RTA for our calculations.

A similar approach to calculate the thermoelectric properties of bulk materials

was originally performed by several authors,[51,52] and we follow their work closely but with important exceptions. The common calculations are as follow. First, like Slack,[52] we assume three band transport, using two conduction bands, one near the X point and one at the L point; and one effective valence band. We find the L conduction band does not contribute substantially to the transport properties. Second, like Vining,[51] we take into account the exact form of the relaxation times from the literature.[48,49,51,55] Slack uses an effective relaxation time exponent or empirical results in his model.

We differ from the authors' calculations in the following ways. The first difference is that we do not assume that the conduction bands and valence bands have the same band structure parameters; rather, we use literature values for most key quantities such as the conduction band effective mass and deformation potential. These values and any adjustments made are listed in Appendix A.

The second difference is that we take into account the non-parabolicity of the X conduction band, which strongly affects the thermoelectric properties at high n-type doping concentrations.[49] Vining and Slack did not take non-parabolicity into account, and while they were able to fit most of the data, unphysical values of some fitting parameters were required, or an empirical result was used to obtain agreement. By using a non-parabolic formulation we are able to explain experimental data over the entire doping concentration range with only minor adjustments to the literature values of the band structure parameters.

Another important difference is the treatment of dopant precipitation issues in $Si_{1-x}Ge_x$. As discussed by many authors,[51,52,56–58] $Si_{1-x}Ge_x$ alloys used for thermoelectrics, which are usually doped with P (n-type) or B (p-type), are often doped beyond the solubility point for the dopant, causing the carrier concentration to vary with temperature as dopants precipitate out at lower temperatures and become reactivated at higher temperature. These processes can change the carrier concentration by a factor of two or more over the entire temperature range, significantly affecting the observed transport properties. This effect is especially pronounced for P in $Si_{1-x}Ge_x$, which has a strong tendency to precipitate at grain boundaries.[51] Furthermore, in

many cases the carrier concentration depends on the thermal history of the sample, making it even more difficult to compare results because the properties of the nominally same material at the same temperature might not be equal due to differences in thermal processing. We have observed this phenomenon in our measurements: because the mobility is measured using a different system than that used for the reported measurements of electrical conductivity and Seebeck coefficient, the samples are subjected to different heat treatments and thus the electrical conductivities measured by different systems are not equal. While Vining was forced to fit the chemical potential at each temperature to account for this variation, we are able to estimate the change in carrier concentration versus temperature during the electrical conductivity and Seebeck coefficient measurement using the previously reported electrical conductivity measurements,[16,17] new mobility measurements, and model calculations. This procedure simply uses the definition of conductivity $\sigma = ne\mu$ to estimate $n(T)$. It is necessary to assume one band transport for this procedure; we find this to be a valid assumption for the cases studied here. For the n-type case, where the mobility has a stronger dependence on the carrier concentration, an iterative procedure is used to ensure self-consistency between all the properties.

A final point to mention before discussing the details of the calculation is the difficulty in accurately modeling transport in p-type $Si_{1-x}Ge_x$ using the Boltzmann equation. The warped energy surface of the heavy hole band, along with interactions from the split-off band (which is only 0.044 eV away from the valence band edge), causes the parabolic energy surface approximation to be poor at high doping levels. While it is sometimes possible to obtain a reasonable fit to the data, the quality of the fit is often worse than that of n-type $Si_{1-x}Ge_x$, and for the p-type nanocomposite no satisfactory fit could be found. The valence band parameters used in the calculation are listed in Appendix A.

2.2.1 Relaxation time approximation

We now discuss the details of the theory necessary to model bulk thermoelectric materials. A detailed derivation of these results is given in Ref. [59]. In a bulk

material, under the RTA the electrical current J and heat current J_q carried by charge carriers can be written as:[47]

$$J = L_{11}\left(-\frac{d\Phi}{dx}\right) + L_{12}\left(-\frac{dT}{dx}\right) \tag{2.1}$$

$$\begin{aligned} J_q &= L_{21}\left(-\frac{d\Phi}{dx}\right) + L_{22}\left(-\frac{dT}{dx}\right) \\ &= \frac{L_{21}}{L_{11}}J + \left(L_{22} - \frac{L_{12}L_{21}}{L_{11}}\right)\left(-\frac{dT}{dx}\right) \end{aligned} \tag{2.2}$$

where Φ is the electrochemical potential. The coefficients are given by:

$$L_{11} = \frac{e^2}{3}\int_0^\infty \tau(E)v^2\left(-\frac{\partial f_0}{\partial E}\right)D(E)dE \tag{2.3}$$

$$L_{12} = -\frac{e}{3T}\int_0^\infty \tau(E)v^2\left(-\frac{\partial f_0}{\partial E}\right)(E-E_f)D(E)dE \tag{2.4}$$

$$L_{21} = -\frac{e}{3}\int_0^\infty \tau(E)v^2\left(-\frac{\partial f_0}{\partial E}\right)(E-E_f)D(E)dE \tag{2.5}$$

$$L_{22} = \frac{e}{3T}\int_0^\infty \tau(E)v^2\left(-\frac{\partial f_0}{\partial E}\right)(E-E_f)^2D(E)dE \tag{2.6}$$

Here E is the energy, $D(E)$ is the density of states, $f_o = (\exp((E-E_f)/k_BT)+1)^{-1}$ is the Fermi-Dirac distribution, e is the absolute value of the charge of an electron, v is the electron group velocity, $\tau(E)$ is the relaxation time, and E_f is the Fermi level. Note that it is essential to use the Fermi distribution rather than the Boltzmann distribution as thermoelectrics have a very high doping level and are usually degenerate. We can identify the electrical conductivity, the Seebeck coefficient, and the electronic contribution to the thermal conductivity as:

$$\sigma = L_{11} \tag{2.7}$$

$$S = -\frac{d\Phi}{dT} = -\frac{d\Phi/dx}{dT/dx} = \frac{L_{12}}{L_{11}} \tag{2.8}$$

$$k_e = L_{22} - \frac{L_{12}L_{21}}{L_{11}} \tag{2.9}$$

We can also calculate the mobility using:

$$\mu = \frac{\sigma}{ne} \tag{2.10}$$

where n is the electron or hole concentration. Thus, under the RTA, the problem of calculating thermoelectric properties reduces to calculating the coefficients L_{ij}.

2.2.2 Additional details

To complete the formulation we need expressions for the density of states $D(E)$ and the electron velocity v, a way to account for multiple band transport, a way to find the Fermi level, and the relaxation time τ. The first two quantities, $D(E)$ and v, can be obtained from the $E(k)$ dispersion relation. To take into account anisotropic, non-parabolic bands we use a two band approximation,[49,50] which modifies the $E(k)$ dispersion relation from the usual parabolic form to:

$$\gamma(E) = E(1 + \alpha E) = \frac{\hbar^2}{2}\left(\frac{k_l^2}{m_l^*} + 2\frac{k_t^2}{m_t^*}\right) \tag{2.11}$$

where m_l^* and m_t^* are the longitudinal and transverse components of the effective mass, respectively, and α is the non-parabolicity coefficient, an adjustable parameter which is approximately $\alpha \approx 1/E_g$, with E_g being the bandgap.[49] The density of states can thus be determined from:

$$D(E) = \frac{k^2}{\pi^2}\frac{dk}{dE} = \frac{1}{2\pi^2}\left(\frac{2m_D^*}{\hbar^2}\right)^{3/2}\gamma^{1/2}\frac{d\gamma}{dE} \tag{2.12}$$

where $m_D^* = N^{2/3}(m_l^* m_t^{*2})^{1/3}$ is the density of states effective mass. Here N is the number of equivalent valleys, and is equal to six for the X conduction band in $Si_{1-x}Ge_x$(the electronic structure of $Si_{1-x}Ge_x$is the same as that of Si for $x < 0.85$).[60] The electron velocity is:

$$v = \frac{1}{\hbar}\nabla_k E = \sqrt{\frac{2}{m_c^*}}\frac{\gamma^{1/2}}{\gamma'} \tag{2.13}$$

where $\gamma' = d\gamma/dE$ and m_c^* is the conductivity mass. For a non-parabolic band the conductivity mass is modified from its usual form as follows:[61]

$$m_c^* = \frac{3Km_t^*}{2K+1} \frac{\int_0^\infty \left(-\frac{\partial f_0}{\partial E}\right)(E+\alpha E^2)^{3/2} D(E) dE}{\int_0^\infty \left(-\frac{\partial f_0}{\partial E}\right)(E+\alpha E^2)^{3/2}(1+2\alpha E)^{-1} D(E) dE} \tag{2.14}$$

where $K = m_l^*/m_t^*$ is the ratio of the longitudinal effective mass to the tranverse effective mass.

Next, we need to account for the presence of multiple bands, including electron and hole bands. Hole bands have the opposite sign of Seebeck coefficient from electrons and thus can strongly affect the overall Seebeck coefficent. Multiple band transport can be incorporated by calculating the contribution from each band and combining the results. The appropriate manner in which to combine the terms is given below:[18,52]

$$\sigma = \sum_i \sigma_i \tag{2.15}$$

$$\mu = \frac{\sum_i \mu_i n_i}{\sum n_i} \tag{2.16}$$

$$S = \frac{\sum_i S_i \sigma_i}{\sum_i \sigma_i} \tag{2.17}$$

$$k_{elec} = \sum_i k_i + \sum_{i \neq j} \frac{\sigma_i \sigma_j}{\sigma_i + \sigma_j} (S_i - S_j)^2 T \tag{2.18}$$

Note the presence of the bipolar thermal conductivity term in Eq. 2.18, which can be appreciable at high temperatures.

To find the Fermi level we use the charge conservation condition.[48,49] The electron concentration in each band is given by:

$$n_{e,i} = \int_0^\infty D(E)(e^{(E-(E_f-E_{c,i})/k_BT} + 1)^{-1} dE \tag{2.19}$$

where i indexes each conduction band and E is measured relative to the conduction band edge for each band. The hole concentration in each band is

$$n_{h,j} = \int_0^\infty D(E)(e^{(E-(E_{v,j}-E_f))/k_BT} + 1)^{-1} dE \tag{2.20}$$

where j indexes each hole band and E is measured relative to the valence band edge for each band. For charge conservation we need any net electrons or holes to be from an impurity. This condition gives

$$N_A^- - N_D^+ = \sum_j n_{h,j} - \sum_i n_{e,i} \tag{2.21}$$

where N_D^+ is the number of ionized donors and N_A^- is the number of ionized acceptors. N_D^+ and N_A^- might not be equal to N_D and N_A if not all the dopants are ionized, but since the ionization energy is small for typical dopants such as B and P the number of ionized donors or acceptors is assumed to equal the number of donor or acceptor atoms, respectively.[62] Equation 2.21 is an implicit equation for E_f which can be solved with a numerical scheme such as the bisection method; once E_f is found the electron and hole concentrations in each band can be determined from Eq. 2.19 and 2.20.

2.2.3 Electron relaxation times

The final quantity needed is the relaxation time, which accounts for the scattering processes in a material. In this paper we will be modeling $Si_{0.8}Ge_{0.2}$ and will incorporate acoustic phonon (AP) scattering, non-polar optical phonon (NPOP) scattering, and ionized impurity scattering (IIS). Note that $Si_{1-x}Ge_x$ is not a polar material and thus polar scattering mechanisms are not applicable. Technically $Si_{1-x}Ge_x$ also has an alloy scattering mechanism, but our calculations show that alloy scattering is weak compared to IIS in these highly doped materials and so is not considered here. Standard forms for the AP and IIS relaxation times are in the literature.[48–50,54,55,63] The relaxation times used here incorporate non-parabolicity. The relaxation time τ_{AP} for AP scattering is:[55]

$$\tau_0^{-1} = \frac{\pi k_B T D_a^2}{\rho v_s^2 \hbar} D(E) \tag{2.22}$$

$$\tau_{AP}^{-1} = \tau_0^{-1} \left\{ \left[1 - \frac{E}{E_g + 2E} \left(1 - \frac{D_v}{D_A} \right) \right]^2 - \frac{8}{3} \frac{E(E_g + E)}{(E_g + 2E)^2} \frac{D_v}{D_A} \right\} \tag{2.23}$$

where E is the energy relative to the band edge, D_a is the conduction band acoustic deformation potential, D_v is the valence band acoustic deformation potential, E_g is the band gap, $D(E)$ is the density of states defined in Eq. 2.12, ρ is the density, and v_s is the sound speed. It is possible to derive other forms for the AP relaxation time which give similar results.[49]

The other phonon scattering mechanism, non-polar optical phonon (NPOP) scattering, is not elastic and it is not possible to strictly define a relaxation time. However, if $k_B T/\hbar\omega_{op} \gg 1$, where ω_{op} is the optical phonon frequency, then the scattering can be considered to be approximately elastic. For NPOP scattering we use an approximation due to Ravich which gives a relaxation time with a form similar to that of AP scattering.[55] The result is:

$$\tau_0^{-1} = \frac{\pi^3 \hbar \left(k_B T\right)^{1/2}}{\rho a^2} \left(\frac{a D_o}{\hbar\omega_{op}}\right)^2 D(E) \tag{2.24}$$

$$\tau_{OP}^{-1} = \tau_0^{-1} \left\{ \left[1 - \frac{E}{E_g + 2E}\left(1 - \frac{D_{vo}}{D_o}\right)\right]^2 - \frac{8}{3}\frac{E(E_g + E)}{(E_g + 2E)^2}\frac{D_{vo}}{D_o} \right\} \tag{2.25}$$

where D_o is the conduction band optical deformation potential (with units J/m), D_{vo} is the valence band optical deformation potential, a is the lattice constant, and the other parameters were defined earlier. The values of the acoustic and optical deformational potentials are listed in Appendix A.

The final scattering mechanism, ionized impurity scattering, has a relaxation time given by the standard Brooks-Herring result:[48,49]

$$\tau^{-1} = \frac{\pi \left(4\pi Z e^2/\varepsilon_0\right)^2}{8\hbar k^4} D\left(E\right) F_{imp} N_D \tag{2.26}$$

$$F_{imp} = \ln\left(1 + \xi\right) - \frac{\xi}{1 + \xi} \tag{2.27}$$

$$\xi = (2kR)^2 \tag{2.28}$$

where Z is the number of charges per impurity, ε_0 is the static dielectric constant, N_D is the doping concentration, k is the magnitude of the electron wavevector, and R is the Debye screening length.[48,49,61,64] In the Thomas-Fermi approximation, R is

given by:[61,64]

$$R^{-2} = \frac{4\pi e^2 Z}{\varepsilon_\infty} \int_0^\infty \left(-\frac{\partial f_0}{\partial E}\right) D(E) dE \tag{2.29}$$

To obtain a total relaxation time for all the scattering mechanisms, we can add the scattering rates τ^{-1} using Matthiessen's rule:[48,49]

$$\tau^{-1} = \sum_i \tau_i^{-1} \tag{2.30}$$

Matthiessen's rule assumes all the scattering mechanisms are independent of each other. The total relaxation time can then be inserted into Eqs. 2.3-2.6 to calculate the thermoelectric properties. This completes the theoretical treatment of electron transport.

2.2.4 Phonon modeling

The final task is to model phonon transport. For this we use Steigmeier and Abeles' model[65] of the lattice thermal conductivity of alloys based on the Callaway model.[41] Their model treats phonons with the Boltzmann equation under the RTA and includes point-defect, phonon-phonon, and phonon-electron scattering mechanisms, all of which are characterized by a relaxation time as was the case for electrons.[65] These relaxation times are used exactly as they are given in Ref. [65] and so are not reproduced here.

Once the relaxation times have been computed, the lattice thermal conductivity can be determined:

$$k_l = \frac{k_B}{2\pi^2 v_s} \left(\frac{k_B \theta_D}{\hbar}\right)^3 (I_1 + I_2^2/I_3) \tag{2.31}$$

where v_s is the sound speed, θ_D is the Debye temperature, and I_1, I_2, and I_3 are given by:

$$I_1 = \int_0^1 \tau x^2 \frac{\alpha^2 x^2 e^{\alpha x}}{(\exp(\alpha x) - 1)^2} dx \tag{2.32}$$

$$I_2 = \beta \int_0^1 \frac{\tau}{\tau_U} x^2 \frac{\alpha^2 x^2 e^{\alpha x}}{(\exp(\alpha x) - 1)^2} dx \tag{2.33}$$

$$I_3 = \beta \int_0^1 \frac{1}{\tau_U} \left(1 - \frac{\beta\tau}{\tau_U}\right) x^2 \frac{\alpha^2 x^2 e^{\alpha x}}{(\exp(\alpha x) - 1)^2} dx \tag{2.34}$$

Here $x = \omega/\omega_D$, where ω_D is the Debye frequency, $\alpha = (\theta_D/T)^n$, where θ_D is the Debye temperature, $n \approx 1$ is a fitting parameter related to higher order phonon scattering, β is the ratio of Umklapp to normal mode scattering, and τ and τ_U are the total and umklapp relaxation times, respectively. The total thermal conductivity is the sum of the lattice thermal conductivity and the electronic thermal conductivity, Eq. 2.9.

2.2.5 Summary of the calculation

We now review the steps necessary to perform the calculation. After specifying band structure parameters, temperature, and doping level, the first step is to calculate the Fermi level. This can be done by calculating n_e and n_h for each band, as in Eqns. 2.19 and 2.20, and combining the result in Eq. 2.21. The equation is now a nonlinear function of the Fermi level E_f. By iteratively solving this equation using the bisection method, we can find E_f and then the equilibrium electron and hole concentrations. The next step is to compute the energy dependent relaxation times and combine them using Matthiessen's rule, Eq. 2.30. Once the total relaxation times are determined, we can compute the coefficients L_{ij} given in Eqns. 2.3-2.6 for each band, and subsequently calculate the properties for each band using Eqns. 2.7-2.9. The overall transport properties, which are the quantities that are measured experimentally, are found from combining the properties for each band, as in Eqns. 2.15-2.18. Finally, the lattice thermal conductivity can be calculated separately using the Callaway model, given in Eqs. 2.31-2.34. This procedure can be repeated for each temperature or doping concentration, allowing all of the thermoelectric properties to be determined over the desired temperature and doping concentration range.

2.3 Model validation

To validate the model, we compare the calculated results to experimental data for bulk $Si_{1-x}Ge_x$ from several sources.[16,17,51,66] The band structure parameters used are listed in Appendix A.

The modeling predictions for bulk n-type $Si_{0.7}Ge_{0.3}$, along with the same data used by Vining for comparison,[51,66] are shown in Fig. 2-1. The calculations match the experimental data to within about 15% over most of the doping concentration and temperature range. The two highest doping concentrations have been increased by about 10% from the reported values; this adjustment is expected to be within the experimental error of the measurement. Some of the important effects discussed earlier can be clearly seen in the model; for example, for the lowest doping concentration the bipolar thermal conductivity is dominant at high temperatures, and is accompanied by a large decrease in Seebeck coefficient. The most highly doped material shows evidence of dopant precipitation above 1000 K, seen as an increase in the electrical conductivity, but this is not accounted for here as the mobility is unknown.

A similar comparison for p-type $Si_{0.7}Ge_{0.3}$, along with data from Dismukes,[66] is shown in Fig. 2-2. The fit is slightly worse than that for the n-type case, particularly the Seebeck coefficient, as this parameter is sensitive to the band structure and is most affected by the failure of the parabolic approximation. At high temperature the Seebeck coefficient is underestimated by about 20% in the worst case. As indicated by the $\times$ symbols in the figure, the accuracy of some of the experimental data is questionable as the maximum ZT value for the highest two doping concentrations is almost $ZT = 0.8$, higher than the expected value of around $0.5 - 0.6$ for state-of-the-art bulk $Si_{0.8}Ge_{0.2}$ shown in Figure 2-4.

We also computed the thermoelectric properties of state of the art n-type and p-type $Si_{0.8}Ge_{0.2}$ alloys,[16,17] shown in Figures 2-3 and 2-4. In this case the carrier concentrations are not available, forcing us to adjust the values to fit the data. The fitted carrier concentrations were determined to be $N_D = 1.7\times10^{20}$ cm^{-3} for n-type and $N_A = 1.4\times10^{20}$ cm^{-3} for p-type. The calculation is again in good agreement

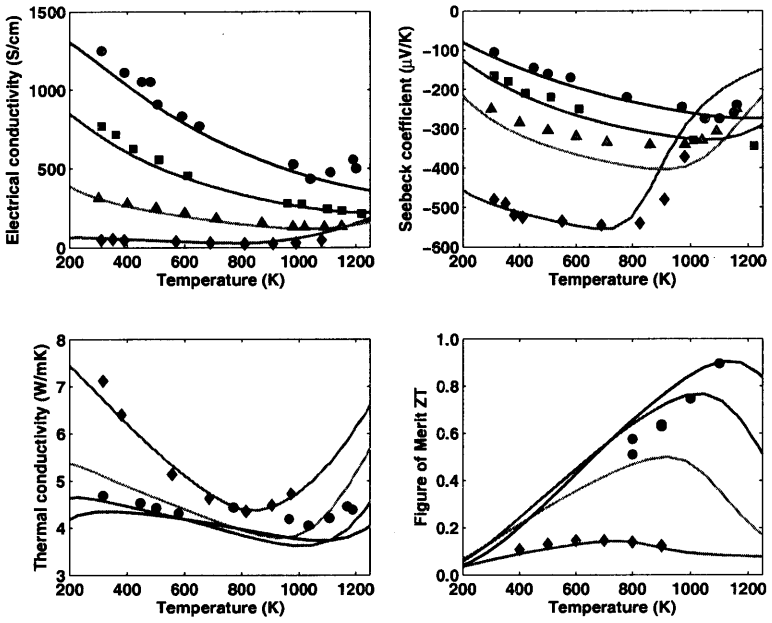

Figure 2-1: Experimental (symbols) and computed (curves) thermoelectric properties of n-type bulk $Si_{0.7}Ge_{0.3}$ (data from Ref. [51]). Doping concentrations ($\times 10^{19}$ cm^{-3}): $\diamond$=0.22; $\triangle$=2.3; $\square$=7.3; $\circ$=17.

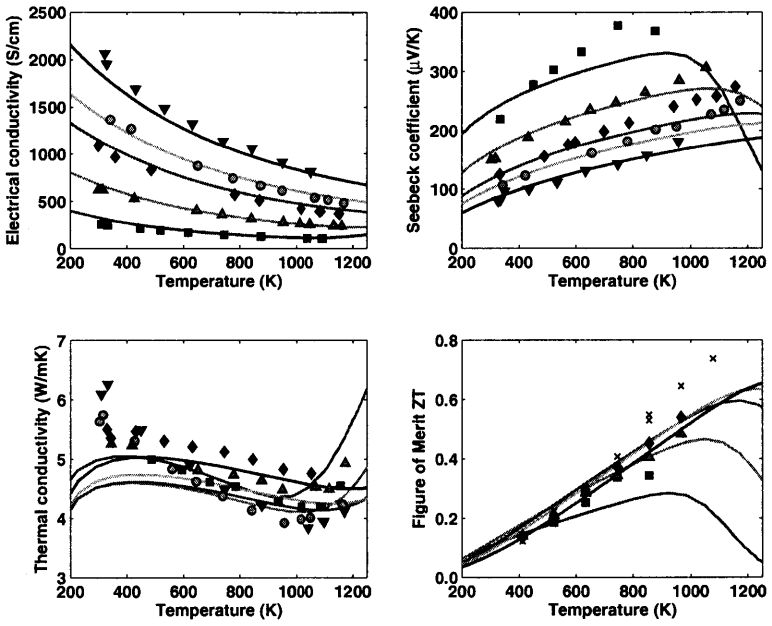

Figure 2-2: Experimental (symbols) and computed (curves) thermoelectric properties of p-type bulk $Si_{0.7}Ge_{0.3}$ (data from Ref. [66]). Doping concentration ($\times 10^{19}$ cm^{-3}): $\square$=3.4; $\triangle$=8.9; $\diamond$=18; $\circ$=24; $\triangledown$=35. $\times$ symbols in the ZT figure indicate the accuracy of the data is questionable as the ZT value is much higher than previously reported values for bulk p-type $Si_{1-x}Ge_x$.

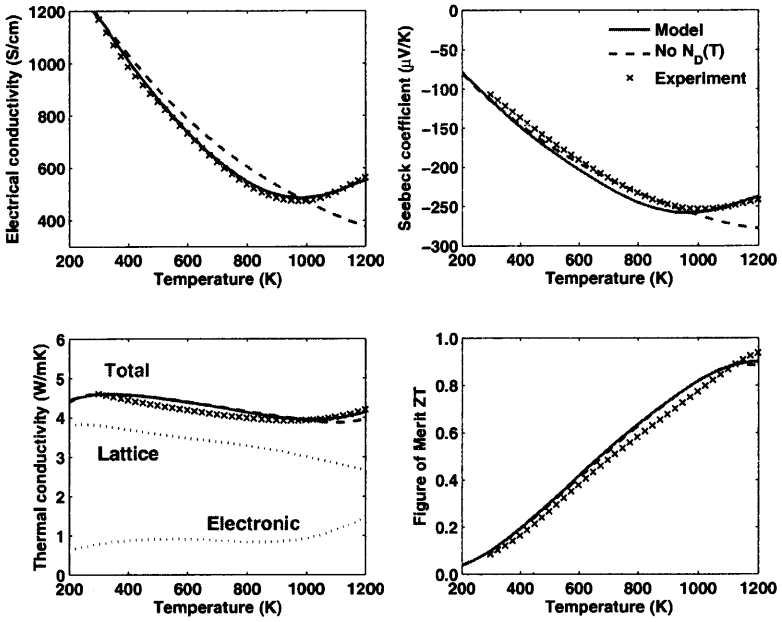

Figure 2-3: Experimental (symbols) and calculated (curves) thermoelectric properties of state-of-the-art n-type bulk $Si_{0.8}Ge_{0.2}$. (Solid line - model including carrier concentration variation with temperature; dashed line - model without carrier concentration variation with temperature; dotted lines - electronic and lattice components of thermal conductivity.)

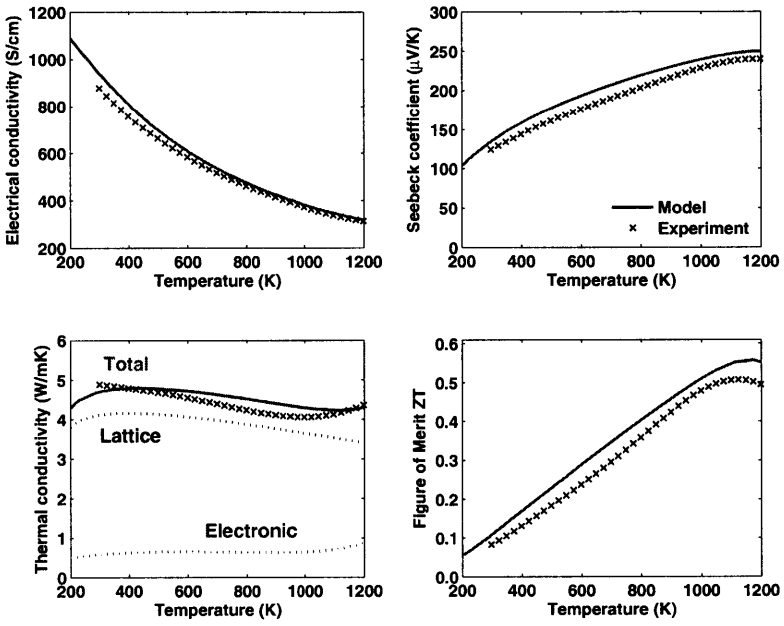

Figure 2-4: Experimental (symbols) and calculated (curve) thermoelectric properties of state-of-the-art p-type bulk $Si_{0.8}Ge_{0.2}$. (Solid line - model; Dotted lines - electronic and lattice components of thermal conductivity.)

with the experimental data over the temperature range. As expected, the n-type material exhibits a strong carrier concentration variation with temperature due to dopant precipitation effects. To account for this, the calculated mobility and the experimental electrical conductivity are used to estimate the carrier concentration variation with temperature using $\sigma = ne\mu$. As the mobility depends on the carrier concentration to some extent, an iterative procedure to ensure consistency between all the properties is employed. The carrier concentration variation is found to be similar to that deduced for the n-type nanocomposite, and using either one will give a good fit; the fit from the bulk experimental data is used for both Figs. 2-1 and 2-3 as this fit gives a smoother curve.

2.4 Modeling nanocomposites

$Si_{1-x}Ge_x$ nanocomposites can have markedly different transport properties from their bulk counterparts. Grain boundaries in materials can act as interfaces to scatter phonons,[6] electrical traps for charge carriers,[67–69] and segregation sites for dopant atoms.[51,69] In nanocomposites these effects are further enhanced because the grain size is often comparable to or smaller than characteristic lengths such as the phonon mean free path or the electron wavelength. TEM images also show that the microstructure of nanocomposites is much more complicated than that of microcrystalline materials; in nanocomposites the nanometer-sized grains contain defects and composition variations, and the nanometer-sized grains themselves are embedded inside larger grains.[15–17] We focus our discussion on the effects of grain boundaries between the nanometer-sized grains as these are expected to have the largest impact on transport properties.

The most obvious way the thermoelectric properties are affected by grain boundaries is by a reduction in lattice thermal conductivity, which is the mechanism of ZT enhancement in $Si_{1-x}Ge_x$ nanocomposites.[16,17] It is also found that the presence of grain boundaries reduces the electrical conductivity and can affect the Seebeck coefficient. The physical mechanisms for these changes in the transport properties

of polycrystalline materials have been the subject of much discussion, especially for polycrystalline silicon.[37,38] The reduction in lattice thermal conductivity is attributed to strong interface scattering of phonons.[6] For charge carriers, the generally accepted model to explain the effects of grain boundaries is the charge-trapping model.[67–69] This model postulates that incomplete bonding in grain boundaries leads to the formation of many surface states within the band gap, making it preferable for carriers to occupy these lower energy states. Due to a depletion of the grain near the grain boundary, a space charge region with a potential barrier forms; this potential acts as a scattering potential for charge carriers. Dopant segregation is also thought to affect the electrical properties of grain boundaries, though if and how the grain boundaries are affected is not well understood.[69] Misalignment of crystallographic directions between adjacent grains can also lead to electron scattering processes.[70]

To obtain quantitative predictions of how grain boundaries affect the thermoelectric properties in nanocomposites using the Boltzmann equation, it is necessary to develop phonon and charge carrier grain boundary scattering models which give a grain boundary scattering rate τ_{GB}^{-1}. The resulting scattering rates can then be added to the bulk scattering rate, as in Eq. 2.30 for charge carriers, and the thermoelectric properties calculated in a similar manner to the bulk case. We now develop the grain boundary scattering models. Here, we specialize the situation for charge carrier scattering to electrons in an n-type material; the same discussion will apply to holes in a p-type material.

2.4.1 Phonon scattering

There have been several previous efforts to determine the thermal conductivity of nanocomposites. Yang and co-workers calculated the effective thermal conductivity of a nanocomposite using the phonon Boltzmann equation.[43,44] Monte Carlo techniques have also been used to calculate the thermal conductivity, giving good results but requiring significant computational time.[71] Prasher has had considerable success obtaining analytical solutions to the Boltzmann equation for simple geometries.[72,73] Scattering models based on Rayleigh scattering[74] and acoustic Mie scattering theory[75]

have also been used to treat nanoparticle scattering. Minnich and Chen introduced a modified theory to analytically compute the thermal conductivity of nanocomposites.[76]

For the present work we use a standard boundary scattering rate.[12,74] We can derive the model by examining characteristic lengths relevant to phonon transport. In this case the appropriate lengths are the phonon mean free path relative to the grain size. Our calculations for bulk, poly-crystalline $Si_{0.8}Ge_{0.2}$ indicate that a large fraction of phonons have a mean free path (MFP) λ_{PH} of about 100 nm, which is much larger than the nanocomposite grain size l_g of about 10-20 nm. A reasonable model is thus one which approximates that the phonon MFP in nanocomposites is limited to the grain size such that $\lambda_{PH} = l_g$. Then, using the sound speed as the phonon velocity, as in the Debye model, the scattering rate follows immediately:

$$\tau_{GB}^{-1} = \frac{v_s}{l_g} \tag{2.35}$$

This is added to the other phonon scattering rates, and the lattice thermal conductivity is calculated in the same manner. We are able to obtain a good fit to the thermal conductivity data using a grain size l_g of ten to twenty nanometers, which is consistent with the experimental values recently reported.[16,17]

2.4.2 Electron scattering

The grain boundary model for electrons is based on the charge trapping model, which postulates that the formation of surface states at the grain boundary depletes the grain of carriers near the grain boundary, resulting in a space charge region with a potential barrier. The potential barrier acts as a scattering potential which affects electron transport. To calculate electrical properties, it is necessary to develop a model which can describe this phenomenon with a relaxation time, but to create a consistent model it is necessary to clarify details of the GB scattering process. Important questions that must be answered are what is a physical value for the GB potential, whether the electron wave experiences diffuse or coherent scattering, and

over what length scale the grain boundary potential affects the electrons.

The first question, regarding an appropriate value for the GB potential, can be answered using a depletion region approximation. This analysis yields the following equation for the GB potential, assuming all the trap states are filled:[67]

$$U_g = \frac{qN_t^2}{8\epsilon N_D} \tag{2.36}$$

where ϵ is the permittivity, N_D is the doping concentration, and N_t is the number density of traps. For $N_D \approx 1\times10^{20}$ cm^{-3} and $N_t \approx 1 \times 10^{13}$ cm^{-2}, U_g will be around 20 meV. Of course, the trap density is unknown and could vary widely. An important unresolved question is how dopant segregation affects the distribution and quantity of surface states.[69] It is known that P in $Si_{1-x}Ge_x$ has a strong tendency to precipitate in the GB,[51] and in principle the extra dopant atoms thus provided to the GB could affect the surface state distribution. Assuming that the reported values for $N_t \approx 1\times10^{11}$ cm^{-3}-1×10^{13} cm^{-3} are a reasonable estimate for our materials, at high doping levels this model predicts that U_g should be less than 20 meV.[69] However, we find that a larger GB potential is required to fit the nanocomposite data; we will discuss possible reasons for this discrepancy in Sec. 2.6.

The last two questions, whether the electron wave experiences diffuse or coherent scattering and over what length scale the grain boundary potential affects the electrons, can be answered by examining the key length scales related to carrier transport in nanocomposites as was done for phonons. TEM and XRD measurements indicate that the average GB size is ten to twenty nanometers and its thickness is around one nanometer.[16,17] We can determine how these length scales compare with carrier length scales by computing the screening length R, the electron wavelength λ_e, and the electron MFP.

The screening length R was previously given in Eq. 2.29. Computing this value shows that R is less than one nanometer, implying that the GB potential is completely screened unless the electron is within a few nanometers of the GB. Hence, we can conclude that the model should focus on only a small section of the GB, since long-

range potentials from other sections of the GB are neutralized by screening effects. The Mayadas model[53] is not consistent with this result as it models the potential as a series of grain boundaries.

Next, the type of scattering must be determined. For example, if there are substantial variations in the potential at the GB we might expect the electron wave to be scattered diffusely, but if the variations are small, the scattering should be coherent. In addition, if the MFP is comparable to the grain size, we might also expect multiple scattering effects to be important. These questions can be resolved by calculating the distribution of electron wavelengths and MFPs. We first determine the cumulative distribution function of the electron occupation number versus wavelength, which gives the percentage of electrons that have a wavelength less than a certain value. The electron wavelength λ_e is given by the de Broglie expression:

$$\lambda_e = \frac{2\pi\hbar}{m_c^* v} = \frac{2\pi\hbar(1+2\alpha E)}{\sqrt{2m_c^* E(1+\alpha E)}} \tag{2.37}$$

where m_c^* is the conductivity mass. We define the transport electron occupation number as:

$$g_t = v^2 \left(-\frac{\partial f_0}{\partial E}\right) D(E) \tag{2.38}$$

Integrating g_t to a certain value and normalizing the result by the integral over all energy will give the cumulative distribution function for the transport electron occupation number. Additionally, we can determine the electron MFP length using an equation of the form $l = v\tau$, where v is the electron velocity and τ is the total bulk electron relaxation time. The electron MFP will in general be energy-dependent, and we can relate the electron MFP to the wavelength λ_e by expressing each as a function of energy.

These two quantities, the transport electron wavelength cumulative distribution function and the electron MFP versus wavelength, are shown in Fig. 2-5 at 300 K for heavily doped bulk $Si_{0.8}Ge_{0.2}$. The first observation we can make is that most electrons have mean free paths between two and five nanometers, which is smaller than the grain size. This fact implies that each small section of the grain with which

the electron interacts is independent of the others: since the grain size is on average on the order of ten to twenty nanometers, after the electron scatters from the GB it will, on average, experience several collisions before it reaches another part of the GB. Thus the memory of the previous collision is essentially lost by the time the carrier reaches another part of the grain, and we can conclude that each scattering point on the GB is independent from the others. This is further evidence against using the Mayadas model for thermoelectrics as it accounts for the effects of many grain boundaries scattering coherently.

The second observation is that most electrons have a wavelength between six and eleven nanometers, which is much larger than the GB thickness of one nanometer. Diffuse scattering of the electron wave requires substantial potential variation so that the wave is scattered randomly in all directions. Since the barrier potential is confined to a region very close to the GB itself, any spatial variation in the potential can only occur over a length on the order of the GB thickness. Furthermore, having a large variation in the value of the potential along the GB would require substantial nonuniformities which have not been observed in microstructure studies. These two results suggest that any variation in potential is not large and is confined to a region much smaller than the electron wavelength, which implies that the large variation in potential required for diffuse electron scattering is not present. Thus we can conclude that electrons for the most part should scatter coherently from the GB, enabling the use of scattering theory to calculate scattering rates of an electron wave from a scattering potential.

The third observation we make is that the electron MFP is predicted to be smaller than the wavelength, implying that the Boltzmann equation is at the edge of its validity. As the Boltzmann equation still gives good results for both bulk and nanocomposite materials, the above discussion is still expected to hold. This issue is further discussed in Sec. 2.6.

Based on the above discussion, the physical picture for GB scattering is that of a carrier interacting with local regions of the GB, with each region acting as an independent scattering site which coherently scatters an electron wave. The GB is

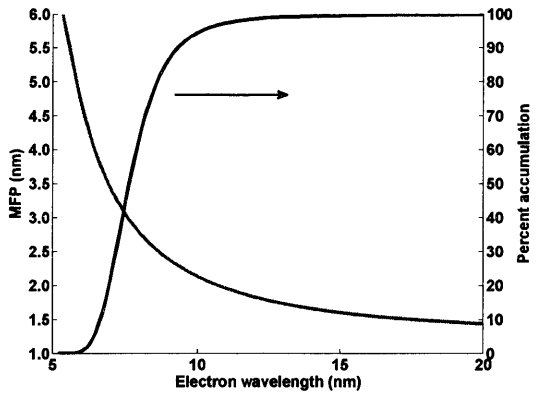

Figure 2-5: Computed results for the electron mean free path versus electron wavelength (left axis), and percent accumulation of electron occupation number versus electron wavelength (right axis) for n-type ($N_D \approx 2\times10^{20}$ cm^{-3}) bulk $Si_{0.8}Ge_{0.2}$ at 300 K.

composed of many of these scattering sites. The most appropriate model for GB scattering is therefore one which models only a local potential along a small section of the GB.

Using these results, we can now create an electron GB scattering model by identifying a scattering potential and calculating the corresponding scattering rate. We have developed a model which describes a small section of the grain boundary with a scattering potential U_g in a cylindrical region, as illustrated in Fig. 2-6. Since the actual GB is an extended line defect, the modeled GB is composed of many such cylinders, each of which acts as an independent scattering site. Possible variations in the value of the scattering potential throughout the thermoelectric material are not considered here. If r_0 is the radius of the cylinder, z is the direction normal to the GB, and $z = 0$ is at the center of the GB, then the model potential is given by:

$$U_g = \begin{cases} U_0 e^{-|z|/z_0} & r < r_0 \\ 0 & r > r_0 \end{cases} \tag{2.39}$$

Here U_0 is the maximum grain boundary potential, r_0 is a constant on the order of the screening length R, and z_0 is a constant related to the size of the depletion region. This particular form of the potential is chosen for several reasons. The

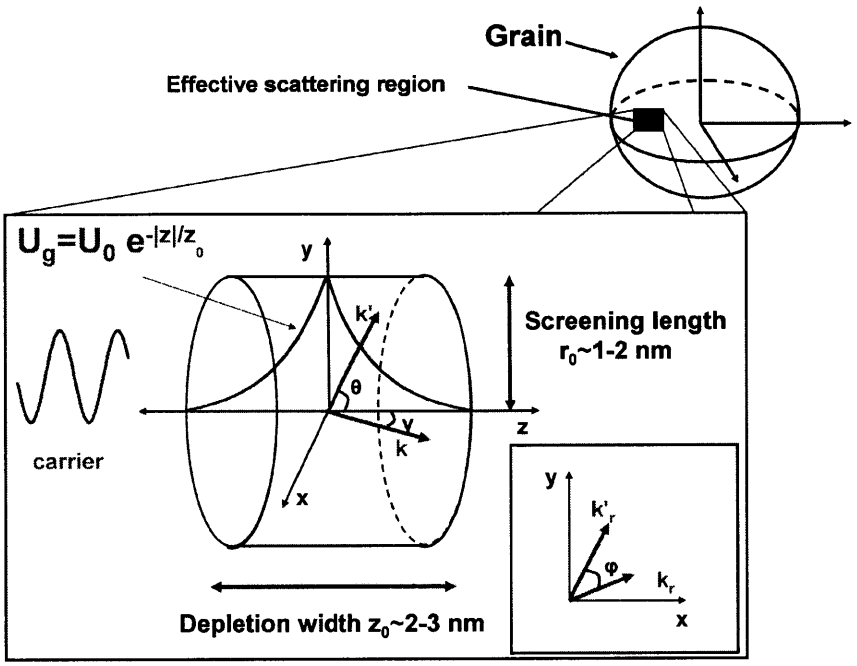

Figure 2-6: Schematic of the cylinder model for electrical grain boundary scattering.

decaying exponential form of the potential in z is used as an approximation to the exact potential which would result from a carrier depletion region. The cylindrical geometry is chosen to model the effects of screening: within the cylinder the GB potential acts on the electron, but beyond several multiples of the screening length the GB potential is screened out and is essentially zero.

With the scattering potential determined, the final step is to determine the scattering rate. We use the first Born approximation to calculate the scattering rate as the GB potential is not expected to be large. The matrix element $M_{kk'}$ for the potential is:

$$M_{kk'} = \int e^{i\vec{k}\cdot\vec{r}} U_g(\vec{r}) e^{-i\vec{k'}\cdot\vec{r}} d^3r = \int e^{i\vec{q}\cdot\vec{r}} U_g(\vec{r}) d^3r \tag{2.40}$$

$$= 4\pi U_0 \left(\frac{z_0}{1+(q_z z_0)^2}\right) r_0^2 \left(\frac{J_1(q_r r_0)}{q_r r_0}\right) \tag{2.41}$$

where $J_1(z)$ is a first order Bessel function of the first kind, $\vec{q} = \vec{k} - \vec{k'}$, and q_r and q_z are the r and z components of $\vec{q}$, respectively. Here the $r-z$ coordinate system is relative to that of the disk. From Fig. 2-6, we can express q_r and q_z in terms of γ,

the angle between the z-axis and $\vec{k}$; θ, the angle between the z-axis and $\vec{k'}$; and ϕ, the angle between k_r and k'_r. The result is:

$$q_z = k_z - k'_z = k(\cos\gamma - \cos\theta) \tag{2.42}$$

$$q_r = k\sqrt{\sin^2\gamma + \sin^2\theta - 2\sin\gamma\sin\theta\cos\phi} \tag{2.43}$$

The scattering rate and momentum relaxation times can be obtained from the expressions:

$$S(k,k') = \frac{2\pi}{\hbar}|M_{kk'}|^2\delta(E_{k'} - E_k) \tag{2.44}$$

$$\tau^{-1} = \frac{2}{(2\pi)^3}\int_0^{2\pi}\int_0^{\pi}\int_0^{\infty} S(k,k')(1-\cos\theta)k'^2\sin\theta dk' d\theta d\phi \tag{2.45}$$

Since the potential does not have spherical symmetry, evaluating the momentum relaxation time is more complicated and an analytic solution is not possible. Using the definitions above, the momentum relaxation time can be shown to be:

$$\tau_{GB}^{-1} = \frac{8\pi^2 U_0^2 z_0^2 r_0^4 D(E)}{\hbar} N_g I(r_0, z_0) \tag{2.46}$$

$$I(r_0,z_0) = \frac{1}{\pi}\int_0^{2\pi}\int_0^{\pi}\int_0^{\pi}\left[\frac{\sin\theta(1-\cos\gamma\cos\theta-\sin\gamma\sin\theta\cos\phi))}{(1+(q_z z_0)^2)^2} \times \frac{J_1^2(q_r r_0)}{(q_r r_0)^2}\right] d\gamma d\theta d\phi \tag{2.47}$$

where N_g is the number of cylinders per unit volume. An average has been performed over the incoming angles γ.

This scattering rate has two distinct regimes. For $\xi \ll 1$ (low energy electrons), $\tau_{GB}^{-1} \propto E^{1/2}$, similar to the energy dependence of a diffusive boundary scattering rate. For $\xi \gg 1$ (high energy electrons), $\tau_{GB}^{-1} \propto E^{-3/2}$, similar to the energy dependence of the ionized impurity scattering rate. Depending on the value of the cylinder radius r_0, this change in energy dependence could give an energy filtering effect.

The final quantity needed is the density of cylinders N_g. If the grain boundary is modeled as a sphere, the number of cylinders per grain is simply the surface area of

the sphere divided by the base area of the cylinder. The number density of cylinders is then just the number of cylinders per grain multiplied by the number density of grains:

$$N_g = \frac{1}{2}\frac{4\pi(l_{gb}/2)^2}{(\pi r_0^2)} \times \frac{1}{(l_{gb}/2)^3} \times f = \frac{4f}{l_{gb}r_0^2} \tag{2.48}$$

The factor of 1/2 is necessary as each cylinder is shared between two grains. The parameter $0 < f < 1$ is a constant which accounts for the geometrical distribution of the cylinders. In the actual material, the cylinders are arranged according to the shape of the grain boundaries, but in the derivation above it is implicitly assumed that the cylinders are uniformly distributed throughout the material. This could lead to an overestimation of the scattering rate. To estimate the magnitude of this effect, we implemented a simple Monte Carlo simulation which models a particle traveling through a three-dimensional lattice containing GB scattering sites in various geometries. In the first case, the GB sites are arranged along the faces of a cube, an approximation to their actual locations in the material; in the second case, the same number of GB sites are distributed uniformly throughout the region. After the particle passes through the GB site it is assumed the particle experiences an elastic, velocity-randomizing collision; the particle also experiences the same type of collision over a randomly chosen distance between two and five nanometers to account for other scattering processes. For each geometry, the number of times the particle passes through a GB site is recorded. This analysis indicates that assuming the same number of GB sites are uniformly distributed overestimates the number of times the particle is scattered by a GB site by approximately 30%. To compensate for this, we simply set $f \approx 0.7$-0.8 to reduce the effective density of cylinders. This is valid as it was previously shown that all the GB scattering sites should be independent of each other. The results are not particularly sensitive to the value of f: using a value of $f \pm 0.1$ will give a GB potential of approximately $U_g \pm 5\ meV$. We use $f = 0.7$ for the calculations in this study.

With the scattering rate determined, the thermoelectric properties of nanocomposites can be determined by adding the GB scattering rate to the other scattering

rates using Matthiessen's rule. To explain the nanocomposite data, suitable values of the model parameters will need to be determined. The adjustable parameters of the model are the barrier height U_g, the radius of the disk r_0, and the potential decay constant z_0. However, the parameters are not totally arbitrary: to be consistent with the characteristic lengths discussed before, r_0 must be on the order of the screening length, about one to two nanometers, and z_0 must be on the order of the space charge region width, about two to four nanometers. The charge trapping model predicts that U_g should be less than 20 meV, though the required GB potential turns out to be larger. In addition, for the lattice thermal conductivity model the grain size must be specified; this is determined from XRD measurements to be on the order of ten to twenty nanometers.[16,17]

2.5 Nanocomposite results

Using these values as a guide, we have calculated the thermoelectric properties for n-type and p-type $Si_{0.8}Ge_{0.2}$ nanocomposites whose properties were recently reported.[16,17] The fitting procedure is as follows. First, with all other parameters kept constant, the parameters r_0, z_0, and U_g are adjusted so that the calculated mobility agrees with the experimental results. Next, the carrier concentration versus temperature variation is determined using the calculated mobility and the reported electrical conductivity. As mentioned before, we cannot simply use the electrical conductivity from the mobility measurement because each experimental system subjects the sample to different heat treatments. Finally, the electrical conductivity, Seebeck coefficient, thermal conductivity, and ZT are calculated. If the calculation is consistent, after fitting the mobility and carrier concentration the calculated results for all the properties should match the experimental data.

2.5.1 N-type nanocomposite $Si_{0.8}Ge_{0.2}$

We are able to obtain excellent agreement with the experimental data for the n-type nanocomposite using this procedure, indicating that the Boltzmann equation and

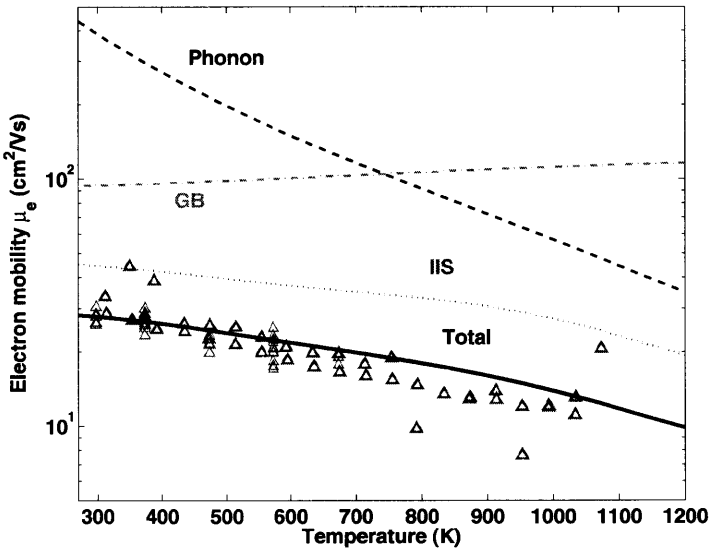

Figure 2-7: Calculated mobility for each scattering mechanism and total mobility (curves) with experimental data (symbols) for the n-type $Si_{0.8}Ge_{0.2}$nanocomposite. (Solid line - total mobility; broken lines - mobility for each scattering mechanism.)

the GB scattering model are a good description of the transport. The calculated and experimental mobilities are shown in Fig. 2-7. Ionized impurity scattering is the dominant scattering mechanism over most of the temperature range, with GB scattering next most dominant at room temperature and acoustic phonon scattering next most dominant above 1000 K. The GB scattering fitting parameters used to obtain this result are summarized in Table 2.1.

Figure 2-8 shows the n-type and p-type carrier concentrations versus temperature. For the n-type nanocomposite, there is a slight decrease in electron concentration with temperature at intermediate temperature, followed by a large increase in electron concentration with temperature at elevated temperature. This behavior is consistent with previous reports, as dopant precipitation to the GB in n-type $Si_{1-x}Ge_x$ is known to be a significant process even at intermediate temperatures of 600-900 K.[51,58] At room temperature the material is a supersaturated solution of $Si_{0.8}Ge_{0.2}$ and P as the material has been quenched in air to room temperature, freezing the dopants in place. As the temperature is increased P is rejected from the lattice as the material attempts

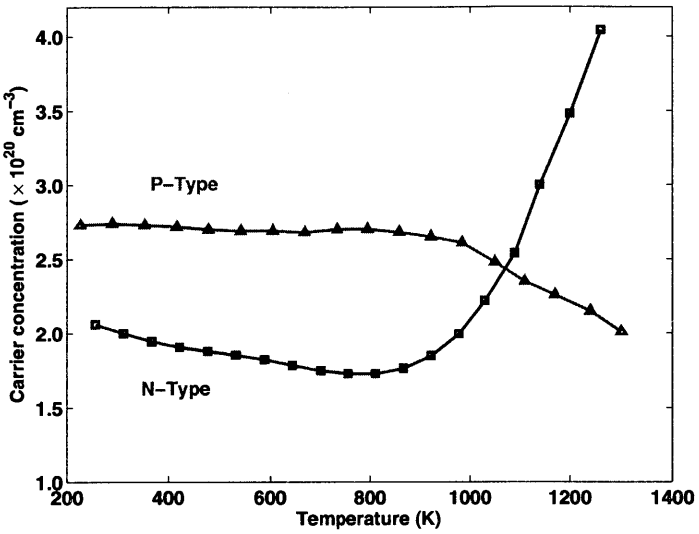

Figure 2-8: Extracted carrier concentration versus temperature for the n-type and p-type $Si_{0.8}Ge_{0.2}$ nanocomposites.

to return to its equilibrium state. At high temperature, the dopants are reactivated due to the increasing solubility limit and the electron concentration increases. Somewhat unexpectedly, the presence of additional grain boundaries in the nanocomposite does not seem to exacerbate this phenomenon; the bulk and nanocomposite materials exhibit very similar carrier concentration versus temperature curves.

The calculated thermoelectric properties, including dopant precipitation effects, are shown in Fig. 2-9 (solid curves), along with the nanocomposite experimental data (symbols) and the calculated results without GB scattering for comparison (dashed lines). The calculated results which include GB scattering are in excellent agreement with the experimental results. Dopant precipitation is seen to cause the normally monotonically decreasing electrical conductivity to actually increase above 1000 K; the opposite trend is present in the Seebeck coefficient. The same carrier concentration variation with temperature as was used for the bulk n-type case is also used here.

Table 2.1: Fitting parameters for the grain boundary potential used in $Si_{0.8}Ge_{0.2}$ nanocomposite modeling.

Material	$U_g[meV]$	r_0 [nm]	z_0 [nm]	l_g [nm]
n-type $Si_{0.8}Ge_{0.2}$	45	1.0	2.0	12
p-type $Si_{0.8}Ge_{0.2}$	45	1.0	2.0	20

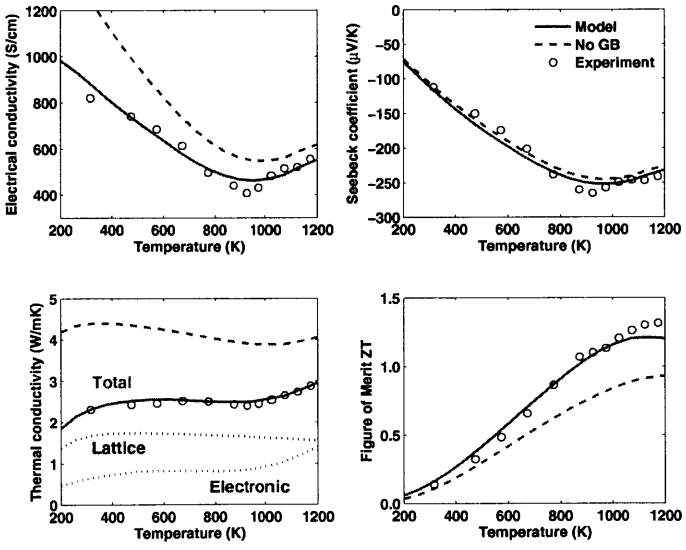

Figure 2-9: Calculated (curves) and experimental (symbols) thermoelectric properties for the n-type nanocomposite (data from Ref. [16]). (Solid lines - model including GB scattering; dashed lines - model without GB scattering; dotted lines - electronic and lattice components of thermal conductivity.)

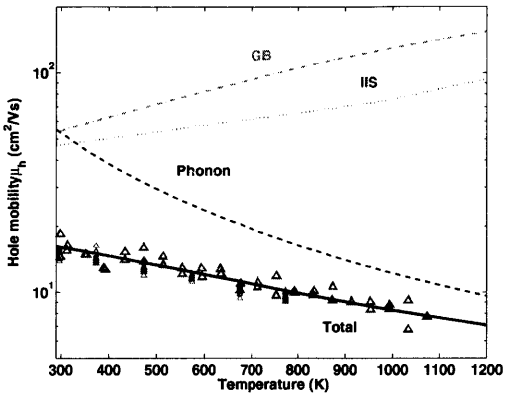

Figure 2-10: Calculated mobility for each scattering mechanism and total mobility (curves) with experimental data (symbols) for the p-type nanocomposite. (Solid line - total mobility; broken lines - mobility for each scattering mechanism.)

2.5.2 P-type nanocomposite $Si_{0.8}Ge_{0.2}$

Unfortunately, a completely consistent fit for the p-type nanocomposite could not be found. Specifically, the model is not able to predict the high Seebeck coefficient that is observed experimentally without making an adjustment to the hole effective mass. We find that increasing the hole effective mass from $1.2m_e$ to $1.55m_e$ is able to explain the data, possibly indicating the nanocomposite valence band is different from that of the bulk. A change in hole effective mass has been reported in strained $Si_{1-x}Ge_x/Si_{1-y}Ge_y$ thin films,[77] but whether the same phenomenon is responsible for the observed nanocomposite properties is not clear.

The mobility is shown in Fig. 2-10. Unlike the n-type case, where ionized impurity scattering is dominant, here acoustic phonon scattering is the dominant scattering mechanism over most of the temperature range.

Figure 2-8 shows the hole concentration versus temperature. Unlike previous reports for bulk p-type $Si_{0.8}Ge_{0.2}$,[56] the nanocomposite does exhibit a change in hole concentration at elevated temperature, reducing from around 2.6×10^{20} cm^{-3} at room temperature to 2.0×10^{20} cm^{-3} at 1300 K. This is somewhat unexpected as carrier concentration changes in p-type $Si_{0.8}Ge_{0.2}$ had previously been observed only on the time scale of thousands of hours.[56] The explanation for this effect is similar to that

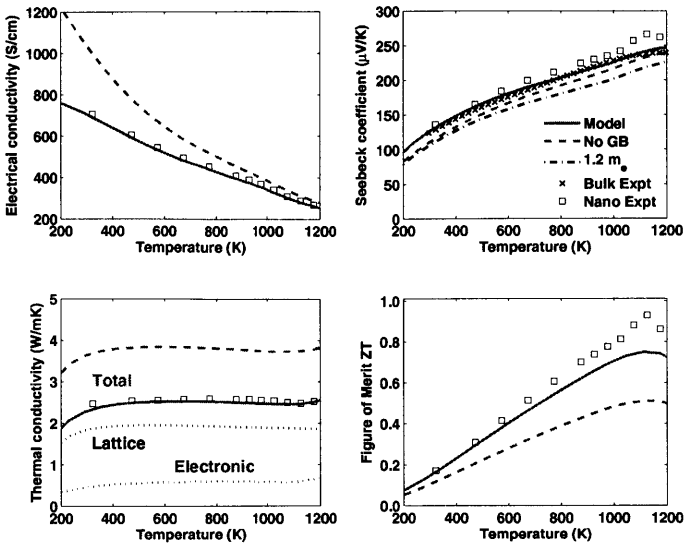

Figure 2-11: Calculated (curves) and experimental (symbols) thermoelectric properties for the p-type nanocomposite (data from Ref. [17]), along with the bulk experimental data shown earlier for reference. (Solid lines - model including GB scattering; dashed lines - model without GB scattering; dotted lines - electronic and lattice components of thermal conductivity; dash-dotted line - Seebeck coefficient calculated using the bulk effective mass of $1.2m_e$.)

for n-type dopant precipitation. At room temperature, the material is supersaturated with B, but it must be raised to a higher temperature of about 1000 K to reject B from the lattice. The B rejection causes the hole concentration to be reduced to a value closer to the solubility limit.

Figure 2-11 shows calculated thermoelectric properties for different conditions, along with the experimental thermoelectric properties of the nanocomposite and bulk material. One set of curves is calculated using an effective mass of $1.55m_e$ and includes GB scattering, while the second set does not include GB scattering but is otherwise the same. The Seebeck coefficient using the bulk effective mass of $1.2m_e$ has also been computed for comparison.

The calculated Seebeck coefficient obtained using the bulk effective mass of $1.2m_e$ is about 25% lower than the experimental data over the entire temperature range, while that calculated using $1.55m_e$ gives a better fit. An interesting feature of the

experimental data is that even though the hole concentration of the nanocomposite material is almost twice that of the bulk material (2.6×10^{20} cm^{-3} versus 1.4×10^{20} cm^{-3}), the Seebeck coefficient of the nanocomposite is actually equal to or higher than that of the bulk. We have tried many different types of GB scattering models, but none predict the level of increase in Seebeck coefficient that is observed; only by increasing the effective mass are we able to obtain a satisfactory fit for all the properties. However, whether the material actually does have a different effective mass from the bulk is not clear, and more investigation into the transport properties and band structure of nanocomposite p-type $Si_{0.8}Ge_{0.2}$ is necessary.

2.6 Discussion

We used the model calculations to better understand the effects of GB scattering on the thermoelectric properties. To start, we examine the nanocomposite and bulk experimental data more closely. For both the n-type and p-type materials, the nanocomposite electrical conductivity is reduced from the calculated value without GB scattering at room temperature, but the difference decreases as the temperature increases. This is expected because the acoustic phonon scattering rate goes as $T^{3/2}$ and thus becomes large compared to the other scattering mechanisms at high temperature, making the influence of GB scattering less significant as the temperature increases. Crucially, the phonon GB scattering rate is always much larger than the other phonon scattering rates over the entire temperature range. Thus, while the nanocomposite electrical conductivity approaches that of the bulk at high temperature, the lattice thermal conductivity is still much lower than that of the bulk, leading to a net increase in ZT which is most pronounced at high temperature. Unfortunately, this also implies that improving the electrical properties at high temperature is difficult because the mobility is always limited by acoustic phonon scattering, especially in the p-type material.

The model can provide additional information about GB scattering. An interesting observation is that the GB potentials required to fit the data are several

times higher than those predicted from the Poisson equation. Even with a very high trap density of $N_t = 1\times10^{13}$ cm^{-3} and a relatively lower doping concentration $N_D = 1\times10^{20}$ cm^{-3}, the magnitude of the GB potential is only predicted to be about 20 meV. However, the value required to fit the data is 45 meV. There could be several reasons for this. One likely possibility is that there are many more defects present than were accounted for in the model. TEM images show there are a variety of nanoprecipitates and composition variations that could also act as electron scattering sites.[15–17] In the model only scattering sites from the nanoscale grain boundaries are taken into account, but if the density of scattering sites is actually larger than this, the magnitude of the GB potential required to fit the data would decrease.

Another possibility is that nanocomposites have more disordered GB regions and thus more trapping states than have been previously measured for microcrystalline materials. The nanocomposite materials studied here are doped far beyond the solubility limit for the host material $Si_{0.8}Ge_{0.2}$, with the result that a large fraction of the inserted dopants are rejected from lattice sites and are forced into other regions of the material such as the GB. As an example, the p-type nanocomposite sample is doped with 5% B, or 2.5×10^{21} cm^{-3}, but the measured carrier concentration is only 2.6×10^{20} cm^{-3}, indicating that most of the dopants do not occupy substitutional sites in the lattice. It has been previously hypothesized that dopants might affect the number of trapping states in the GB, though if and to what extent the trapping states are modified is not known.[69] Unfortunately, it is not easy to determine the number of trapping states with common methods, such as capacitance measurements, due to the very small size of the grains.

Yet another possibility is that the grains are becoming so small that the volume fraction of GB is not negligible, making the material essentially composed of two phases, one being the host material and the inclusion phase being the GB material. Since the GB is expected to have very low carrier mobility, the combined material's mobility will be lower than would be predicted from a scattering model alone.

While it is clear that many questions remain concerning transport in nanocomposites, the results discussed here do suggest several strategies and research topics which

could lead to further improvements in ZT. One obvious topic for further research is determining how to fabricate nanocomposites with fewer defects and cleaner grain boundaries. If the number of defects or number of trapping states could be reduced, the GB scattering rate would be reduced and the mobility would increase, especially in the room temperature to intermediate temperature range. Understanding the reason for the mobility reduction and adjusting fabrication conditions to minimize it would thus be very helpful.

Another possible research topic is based on the observation that the lattice thermal conductivity has been reduced so far that it is nearing the electronic thermal conductivity; in the n-type case the electronic thermal conductivity is actually larger than the lattice component at high temperature. Unfortunately, this means that further reducing the lattice thermal conductivity will yield only marginal improvements in ZT as the lattice thermal conductivity approaches the electronic thermal conductivity. Research on ways to reduce the electronic and bipolar thermal conductivities would thus also be very useful.[23]

The final topic we discuss is the validity of the Boltzmann equation for highly doped thermoelectric materials. The Boltzmann equation is an equation for particle transport and neglects wave effects. For this requirement to be satisfied, it can be shown that the necessary condition is that the electron MFP be much longer than the electron wavelength.[48] However, as shown in Fig. 2-5, for highly doped $Si_{0.8}Ge_{0.2}$ the electron MFP is predicted to be even shorter than its wavelength, making the applicability of the Boltzmann equation somewhat questionable. The prediction of the wavelength being longer than the mean free path may also be caused by the inaccuracy of scattering models, which are mostly derived assuming that the doping level is not too high. Thermoelectric materials are very highly doped and are usually degenerate, however, and their electrical properties are sometimes closer to those of metals than to semiconductors. Thus while the Boltzmann equation has been successful in explaining most of the experimental data, a predictive capability for the transport properties of nanocomposites will require a more powerful formalism.

2.7 Conclusion

In this chapter, we have used the BTE under the relaxation time approximation to investigate the thermoelectric properties of nanocomposite $Si_{1-x}Ge_x$ alloys. We account for the strong GB scattering mechanism in nanocomposites using phonon and electron GB scattering models. We find that the calculations are in excellent agreement with the reported properties for the n-type nanocomposite, but the experimental Seebeck coefficient for the p-type nanocomposite is larger than the model's prediction. Increasing the hole effective mass gives a better fit, possibly indicating the valence band in the nanocomposite is different from that of the bulk material. We also find that dopant precipitation is an important process in both n-type and p-type nanocomposites, in contrast to bulk SiGe, where dopant precipitation is most significant only in n-type materials. Finally, the model shows that the grain boundary potential required to fit the data is several times larger than the value obtained using the Poisson equation. This suggests that an improvement in electrical properties is possible by reducing the number of defects in the grain or reducing the number of electrical trapping states at the grain boundaries.

To conclude this chapter, using modeling along with experimental characterization of our nanostructured materials has given us very useful insight into the nanoscale transport processes taking place in these materials. These kinds of relatively simple computations allow us to gain a much deeper understanding of nanoscale transport than if we only examine experimental data.

Chapter 3

Determining phonon mean free paths: the quasi-ballistic heat transfer regime

3.1 Background

In chapter 2 we saw that modeling, combined with experimental characterization, can give us useful insight into nanoscale transport processes. However, one problem with this approach is that it is indirect: while the model may be able to fit the data, there is really no guarantee the model is correct. Even completely unphysical models can fit the data presented in chapter 2 if the numbers are tweaked appropriately.

Because of this dilemma, it is natural to wonder if there is a way we can more directly study the heat carriers themselves, rather than relying on indirect models. Unfortunately, if we restrict ourselves to only measuring macroscopic transport properties, like was done in chapter 2, we quickly run into a problem.

Let us examine the kinetic equation for the phonon thermal conductivity. We can express the thermal conductivity as:

$$k = \frac{1}{3}\int_0^{\omega_m} C_\omega v_\omega \Lambda_\omega d\omega \tag{3.1}$$

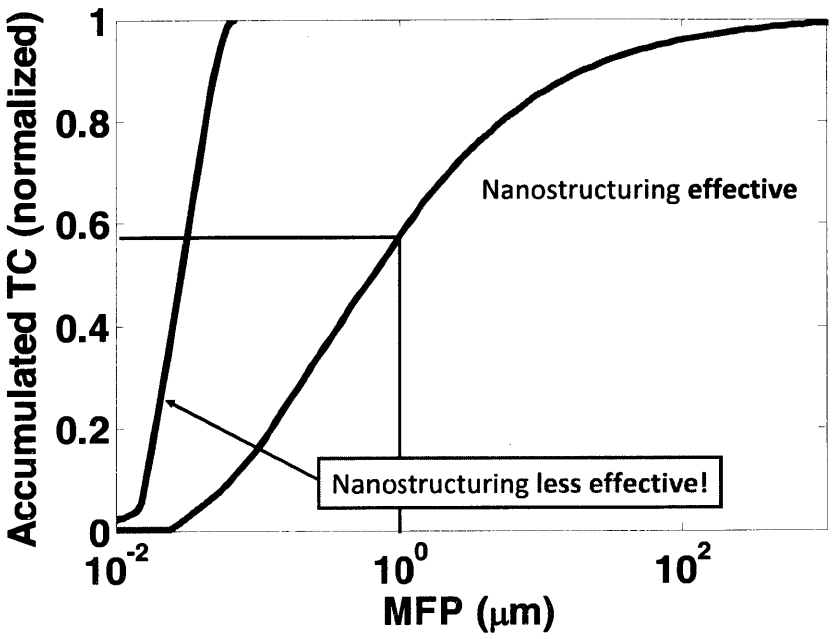

Figure 3-1: Thermal conductivity (TC) accumulation (cumulative distribution function) versus MFP. Even though these two distributions could have the same thermal conductivity, the MFPs of phonons carrying the heat are completely different. Knowledge of this distribution is critical for nanoscale engineering.

where C_ω is the specific heat, v_ω is the group velocity, Λ_ω the mean free path (MFP), ω_m is the cutoff frequency, and ω the phonon frequency. From this integral, we see that if we only measure macroscopic transport properties like the thermal conductivity, we measure the integral effect of all phonons contributing to the heat transfer. The information about the underlying distribution is not easily accessible. In fact, any distribution of MFPs Λ_ω can give the thermal conductivity we measure, if the numbers are adjusted appropriately. Therefore, simply measuring macroscopic properties cannot reveal properties of the distribution. To directly measure properties of the carrier distributions, like MFPs Λ_ω or relaxation times $\tau_\omega = \Lambda_\omega / v_\omega$, we need a new strategy.

Before discussing what the strategy is, it is necessary to emphasize why this information is so important. The reason is illustrated in Fig. 3-1, which shows the thermal conductivity accumulation, or cumulative distribution function (CDF) of the

thermal conductivity, as a function of the MFP. This shows how much different MFPs contribute to the total thermal conductivity. In principle, both of these distributions could have the same thermal conductivity after the distribution is integrated. However, the two distributions are completely different: it is difficult to engineer the thermal properties of materials with the blue distribution because the MFPs are already very short. Meanwhile, the opposite is true for the green distribution: it is much easier to engineer the thermal properties in this material because there are many long MFP phonons which can be modified by nanostructuring. Unfortunately, this dichotomy cannot be revealed by macroscale transport measurements.

Clearly, our lack of knowledge concerning MFPs is of concern, because it is very difficult to engineer a material at the scales of the MFPs unless we know their values. While nanostructured materials such as nanowires, superlattices, and nanocomposites with strongly reduced thermal conductivities have recently been reported and are being assessed for use in thermoelectric applications,[13,14,35,36] further engineering these materials will require a better understanding of phonon MFPs.

3.2 The quasi-ballistic heat transfer regime

In order to directly measure properties like MFPs, we need to study transport at the fundamental scales of the phonons themselves. Consider a typical macroscale thermal measurement. If thermal transport is studied in the diffusive regime, or for length and time scales much longer than MFPs and relaxation times, the phonons have already relaxed to a near-equilibrium distribution. Because of this, the relaxation information is not easily accessible.

In the quasi-ballistic regime, however, where length and time scales are shorter than MFPs and relaxation times, the phonons have not had a chance to relax due to a lack of scattering events. As a result, local thermal equilibrium does not exist and the transport is non-diffusive. By observing transport at these scales and watching the phonons relax, we can extract information about MFPs or relaxation times.

This type of size effect, where there is a large temperature gradient over the scale

of phonon MFPs, has been studied both theoretically and experimentally. Transient ballistic transport has been studied using heat-pulse techniques at cryogenic temperatures in low defect materials such as single-crystal sapphire, where phonon MFPs are comparable to the dimensions of the sample itself.[78] A nonlocal theory of heat transport was proposed as a modification of diffusion theory in the case where some phonon modes are ballistic.[9] Chen predicted that the heat conduction from a heat source smaller than the phonon MFP of the surrounding medium is significantly reduced.[8] Such non-diffusive transport has important implications for heat transfer in microelectronic devices.[79]

As an introduction to this transport regime, in this chapter we numerically solve the frequency-dependent Boltzmann transport equation (BTE), which is valid at length and time scales shorter than MFPs and relaxation times, to better understand how the quasi-ballistic transport regime can yield information about the phonon distribution. We solve the BTE for a metal film on a substrate using the method of discrete ordinates. The metal film on a substrate geometry is the same as that used in transient thermoreflectance (TTR) experiments.[80] In subsequent chapters we will experimentally demonstrate a technique which uses observations of quasi-ballistic transport to extract information about phonon MFPs.

There have been many numerical solutions to the phonon Boltzmann transport equation (BTE) in past years,[7,81–85] but many studies used frequency averaged properties. In a material such as Si, where phonon MFPs can vary by five orders of magnitude over the Brillouin zone,[86] this assumption is clearly not realistic. While some studies did include frequency dependence,[81–83,85] several of these studies made other simplifying assumptions which are not self-consistent.[81,82] A calculation of the phonon transport through a single material, including dispersion and polarization, has been reported, but the calculation did not include interfacial transport.[83]

Here we include the frequency-dependence of the phonon properties in both the metal film and the substrate, allowing for a frequency-dependent interface condition. We discuss the definition of thermal boundary resistance at the metal-substrate interface including frequency dependence. We use the model to show that Fourier's

law does not correctly describe the transport in the quasi-ballistic case, and to examine how observing quasi-ballistic transport can reveal information about the phonon relaxation times.

3.3 Numerical solution of the frequency-dependent phonon Boltzmann transport equation

Here we describe our numerical solution of the transient, one-dimensional, frequency-dependent phonon BTE. To simplify the analysis, heat conduction due to electrons in the metal film is neglected; only phonon heat conduction is considered. In reality, of course, electrons conduct a majority of the heat in metals. However, it has been shown that a thermal resistance due to electron-phonon coupling exists which modifies the effective interface conductance value.[87] As we are interested in observing changes in thermal properties due to quasi-ballistic transport only, to simplify the interpretation we do not include electron heat conduction in the calculation. The thermal conductivity of the metal film is taken to be only that of the lattice, approximately 20 W/mK.

The BTE is given by:[81]

$$\frac{\partial f_\omega}{\partial t} + \mu v_\omega \frac{\partial f_\omega}{\partial x} = -\frac{f_\omega - f_\omega^0}{\tau_\omega} \tag{3.2}$$

Here $f_\omega = \hbar\omega D(\omega) g(\omega)/4\pi$ is the desired distribution function, where $\hbar$ is Planck's constant divided by 2π, ω is the angular frequency, $D(\omega)$ is the phonon density of states, and $g(\omega)$ is the occupation function; f_ω^0 is the equilibrium distribution function, $\mu = \cos\theta$ is the cosine of the angle between the propagation direction and the x-axis, and τ_ω is the frequency dependent relaxation time. The factors of 4π normalize the distribution by the solid angle. Other treatments of the BTE[81,82] have written the equation in terms of the intensity $I_\omega = f_\omega v_\omega$; however, as will be shown later, optical phonons must be included in the calculation but have essentially zero group velocity. To allow for the case of zero group velocity, we remove the velocity from the definition.

The total thermal conductivity of metals is often in the hundreds of W/mK range, but as discussed earlier, much of this is due to electrons. Here we only consider the conduction due to the lattice. The lattice thermal conductivity of the metal is not known with certainty; we use a value of $k_l \approx 20$ W/mK. Phonon relaxation times are also not well known in metals, and we take the relaxation time τ to be a constant so that $k = 1/3 \int C_\omega v_\omega^2 \tau d\omega$ gives the specified thermal conductivity.

The equilibrium distribution f_ω^0 is given by

$$f_\omega^0(T) = \frac{\hbar\omega D(\omega) f_{BE}(T)}{4\pi} \tag{3.3}$$

where $f_{BE}(T) = (\exp(\hbar\omega/k_B T) - 1)^{-1}$ is the Bose-Einstein distribution function, and T is the temperature of the distribution.

For this study, we will take the materials to be an Al film on a Si substrate because these materials are commonly studied using TTR. This equation can be solved numerically for each frequency in both the film and the substrate, an appropriate interface condition applied, and the solution obtained. We now discuss several issues which must be treated properly to obtain a self-consistent solution.

3.3.1 Calculation of the equilibrium distribution

The equilibrium distribution f_ω^0 can be determined by integrating equation 3.2 with respect to frequency and angle and invoking conservation of energy.[81] The result is:

$$\int_0^{\omega_m} \int_{-1}^{1} \frac{f_\omega}{\tau_\omega} d\mu d\omega = \int_0^{\omega_m} \int_{-1}^{1} \frac{f_\omega^0}{\tau_\omega} d\mu d\omega \tag{3.4}$$

We now have a choice about how to satisfy this equation. In the past, the equation has been satisfied by enforcing equality at each frequency, or $f_\omega^0 = 1/2 \int_{-1}^{1} f_\omega d\mu$.[81,82] However, it has been shown that this approximation will not give the correct solution to the BTE.[85]

Therefore, it is necessary to determine the temperature T by integrating Eq. 3.4 over frequency and angle. To simplify the calculation, we approximate that the

temperature difference throughout the domain is not too large. We can then linearize the equilibrium distribution:

$$f_\omega^0(T) = \frac{\hbar\omega D(\omega) f_{BE}(T)}{4\pi} \approx f_\omega^0(T_0) + \frac{C_\omega}{4\pi}\Delta T \tag{3.5}$$

where $\Delta T = T - T_0$. This gives a simpler equation for the temperature of the equilibrium distribution:

$$\Delta T = \frac{4\pi}{\int_0^{\omega_m}(C_\omega/\tau_\omega)d\omega}\int_0^{\omega_m}\int_{-1}^{1}\frac{f_\omega - f_\omega^0(T_0)}{\tau_\omega}d\mu d\omega \tag{3.6}$$

The equilibrium distribution then follows immediately from equation 3.5.

Unfortunately, solving for the equilibrium distribution in this manner significantly complicates the solution. Since all the frequencies are coupled, Eq. 3.6 must be solved at each spatial point. In silicon, phonon MFPs can vary from a few nanometers for zone-edge phonons to millimeters for long wavelength phonons, a six order of magnitude difference. To obtain a correct solution for short mean free path phonons, the numerical spatial grid must have a small step size. However, to obtain a correct solution for the fast, long MFP phonons requires a large spatial domain. Since the solution must be known at every spatial point, these contradictory requirements imply a large domain with very fine spatial step size is required, making the solution computationally demanding. Multi-grid schemes, with a different spatial grid for each frequency, could be used, but to simplify numerical considerations we solve the distribution function for all frequencies on a single grid.

3.3.2 Role of optical phonons

Optical phonons are typically neglected in studies of phonon transport, as they contribute little to the thermal conductivity due to their near zero group velocity.[86] However, in transient heat transport, optical phonon modes with large specific heats act as a thermal capacitance and thus affect the transport, even if the modes do not actually transport any heat themselves.[83,88] We incorporate these phonons in Si (Al

does not have optical phonons) simply as another mode with zero group velocity. We must also specify an optical phonon relaxation time; we use a value of 3 ps.[89] The solution is not sensitive to the precise value. The optical phonon specific heat is given by the Einstein model assuming three degenerate optical branches:[47]

$$C_{op} = 3Nk_B \left(\frac{\hbar\omega_{op}}{k_B T}\right)^2 \frac{\exp(\hbar\omega_{op}/k_B T)}{(\exp(\hbar\omega_{op}/k_B T) - 1)^2} \tag{3.7}$$

where N is the number density of the material and ω_{op} is the optical phonon frequency, equal to 63 meV in Si.[60]

3.3.3 Interface condition

After the phonons travel through the metal film they reach the interface between the metal and substrate, where phonons are either transmitted or reflected. Unfortunately, the details of these transmission or reflection processes are largely unknown. A phonon could be scattered diffusely, or randomly in all angles; or specularly, in a mirror type reflection. Phonons could also scatter inelastically, resulting in a change in phonon frequency, or undergo mode conversion, resulting in a change in polarization.

In our treatment of the interface, we assume elastic, diffuse scattering and neglect any type of mode conversion: phonons do not change frequency or polarization as they cross the interface, but are scattered equally in all directions. A diagram with the dispersions of Al and Si, along with the allowed scattering modes, is shown in Fig. 3-2.

We can split the distribution function into forward-going ($0 < \mu < 1$) and backward-going ($-1 < \mu < 0$) phonons at both sides of the interface. Generally the incoming fluxes to the interface, or the forward going flux on side 1, $f^+_{\omega 1}$, and backward going flux on side 2, $f^-_{\omega 2}$, are known; the outgoing fluxes, or backward going flux on side 1, $f^-_{\omega 1}$, and the forward going flux on side 2, $f^+_{\omega 2}$, need to be determined.

The interface condition simply expresses that the heat flux carried by $f^-_{\omega 1}$ and $f^+_{\omega 2}$ is equal to the reflected and transmitted heat flux from $f^+_{\omega 1}$ and $f^-_{\omega 2}$. Because we assume elastic scattering and neglect mode conversion, the heat flux equality condition must

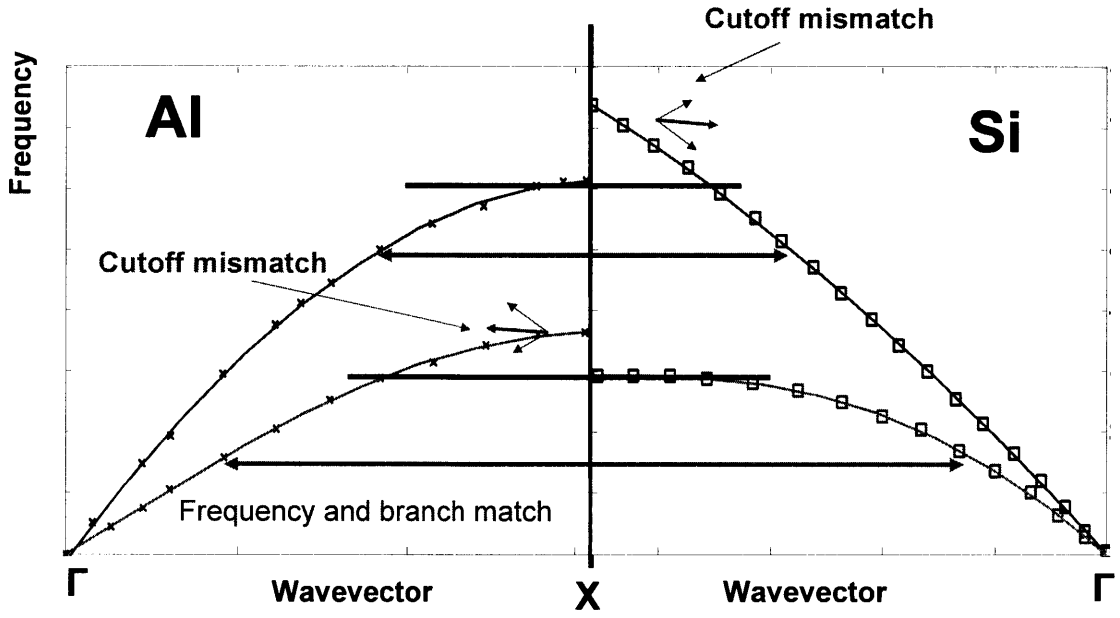

Figure 3-2: Phonon dispersions of Al (left) and Si (right). Scattering is permitted between phonons of the same polarization and frequency. High frequency phonons lacking a corresponding state are diffusely backscattered, indicated by the cutoff mismatch in the figure.

be satisfied for each frequency and polarization. The condition is:

$$q_1^+ = \int_0^1 f_{\omega 1}^+ v_{\omega 1} \mu d\mu \tag{3.8}$$

$$q_2^- = \int_{-1}^0 f_{\omega 2}^- v_{\omega 2} \mu d\mu \tag{3.9}$$

$$f_{\omega 2}^+ v_{\omega 2} = 2\left(T_{12}(\omega) q_1^+ - R_{21}(\omega) q_2^-\right) \tag{3.10}$$

$$f_{\omega 1}^- v_{\omega 1} = 2\left(-T_{21}(\omega) q_2^- + R_{12}(\omega) q_1^+\right) \tag{3.11}$$

Here $T_{12}(\omega)$ is the transmission coefficient from side 1 to 2, $R_{21}(\omega)$ is the reflection coefficient from side 2 back into side 2, and so on.

Under the assumption of elastic scattering and the neglect of mode conversion, some high frequency phonons are unable to transmit from one material to the other due to a lack of a state. For Al and Si, this occurs for phonons in the Al transverse branch and the Si longitudinal branch. These phonons are not able to transmit and therefore have zero transmissivity; this is indicated by 'cutoff mismatch' in Fig. 3-2.

Previous analyses did not consider cutoff frequency mismatches between two materials or frequency dependent transmission and reflection coefficients, and it is necessary to reexamine the relations between the coefficients to ensure that frequency dependence is properly incorporated.

There are several restrictions on the values of the transmission and reflection coefficients so that the principle of detailed balance and conservation of energy are satisfied. Let us assume the frequency-dependent transmissivity from medium 1 to medium 2, $T_{12}(\omega)$, is specified. The principle of detailed balance requires that when both materials are at an equilibrium temperature T, no net heat flux can transmit across the interface. Typically this condition is written as an integral over frequency,[47] but it can be shown that the principle of detailed balance applies for every phonon mode on each side of the interface.[90] The condition is:

$$T_{12}(\omega) f^0_{\omega 1}(T) v_{\omega 1} = T_{21}(\omega) f^0_{\omega 2}(T) v_{\omega 2} \tag{3.12}$$

Thus, even if $T_{12}(\omega)$ is frequency independent, $T_{21}(\omega)$ will in general be frequency dependent. Because we have assumed diffuse scattering, none of the transmission or reflection coefficients are angle-dependent and no further restriction is necessary.

Note that because $f^0_\omega(T)$ depends nonlinearly on T, temperature cannot be extracted from Eq. 3.12, meaning that the relationship between $T_{12}(\omega)$ and $T_{21}(\omega)$ required to satisfy detailed balance will change depending on the phonon temperature. However, due to the small deviations from the equilibrium temperature T_0 considered here, to excellent approximation detailed balance can be satisfied for all the phonons by evaluating Eq. 3.12 at T_0.

The rest of the relations between the transmission and reflection coefficients can be derived by enforcing an equality of the heat fluxes on each side of the interface,[47] giving:

$$R_{12}(\omega) = 1 - T_{12}(\omega) \tag{3.13}$$

$$R_{21}(\omega) = 1 - T_{21}(\omega) \tag{3.14}$$

All of these conditions must be satisfied at every frequency and polarization.

Finally, the transmissivity $T_{12}(\omega)$ can be related to the interface conductance G by calculating the heat flux and equivalent equilibrium temperature on each side of the interface.[7] The interface conductance is defined as $G = q/\Delta T$, where q is the heat flux at the interface and ΔT the temperature difference across the interface. The heat flux depends on the transmissivity, and therefore will be different from the results derived previously[7] due to the frequency dependence of the transmissivity.

The temperature difference ΔT is difficult to define consistently. Assuming that $f^+_{\omega 1}$ and $f^-_{\omega 2}$ have some emitted phonon temperature T_{e1} and T_{e2}, respectively, $f^+_{\omega 2}$ and $f^-_{\omega 1}$ will be composed of reflected and transmitted phonons at these different temperatures and will be strongly out of equilibrium.[7] It has been shown that the appropriate quantity to use is the equivalent equilibrium temperature, which represents the temperature of the distribution that a non-equilibrium phonon distribution would reach if it were to relax adiabatically to equilibrium.[7] Thus, even though the forward and backward going phonons are strongly out of equilibrium, using the equivalent equilibrium temperature allows the results to be compared to the Fourier's law result which assumes local thermal equilibrium.

Using these results, the modified relation between the interface conductance and transmissivity is:

$$\left\langle T_{12}(\omega) f^0_{\omega 1} v_{\omega 1} \right\rangle = \frac{2}{\langle Cv \rangle_1^{-1} + \langle Cv \rangle_2^{-1} + (2G)^{-1}} \tag{3.15}$$

where $\langle \cdot \rangle$ denotes integration over frequency. The details of the derivation are presented in appendix B. If the transmissivity is frequency independent then this formula reduces to the result derived previously.[7] It is important to remember that this formula assumes that the incoming distributions to the interface, $f^+_{\omega 1}$ and $f^-_{\omega 2}$, have a temperature. If these distributions are also out of equilibrium, then it is not possible to relate the interface conductance and transmissivity. In this case, with the transmissivity specified, the interface conductance will change with time until the two incoming distributions do have a temperature, at which point Eq. 3.15 will be valid

and the interface conductance will become a constant. Due to the transient nature of the heat transport studied here, the two distributions never exactly achieve a thermal distribution, and so the thermal conductance can still change slowly with time.

3.3.4 Phonon dispersion and relaxation times

We now need to specify the dispersion and relaxation times for both the Al film and the Si substrate. We use the experimental dispersion in the [100] direction for both Al and Si.

We assume a constant relaxation time τ for all modes in Al; the value $\tau = 10$ ps is chosen to yield the desired lattice thermal conductivity $k \approx 20$ W/mK. For Si, we use relaxation times for phonon-phonon scattering extracted from molecular dynamics simulations[91] but with an empirical term $\exp(-\theta/T)$ to extend the relaxation times to lower temperatures.[42] We also add boundary scattering and impurity/isotope scattering, important at $T < 100$ K, and combine the relaxation times using Matthiessen's rule $\tau^{-1} = \sum_i \tau_i^{-1}$. The relaxation times are:

$$\tau_L^{-1} = A_L \omega^2 T^{1.49} \exp(-\theta/T) \tag{3.16}$$

$$\tau_T^{-1} = A_T \omega^2 T^{1.65} \exp(-\theta/T) \tag{3.17}$$

$$\tau_I^{-1} = A_I \omega^4 \tag{3.18}$$

$$\tau_B^{-1} = w_b \tag{3.19}$$

where L and T denote longitudinal and transverse, respectively. The parameters used are specified in table 3.1.

The thermal conductivity is calculated with the above relaxation times using the kinetic theory expression for the thermal conductivity:

$$k = \frac{1}{3} \sum_p \int_0^{\omega_m} C_\omega v_\omega^2 \tau_\omega d\omega \tag{3.20}$$

where the sum is over polarization p. The exact dispersion is used in this calculation. As in Holland's model,[42] the additive term accounting for normal scattering from

Table 3.1: Parameters used in the phonon relaxation time models for natural silicon.

Parameter	A_L [$K^{1.49}/s$]	A_T [$K^{1.65}/s$]	θ [K]	A_I [s^3]	w_b [s^{-1}]
Value	2×10^{-19}	1.2×10^{-19}	80	3×10^{-45}	1.2×10^{6}

Callaway's model is neglected.[41]

3.3.5 Numerical details and boundary conditions

We solve the BTE numerically using a discrete ordinates method.[82] Both the angle and frequency are discretized using Gaussian quadrature to minimize the number of points required. The angle is discretized into $N_\mu = 40$ points. The frequency discretization is more complicated because of the cutoff frequency mismatch for zone-edge phonons. Integrals involving the phonon dispersion are split into two integrals, one over the modes in common between Al and Si and another over the remaining modes, which in this case is the high frequency modes of the Al T branch and the Si L branch. These integrals are then separately discretized using Gaussian quadrature. An explicit first-order finite difference method is used to discretize the spatial and temporal derivatives.[82]

In addition to the interface conditions, one boundary condition is required for each angle $-1 < \mu < 1$. The distribution function must be specified for angles $0 < \mu < 1$ at $x = 0$, or the top of the metal film, and for angles $-1 < \mu < 0$ at $x = L$, or the bottom of the substrate, where L is the length of the numerical domain. We choose the boundary condition at $x = 0$ to be diffuse reflection so that this surface is adiabatic. For the boundary condition at $x = L$, the type of boundary condition used ideally should not matter if the domain is sufficiently long. We use adiabatic or constant temperature boundary conditions and verify that the solution ot the BTE is the same in both cases.

The initial condition is an exponentially decaying phonon temperature distribution, with the $1/e$ depth of the temperature profile taken to be the light absorption depth in Al, approximately 7 nm for visible wavelengths.[92]

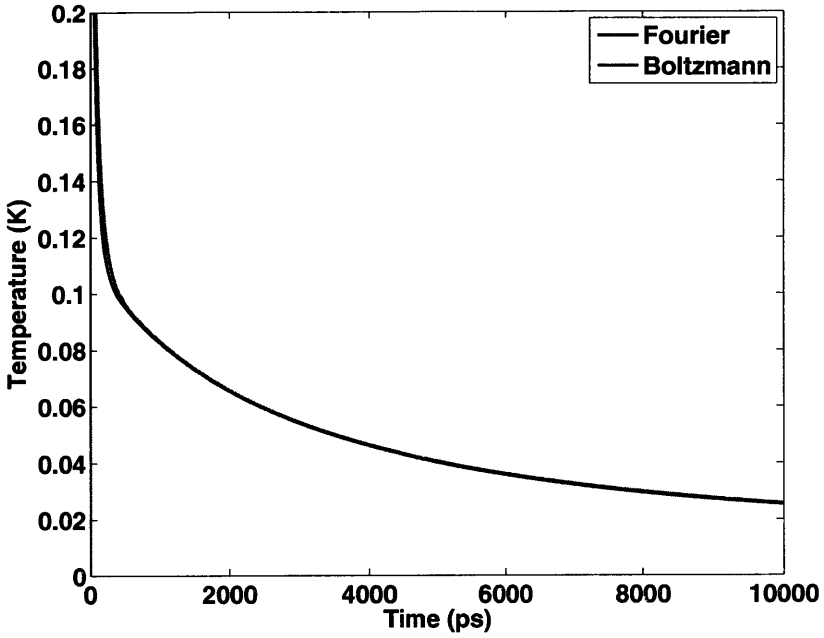

Figure 3-3: Lattice surface temperature versus time predicted by the BTE and the heat equation with truncated relaxation times to 10 ps at 300 K. The curves are almost identical.

The interface transmissivity $T_{12}(\omega)$ is calculated using Eq. 3.15 for a particular value of G specified at the beginning of the simulation. The rest of the transmission and reflection coefficients can then be calculated as described in section 3.3.3.

3.4 Results

We first consider a test case. In this simulation, performed at T=300 K, the maximum relaxation time was truncated to 10 ps, putting the transport easily into the diffusive limit. In this case, the solution from the BTE should be very close to the Fourier law solution. Fig. 3-5 shows the surface temperature of the metal film versus time predicted by the BTE and by the heat equation. The length of the domain is 3 μm. To verify that the finite length of the domain does not influence the solution, two different boundary conditions, adiabatic and constant temperature, were employed at the edge of the substrate, and the length of the domain was varied. In all cases

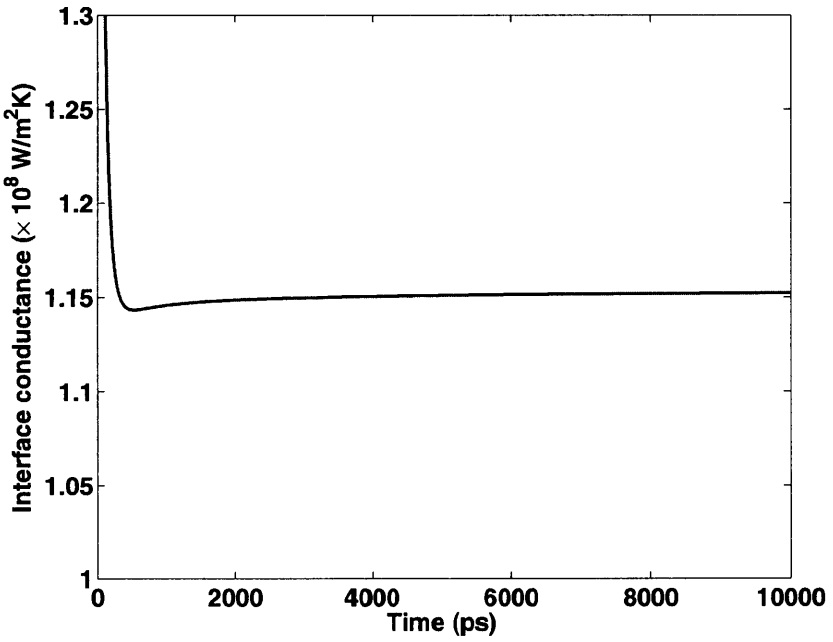

Figure 3-4: Calculated interface conductance G from the BTE with truncated relaxation times to 10 ps at 300 K. The result is close to the specified value of 1.1×10^8 W/m^{2}K, which is chosen at the beginning of the simulation by calculating the transmissivity from Eq. 3.15 using a particular value of G.

the solutions were nearly identical, indicating that the spatial domain is sufficently large. To verify convergence of the numerical solution, the number of spatial points, angle points, and frequency points were all increased; the solution again remained identical.

We can also calculate the interface conductance and compare it to the value specified at the beginning of the simulation. The result is shown in Fig. 3-4; the calculated result is close to the specified value of 1.1×10^8 W/m^{2}K.

This test case demonstrates that the calculation successfully reproduces the diffusive limit and is operating properly. We now perform the same simulation, only with the restriction on relaxation times removed; relaxation times are now given by the equations in Sec. 3.3.4 and can be arbitrarily long. The same figures as before, lattice surface temperature versus time and interface conductance versus time, are shown in Figs. 3-5 and 3-6, respectively.

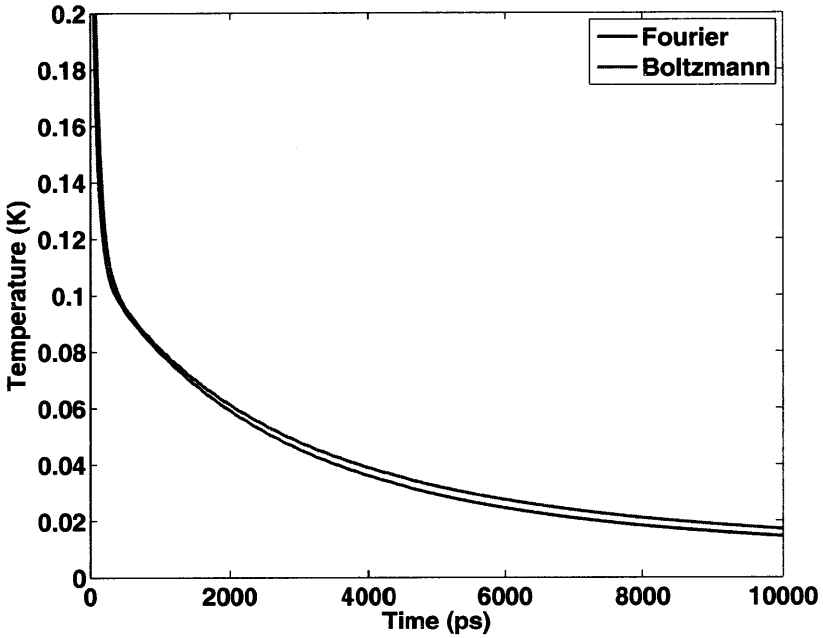

Figure 3-5: Lattice surface temperature versus time predicted by the heat equation and BTE with full relaxation times at 300 K. The two curves do not match exactly, indicating the transport is in the quasi-ballistic regime.

This calculation gives an unexpected result. Examining Fig. 3-5, we see that at room temperature the solution from the BTE does not match that from diffusion theory, indicating ballistic effects are present. This is somewhat surprising, considering that estimates of the average phonon relaxation times are around 50 ps in Si.[47] This illustrates the danger of using the concept of an average relaxation time in many materials. As mentioned in Sec. 3.2, despite the average relaxation time being relatively short, more detailed analyses of phonon transport reveal that MFPs and relaxation times can vary by 5-6 orders of magnitude over the Brillouin zone. In Si, it is estimated that 40% of the thermal conductivity is contributed by phonons with MFP longer than 1 μm.[91] In terms of the present one-dimensional simulation, these long MFP (and relaxation time) phonon modes do not scatter over the timescale of the simulation, resulting in a non-equilibrium phonon distribution and the failure of Fourier's law, which assumes local thermal equilibrium. From Fig. 3-5, we see that the surface temperature decay curve is shallower than the Fourier law prediction, indicating that the heat transfer in the quasi-ballistic case is smaller than in the diffusive case. This phenomenon of "ballistic thermal resistance" in quasi-ballistic transport has been demonstrated experimentally in sapphire,[93] in semiconductor alloys,[94] and in the subsequent chapters of this thesis.

Examining the interface conductance in Fig. 3-6, we see an additional unexpected result. Instead of a constant interface conductance close to the value of 1.1×10^8 W/m^{2}K specified, the interface conductance changes with time. The reason for this was discussed in Sec. 3.3.3. To define an interface conductance, the incoming distributions at the interface must have a thermal distribution. As shown earlier, due to the long relaxation times of some phonons, a local thermal equilibrium does not exist over the short timescales of this simulation, making it impossible to define a constant interface conductance.

To better understand this effect, let us examine the angle-integrated intensity for each frequency normalized to the specific heat:

$$T_\omega = \frac{\int_{-1}^{1} f_\omega d\mu}{C_\omega} \tag{3.21}$$

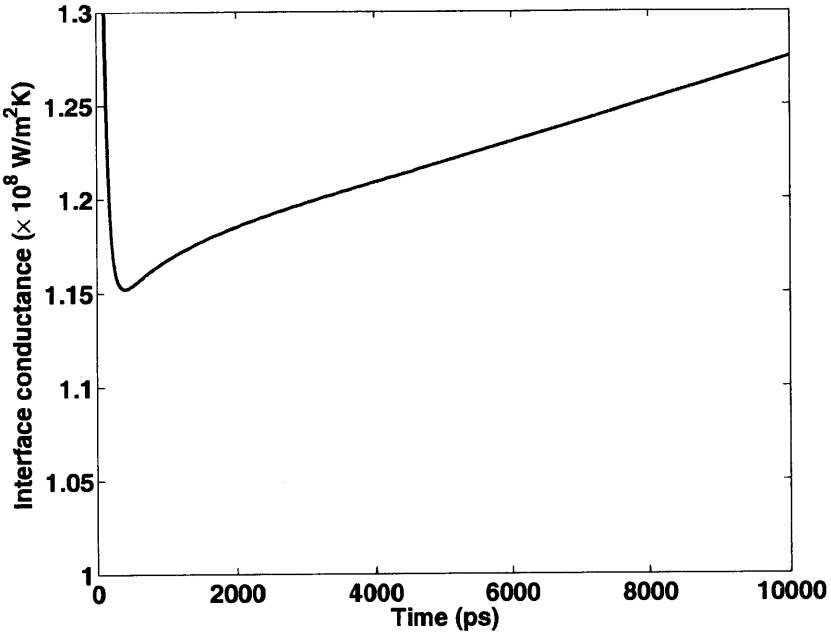

Figure 3-6: Calculated interface conductance G from the BTE at 300 K. The interface conductance is not constant as in the diffusive case.

This gives a 'temperature' for each frequency. If the distribution is in thermal equilibrium this temperature will be constant for all frequencies. This quantity is plotted at t=10 ns for the 10 ps truncated and full relaxation times. As shown in Figs. 3-7 and 3-8, the 10 ps case has a well defined temperature even at the interface, while the full relaxation time case does not. This indicates that the phonon distribution is not in thermal equilibrium for the full relaxation time case, as expected. Therefore, the assumption made in the derivation of the relation between thermal conductance and transmissivity is not strictly valid, and it is not possible to define a constant interface conductance.

These ballistic effects are much more apparent at T< 300 K, where phonon relaxation times can be substantially longer than 1 μs. A typical result is shown in Fig. 3-9 for T=100 K. There is a much more marked difference between the heat equation and BTE solutions, indicating that the transport is quasi-ballistic and a local thermal equilibrium does not exist.

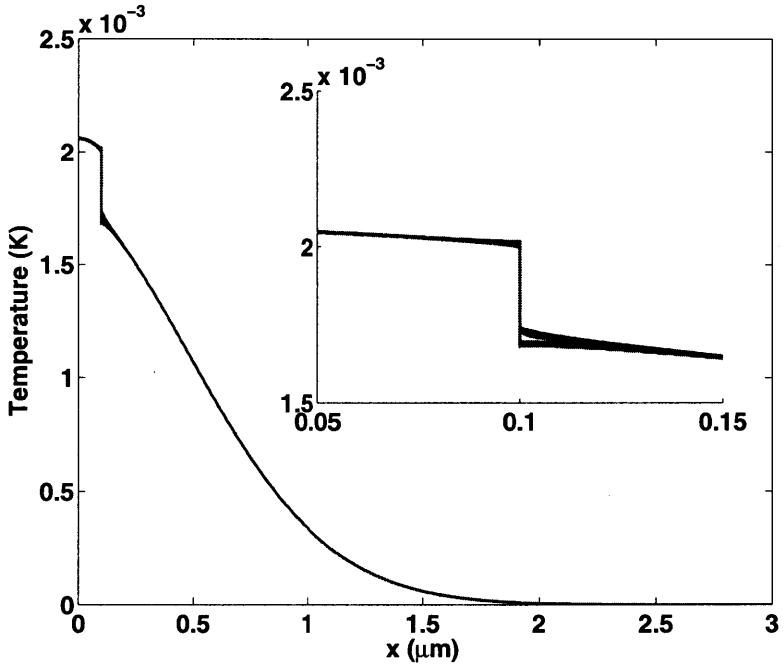

Figure 3-7: Frequency-dependent 'temperatures' for truncated relaxation times to 10 ps case at 300 K. That the temperatures are almost identical indicates that the phonons have a thermal distribution and are in local thermal equilibrium.

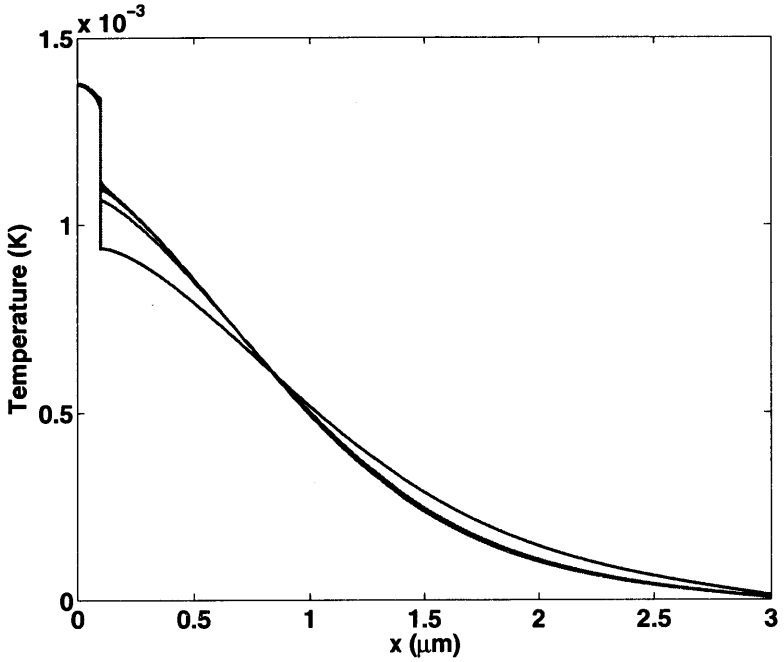

Figure 3-8: Frequency-dependent 'temperatures' for the full relaxation time case at 300 K. The distribution is out of thermal equilibrium, especially at the interface.

3.5 Discussion

From the results presented, it is clear that qualitatively, the solution of the phonon BTE compared to the Fourier's law solution contains information about relaxation times. In particular, if the BTE solution is different than the Fourier's law solution, we can conclude that some phonon modes have relaxation time longer than the timescale of the simulation. The magnitude of the difference between the two solutions also gives some information about relaxation times: the longer the relaxation times, the larger will be the deviation and vice versa.

We would like to better understand which phonon modes are responsible for these discrepancies and determine how to extract information about relaxation times. As discussed in the previous section, quasi-ballistic transport results in a smaller heat flux than predicted by Fourier's law, corresponding to a smaller effective thermal conductivity. We can interpret the value of this effective thermal conductivity using

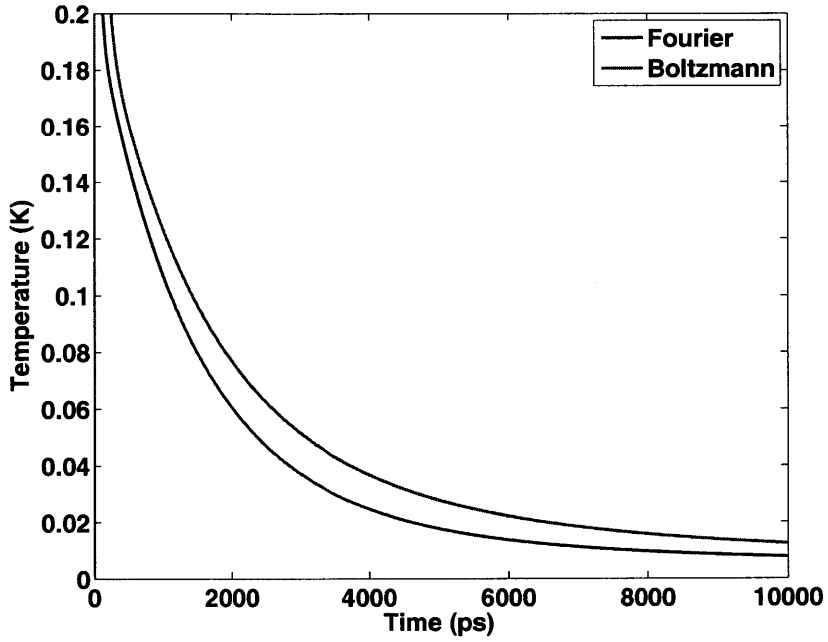

Figure 3-9: Lattice surface temperature versus time predicted by the heat equation and BTE with full relaxation times at T = 100 K. Ballistic effects are more apparent at low temperatures where relaxation times are longer.

an earlier work by Koh and Cahill.[94] In their work, a modulation-frequency dependence of the thermal conductivity of semiconductor alloys was observed, with a lower thermal conductivity measured at higher modulation frequency. They explained this result as follows: as the modulation frequency of the heating pump beam is increased, the cross-plane thermal penetration depth l_d becomes shorter, increasing the fraction of phonons which have MFP longer than the penetration depth. The larger fraction of ballistic phonons results in a smaller heat flux and hence lower effective thermal conductivity, similar to that observed in our numerical simulations. The important component of their interpretation is that the difference between the true and measured thermal conductivity is the contribution by phonons with $\Lambda_\omega > L_{pd} = 2 \times l_d$. In other words, the effective thermal conductivity in the quasi-ballistic case is due to phonons with $\Lambda_\omega < L_{pd}$; phonons with $\Lambda_\omega > L_{pd}$ do not contribute to the thermal conductivity measured by the experiment.

We can use this interpretation to better understand our numerical simulations. As a first step, we examine the single-pulse BTE response; the accumulation effect of multiple pulses will be considered later in the chapter. We fit the single-pulse BTE solution with a Fourier's solution using an effective thermal conductivity k_{eff} and interface conductance G_{eff}, both of which will be smaller than the values specified in the BTE computation due to quasi-ballistic effects. This fit is demonstrated in Fig. 3-10 for T=300 K. The BTE solution, in which $k = 140$ W/mK and G=1.1×10^8 W/m^{2}K were specified, matches a Fourier's law solution with different effective values of $k_{eff} =$ 100 W/mK and $G_{eff} = 1.0 \times 10^8$ W/m^{2}K. Under Koh and Cahill's interpretation, the discrepancy between these two thermal conductivity values is due to phonon modes with $\Lambda_\omega > L_{pd}$. For the single pulse case, $L_{pd} \approx 2 \times \sqrt{\pi \alpha t}$, where $\alpha \approx 10^{-4}$ W/m^{2}K is the thermal diffusivity of silicon at T=300 K and $t \approx 5$ ns is the approximate timescale of the experiment. Using these values, we find that $L_{pd} \approx 2.5 \mu m$, suggesting that phonons with MFPs longer than about 3 μm do not contribute to the measured thermal conductivity. To determine if this value is reasonable, we use the frequency-dependent model of thermal conductivity described in section 3.3.4 to calculate the thermal conductivity excluding phonons with MFPs longer than $\sim 3 \mu m$. The result

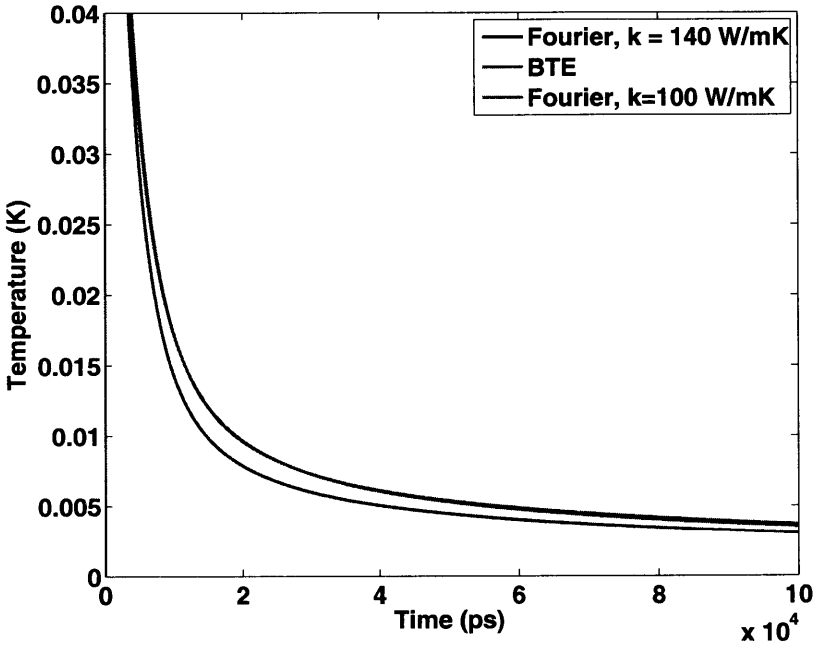

Figure 3-10: Fourier law solutions for k=140 W/mK and k=100 W/mK compared to the solution of the BTE for an aluminum film on silicon at T = 300 K. Even at room temperature, the BTE solution does not match that predicted by diffusion theory. Instead, the BTE solution almost exactly matches a Fourier's law curve with reduced effective thermal conductivity, indicating quasi-ballistic transport is occurring.

is $k \approx 100$ W/mK, in remarkable agreement with the value obtained from fitting the BTE solution.

The results of this fitting procedure for temperatures down to T=100 K are shown in table 3.2. At and below T = 100 K a satisfactory fit using Fourier's law is difficult to obtain for reasons that are presently unclear. However, above T=100 K, there is quite good agreement between the MFP cutoff values Λ_{co}, obtained from the frequency-dependent model of thermal conductivity, and twice the penetration depth L_{pd}. These results further support the hypothesis that phonons with $\Lambda_\omega > L_{pd}$ do not contribute to the measured thermal conductivity.

We can now see that we have made good progress towards our goal of measuring MFPs and relaxation times by studying the quasi-ballistic regime. The BTE calculation shows that when transport occurs over timescales comparable to relaxation

Table 3.2: Values of the effective (k_{eff}) and actual (k) thermal conductivities from the BTE solution at several different temperatures, along with the MFP cutoff values Λ_{co} required to achieve this thermal conductivity and the effective penetration depth L_{pd} at each temperature. The MFP cutoff values agree reasonably well with the effective penetration depth.

T [K]	k_{eff} [W/mK]	k [W/mK]	Λ_{co} [μm]	L_{pd} [μm]
300	100	140	2.5	2.4
250	130	190	3.0	2.8
200	170	273	4.0	3.6
150	230	429	5.3	5.1
100*	450	815	20	8.7

* Poor fit of BTE solution

times, the transport deviates from the predictions of heat diffusion theory. By analyzing the deviations with simple models, we are able to extract information about phonon relaxation times. For the calculations in silicon, the results indicate that phonons with MFP longer than approximately 3 μm contribute 40 W/mK to the total thermal conductivity at room temperature. Unfortunately, if we consider only the single-pulse response there does not seem to be any way to change the penetration depth so that we can measure the MFP distribution at more than one point. This issue will be solved in chapter 5, where we introduce an experimental technique which can measure MFPs over a wide range of length scales and materials.

3.6 Unresolved puzzles

Despite the apparent consistency of our numerical analysis, there are two unresolved puzzles. First, while the single-pulse numerical simulations suggest that quasi-ballistic effects should be observable at room temperature in silicon at nanosecond timescales, experimentally the correct thermal conductivity is routinely measured using standard ultrafast techniques, though in these measurements the accumulation effect of multiple pulses is important. The reason for this discrepancy is presently unknown and warrants further investigation.

Second, our simulation is presently not able to explain the modulation frequency dependence of thermal conductivity observed in Koh and Cahill's experiment. So far, we have only numerically solved for the single-pulse response of the BTE. In a typical transient thermoreflectance experiment, however, an accumulation effect occurs where the observed response of a sample is actually due to multiple pulses because of the fast repetition rate (80 MHz, or one pulse every 13 ns) of the laser.[95] Koh and Cahill's observation of modulation frequency-dependent thermal conductivity can only be interpreted using this multi-pulse response.

The multi-pulse response can be calculated from the single-pulse response using a procedure described in Ref. [96]. Briefly, the procedure involves adding later portions of the single-pulse response multiplied by a phase factor to the beginning of the single-pulse response:

$$Z(t) = \sum_{q=0}^{\infty} h(qT + t)e^{-i\omega_0(qT+t)} \tag{3.22}$$

where $Z(t)$ is the multi-pulse response at time t, h is the single-pulse response, T is the time between laser pulses, and ω_0 is the modulation frequency. The modulation frequency affects the multi-pulse response by changing the phase factor multiplying the single-pulse response.

In the diffusive limit, the multi-pulse response should correspond to the same thermal conductivity of the impulse response regardless of the modulation frequency used. Therefore, if h is a Fourier's law response with a particular thermal conductivity, then the multi-pulse response must correspond to the same value of thermal conductivity for all modulation frequencies. In order to measure a modulation-frequency dependent thermal conductivity, then, the single-pulse response must deviate from the Fourier's law response so that the multi-pulse response at different modulation frequencies corresponds to different thermal conductivities. However, as can be seen in Fig. 3-10, the BTE solution can be fit using a Fourier's law response with an effective thermal conductivity. Because the BTE response and Fourier's law response with effective properties are essentially identical, the multi-pulse response of the BTE must yield a thermal conductivity equal to its original effective value regardless of

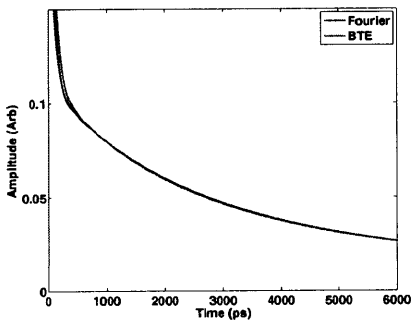

(a) Amplitude signal, ω_0 =15 MHz

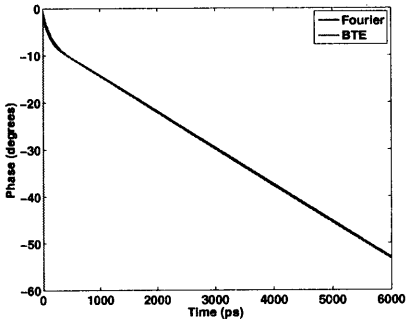

(b) Phase signal, ω_0 =15 MHz

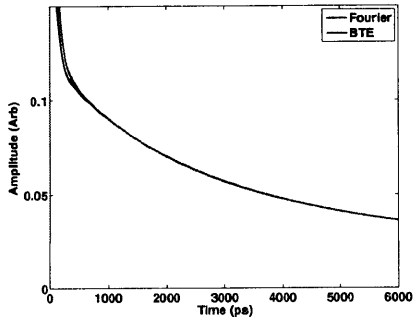

(c) Amplitude signal, ω_0 =6 MHz

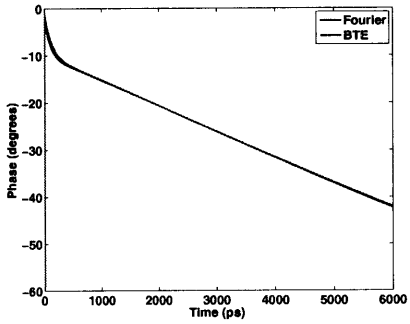

(d) Phase signal, ω_0 =6 MHz

Figure 3-11: Typical multi-pulse responses at different modulation frequencies calculated from the single-pulse response for the BTE and Fourier's law. Both fits correspond to effective thermal conductivity k_{eff} = 100 W/mK and interface conductance $G = 1 \times 10^8$ W/m^{2}K and therefore do not not predict a modulation-frequency dependence of thermal conductivity.

the modulation frequency. Thus, the present BTE calculation does not predict a modulation-frequency dependent thermal conductivity.

This lack of frequency dependence is demonstrated in Fig. 3-11. Here, we have used Eq. 3.22 to calculate the multi-pulse response of the BTE solution and the Fourier's law solution with the effective properties k_{eff}=100 W/mK and $G = 1 \times 10^8$ W/m^{2}K. As the figure shows, this same set of effective parameters can explain both the amplitude and phase responses of the BTE at two different modulation frequencies. We have calculated the multi-pulse responses at several different frequencies in the MHz range and obtained the same result. Calculating the multi-pulse response at lower modulation frequencies is difficult because up to 1 μs of the BTE solution must be computed, but based on the above discussion we do not expect to observe a frequency dependence even at these lower frequencies.

It is interesting to note that experimentally, Koh and Cahill did not observe a modulation frequency effect in pure silicon. The effect was only observed for semiconductor alloys. It would therefore be useful to repeat the BTE calculations with relaxation times corresponding to those for alloys and perform the same type of analysis. Perhaps in this case the BTE would predict the experimentally observed modulation frequency effect.

3.7 Conclusion

In this chapter we took a first step towards determining how we can measure MFPs and relaxation times in materials. We showed that these properties are difficult to measure in the diffusive regime because the carriers have already relaxed. Instead, we must study the quasi-ballistic regime, where transport occurs on scales comparable to MFPs and relaxation times. To further investigate this regime, we numerically solved the frequency-dependent Boltzmann transport equation including a frequency-dependent interface condition. We showed that quasi-ballistic heat transfer will differ from the predictions of heat diffusion theory, and that by analyzing the deviations with simple models we can extract very useful information about MFPs and relaxation

times. In chapter 5 we introduce a new technique to experimentally measure MFPs using observations of quasi-ballistic transport with our ultrafast pump-probe system. First, in chapter 4 we briefly describe our experimental pump-probe system and the modifications we have made in recent years to make these measurements more efficiently.

Chapter 4

Modifications to the pump-probe experiment

4.1 Background

As discussed in the last chapter, studying heat transfer in the quasi-ballistic regime allows us to extract information about phonon MFPs and relaxation times. To experimentally study transport in this regime, length and time scales must be comparable to MFPs and relaxation times. This implies we need nanometer to micron spatial resolution and picosecond time resolution. These requirements, though strict, can be mostly satisfied using ultrafast pump-probe techniques. This type of optical experiment offers sub-picosecond time resolution and micron spatial resolution, which is sufficient to study the quasi-ballistic regime in materials which have phonons with MFPs in the micron range.

In this chapter we describe our experimental pump-probe setup and the modifications which have been made since the setup was first constructed. Our experiment is based on a pulsed Ti:sapphire laser with a fundamental harmonic at 800 nm and an 80 MHZ repetition rate. A schematic of the system is shown in Fig. 4-1.[96] Because the principle of the system and many experimental details are extensively described in Ref. [96], only a brief review will be presented here.

The principle of pump-probe is as follows. A laser pulse is split into two pulses, a

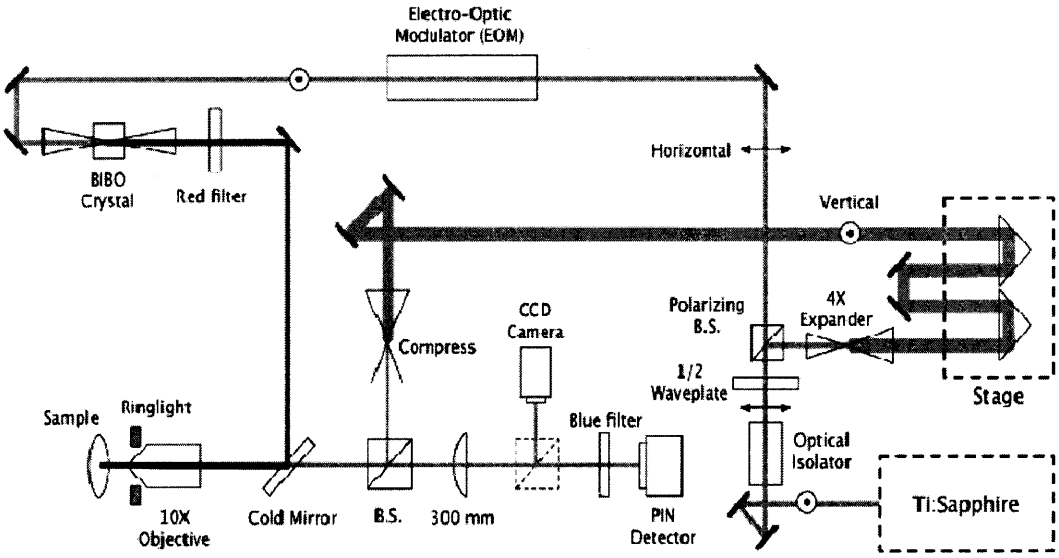

Figure 4-1: Schematic of the pump-probe system in the Rosenhow Kendall Heat Transfer Laboratory (from Ref. [96]). A Ti:Sapphire laser emits a pulse train of 800 nm, 250 fs pulses at a rate of 80 MHz. The pulse train is split into pump and probe beams using a 1/2 waveplate and beamsplitter. The probe is directed to a mechanical delay line and subsequently to the sample. The pump is modulated using an electro-optic modulator (EOM), frequency doubled to 400 nm using a Bismuth Triborate crystal (BIBO), and directed to the sample at the lower left of the figure. The reflected probe light is send to a fast PIN detector (amplified or unamplified photodiode); this signal is then sent to a lock-in amplifier.

pump and a probe. The pump pulse train is modulated at some frequency to allow lock-in detection. In our implementation of the experiment, the pump pulses are frequency doubled using a BIBO (Bismuth Triborate, Newlight Photonics) crystal to allow easier removal of the pump pulses at the detector using color filters. A sample consists of a substrate of interest coated with a thin ($\approx$ 100 nm) metal transducer film, typically Al. The pump beam is focused to a spot of $1/e^2$ diameter between 10-60 μm, heating up the sample. This causes a change in the optical reflectivity of the film, which is monitored using a variably time-delayed probe pulse train. The time delay is accomplished by using a mechanical stage to create a variable difference in path length. The probe has a $1/e^2$ diameter of around 10 μm. For small temperature rises induced by the pump beam, the change in optical properties of the film will be linearly related to the change in temperature of the film. Therefore, by monitoring the change in optical properties for different time delays of the probe pulses, we can measure the temperature decay curve due to the impulsive heating from the pump pulse. The shape of the temperature decay curve contains information about the thermal properties of the system, so by fitting this curve to a thermal model, we can extract the thermal properties of the material system. Typically, the interface conductance G between the metal film and substrate and the thermal conductivity k of the substrate are extracted.

Further details of the experiment and the thermal model are extensively discussed in Ref. [96] and will not be presented here. Instead, we discuss the changes that were made to make the system more stable and robust and simplify the task of data collection.

4.2 Modifications to signal detection circuitry

One of the most helpful modifications we have made is improving the circuitry used to extract the desired signal from the photodiode and send it to the lock-in amplifier. To review, the pump pulse train is modulated at some frequency, typically between 1-15 MHz, to enable lock-in detection. This causes a change in temperature at the

surface of the metal film at the modulation frequency, which is detected by the probe pulse train. Therefore, when the probe pulses are focused into the photodiode, the resulting photocurrent contains very strong frequency components at multiples of 80 MHz, the repetition rate of the laser, and a much weaker component at the modulation frequency which contains the information we wish to extract. This is very similar to amplitude modulation of radio waves, with a lower frequency signal modulating an 80 MHz "carrier" wave. The challenge is to convert the photocurrent at the modulation frequency, which may be as small as 1 pA, to a usable voltage which can be accurately detected by the lock-in amplifier while removing the carrier signal.

In the first generation of the system, this challenge was made even more difficult because of the way in which the modulation was performed. Originally the pump beam was modulated with a square wave, which contains frequency components at odd harmonics (3, 5, 7, ...) of the fundamental. Unfortunately, our lock-in amplifier also mixes the incoming signal with a square wave, allowing these odd harmonics to contaminate the desired signal at the fundamental modulation frequency. To remove these odd harmonics, it was necessary to use a resonant LC filter with a high quality factor. While this setup attenuated the odd harmonics and magnified the voltage measured by the lock-in amplifier with a gain of 10, it also required the filter to be changed in order to change the modulation frequency. This made data collection laborious and time-consuming.

We solved this problem and removed the need for the resonant filters, allowing us to change modulation frequencies completely automatically, as follows. First, we replaced the original digital electro-optic modulator (EOM) amplifier (Conoptics 25D) with an analog amplifier (Conoptics 25A). The analog amplifier amplifies whatever waveform is sent to it, in contrast to the digital amplifier, which is capable of only square wave (on-off) modulation. By modulating the pump beam with a sine wave rather than square wave, we remove the odd harmonics, and hence the need for a resonant filter.

Second, we use an active transimpedance amplifier (TIA) to convert and amplify the photocurrent into a usable voltage signal. Amplified detectors can be easily

purchased and provide a gain of ≈ 2000 V/A, amplifying the small photocurrent into the μV range. Our detector has a bandwidth of approximately 15 MHz, ensuring that the signal at the modulation frequency is amplified while the 80 MHz carrier signal is not.

These two modifications remove the need for the resonant filter and make changing the modulation frequency completely automated. To make the system more robust and stable, we make a few additional modifications. First, we place a band-pass filter between the output of the amplified photodetector and the lock-in. This band pass filter passes 20 kHz $< f <$ 30 MHz, the typical range of the modulation frequency, while further attenuating the carrier signal at 80 MHz. The removal of the interfering carrier signal allows us to place the lock-in amplifier at a more sensitive setting, making the whole setup less susceptible to external EM interference and internal coherent pickup inside the instrument.[97]

Second, we moved the lock-in amplifier and signal generator as close to the detector as possible to minimize the length of the coaxial cables. While coaxial cable ideally should be shielded, a small amount of radiation at the modulation frequency can still be radiated and picked up by signal cables. This is particularly true for the coaxial cables from the EOM, which transmit high voltages and thus radiate strongly. Shortening the signal cables minimizes external EM interference and makes the system far more stable. A picture of our cable setup is shown in Fig. 4-2.

Third, we added an automated beam blocker (DCH50 chopper, Electro-optical Products Corporation, with USB-6008 DAQ board, National Instruments) to null any constant offset voltages at each frequency. There are many sources of signal at the modulation frequency which add a constant offset to the signal measured by the lock-in amplifier, including radiation from EOM cables and internal pickup in the lock-in itself. These offset voltages must be nulled, with the pump beam blocked,[96] in order to obtain a measurement which can be directly compared to our model's predictions. By automating the blocking of the pump beam, this cancellation can be performed automatically, significantly easing the task of data collection.

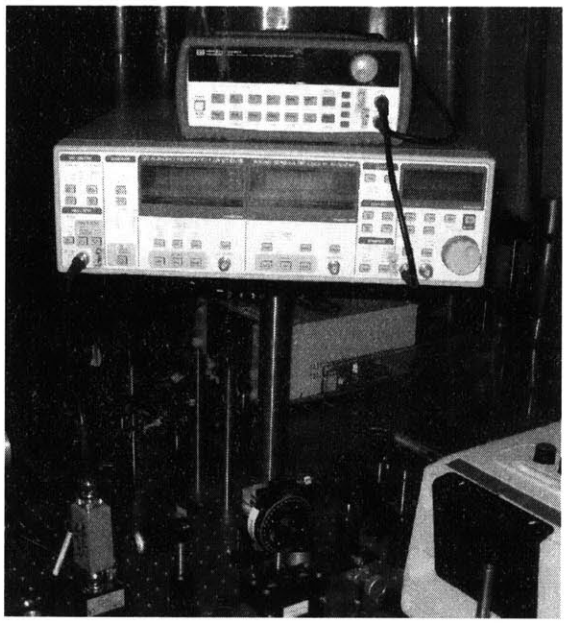

Figure 4-2: Demonstration of good cable practices in our experiment. Note the short cables from the photodiode and function generator to the lock-in amplifier.

4.3 Correction of laser beam astigmatism

The ideal fundamental mode from an oscillator cavity is a symmetric Gaussian beam. A Gaussian beam is completely characterized by the beam diameter and the radius of curvature.[98] The diameter of the beam is typically characterized by the $1/e^2$ diameter, or the width of the beam where the intensity $I = |\mathbf{E}|^2$ has dropped to $1/e^2$ of its peak value, where $\mathbf{E}$ is the electric field. The radius of curvature specifies how fast the wavefront is converging or diverging.

However, real lasers often exhibit astigmatism, meaning the beam diameter and radius of curvature are different in different directions. In our laser, the beam exiting the oscillator has diameters of 1.7 and 1.0 mm and beam divergence angles (related to the radius of curvature) of 0.2 and 0.7 mrad in the X and Y directions, respectively.

This astigmatism makes tightly focusing the beam difficult. While the size of the beam does affect the beam waist, the more difficult problem is the difference in beam divergence angle. Specifically, this difference causes the Y beam waist to occur approximately 75 μm behind the X beam waist, meaning the X and Y foci do not

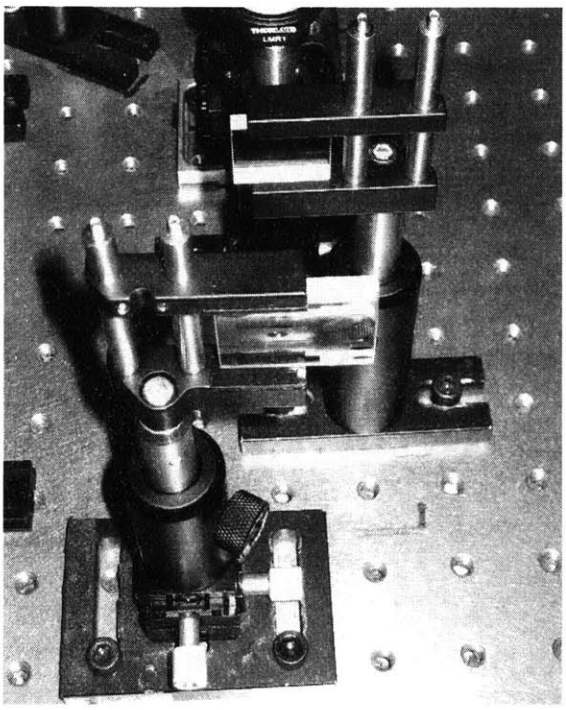

Figure 4-3: Cylindrical lenses (focal lengths -80 and 130 mm) used to correct the probe beam astigmatism.

occur at the same location. Thus, while the beam waists in each direction may be, for example, 8 μm, the actual minimum waist that is achieved at any point is somewhat bigger, and the beam is actually only round at exactly one point. In practice, this point is very difficult to find.

Because the probe weights the metal film optical properties according to its shape, the signal carried by the probe can depend strongly on its shape. This is particularly true in materials with high thermal conductivity, where radial conduction is important and the heat transfer induced by the pump and sampled by the probe will be affected by the intensity profiles of each beam.[96] Because our model assumes symmetric Gaussian beams, it is important to make sure the experiment is consistent with the model.

While in principle it should be possible to directly correct the output of the oscillator at the beginning of the beam line, we were not able to align the lenses correctly to accomplish this. Since the pump beam is relatively circular due to other optics along its path, we decided to correct the probe after the delay line to ease the alignment. We use a pair of cylindrical lenses to control the beam divergence angle in one dimension, and hence the location of the beam waist in that dimension, so that it more closely matches the beam waist location of the other dimension. Figure 4-3 shows the lenses used. These lenses slightly decrease the beam divergence angle so that the Y beam waist occurs closer to the X beam waist. This circularizes the probe beam to a diameter of approximately 11 μm.

One final point is that the BIBO crystal used to frequency double the pump beam can severely distort the pump beam shape and prevent diffraction-limited focusing if it is damaged. This was found to be the case for our 2 mm thick BIBO crystal. We replaced this crystal with a 1 mm BIBO crystal to minimize the temporal and spatial distortion of the pump pulse and were able to get diffraction-limited focusing afterwards. The damage threshold for our BIBO crystal is 4 GW/cm^2 for a 250 fs pulse at 800 nm. Care should be taken to ensure that the intensity remains well below this value.

4.4 Sample preparation and film quality

One of the most important procedures to get reproducible, stable data from the experiment is properly preparing the substrate and depositing a high quality metal film. The primary requirement of the film is that the change in reflectivity be linearly related to the change in temperature. This can only be satisfied if the incident pump and probe intensities are not too high and if the film is tightly bonded to the substrate. If any delamination occurs, or if the laser pulses damage the film, the data obtained is essentially meaningless. We adopted the following procedure to ensure reproducible results:

1. The sample surface must be cleaned thorougly to remove dust and organic contaminants from the surface. For Si, an appropriate cleaning solution would be a piranha solution (1:3 H_2O_2:H_2SO_4). Of course, the solution will depend on the particular substrate. If interface studies are desired, or if a high interface conductance is required, it is especially important to remove the native oxide layer prior to deposition. For Si, an 20:1 H_2O:HF dip is sufficient; this short procedure increases the interface conductance by a factor of 3, from $\approx 1 \times 10^8$ to $\approx 3 \times 10^8$ W/m^{2}K.

2. The film should be deposited under very high vacuum ($< 10^{-6}$ torr) to minimize impurities in the film. We have also found the electron beam evaporation consistently gives better films than does sputtering. The EBeamFP tool, a rapid loadlock evaporator at MIT, is ideal for our purposes and can finish an entire deposition procedure in under an hour. If film adhesion is a problem, a thin ($\approx$ 5 nm) Ti or Cr adhesion layer significantly improves the adhesion.

3. The power density of the pump and probe beams must not be too high or else the film can be damaged, or the change in reflectivity will not be related to the change in temperature. The film seems especially sensitive to damage while under high vacuum. After much trial and error we have found the power density limits are around 100mW/60μm^2 $\approx$ 35 μW/μm^2 for the pump and

$20\text{mW}/10\mu m^2 \approx 60\ \mu\text{W}/\mu m^2$ for the probe. If the pump power is too high, the signal can be unstable and will not be constant in time. If the probe power is too high, the change in reflectivity will not be linearly related to the change in temperature and the resulting data will not agree with the model. In practice, we find that 10 μm is the minimum diameter for the probe beam which permits enough power for a usable signal. Note that these values are approximate because they depend strongly on the quality of the film.

4.5 Other miscellaneous modifications

In the new Rosenhow Kendall lab it was found that there were fairly strong air currents blowing over the table from the ventilation system. These air currents cause the pump and probe beams to wobble slightly with respect to each other, resulting in increased noise. To remove this noise source, we surrounded the entire setup with a clear plastic curtain. This makes the air much more still over the table, and has the added benefit of reducing dust accumulation on the optical table. The present setup is shown in Fig. 4-4.

We also found reflections from various optical elements, particularly from the doubling crystal, could sometimes be reflected back into the laser and destabilize the cavity. To prevent this, we placed the optical isolator directly in front of the output of the oscillator. This significantly stabilized the laser and reduced laser intensity noise.

4.6 Conclusion

In this chapter we have described our pump-probe experiment and the recent modifications which have made it more robust, stable, and automated. We also showed that the system possesses the time and spatial resolution necessary to measure thermal properties at scales comparable to phonon MFPs. In the next chapter, we introduce a novel technique to experimentally measure MFPs using our pump-probe setup.

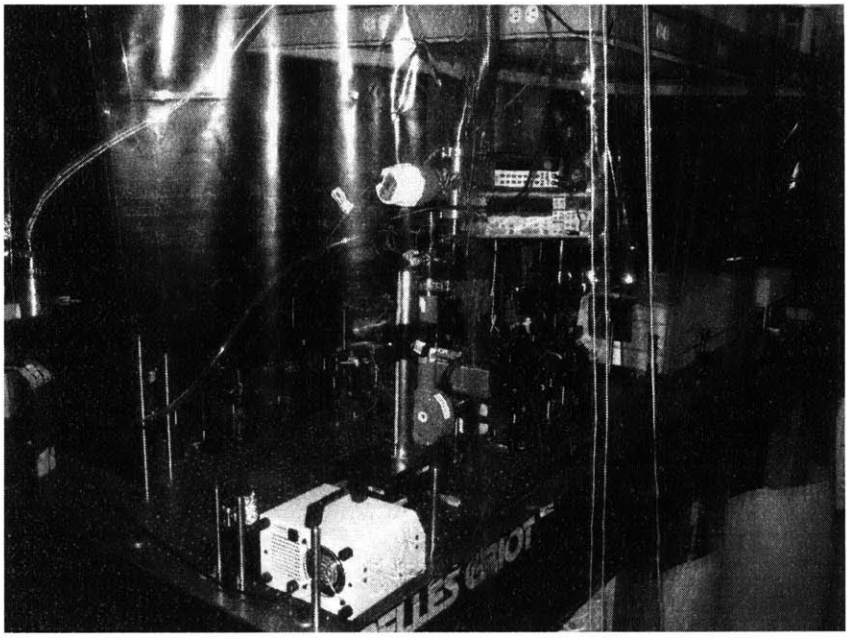

Figure 4-4: Picture of the curtains used to enclose the experiment and reduce air currents and dust accumulation.

Chapter 5

Measuring mean free paths using thermal conductivity spectroscopy

5.1 Introduction

In the previous two chapters we showed that studying transport at the length and time scales of phonons can reveal important information about the underlying phonon distribution, and that ultrafast pump-probe techniques are capable of the length and time resolution required to observe these effects. In this chapter, we introduce a novel thermal conductivity spectroscopy technique which is able to measure phonon MFPs as a distribution like that plotted in Fig. 3-1 using our pump-probe experiment.

As mentioned in earlier chapters, despite the crucial importance of the knowledge of phonon MFPs to understanding and engineering size effects, MFPs are largely unknown for even bulk materials and few experimental techniques exist to measure them. Traditionally, empirical expressions and simple relaxation time models have been the only means to estimate MFPs.[42] Recent first-principles calculations in materials such as silicon show that MFPs of phonons relevant to thermal conductivity vary by more than five orders of magnitude over the Brillouin zone.[86,91] Experimentally, inelastic neutron scattering has been used to measure phonon lifetimes in certain materials, but its resolution is limited and it is not readily accessible.[99] A time-resolved x-ray diffraction and time-domain thermoreflectance technique can measure ballistic

transport in some structures, and was used to study transport in GaAs.[100] Koh et al. observed a modulation frequency dependence of the thermal conductivity in a transient thermoreflectance experiment, which can lead to some knowledge of the phonon MFP distribution, but this technique is limited by the modulation frequency.[94]

In this chapter, we introduce a thermal conductivity spectroscopy technique which can measure MFP distributions over a wide range of length scales and materials using observations of quasi-ballistic heat transfer. The technique is based on the prediction that the heat flux from a heat source will be lower than that predicted by Fourier's law when some phonon MFPs are longer than the heater dimensions due to nonlocal heat conduction external to the heat source.[8] Our numerical solution of the Boltzmann transport equation from Chapter 3 also showed this effect; the prediction was recently confirmed experimentally in a transient grating experiment which measured the heat transfer from nickel nanolines on a sapphire substrate using a soft x-ray probe.[93] The authors observed higher thermal resistance than predicted by Fourier's law between the nickel and sapphire substrate and attributed this observation to an additional "ballistic resistance" due to ballistic transport external to the nickel nanolines. The total thermal resistance was composed of contributions from both the nickel-sapphire interface and the sapphire substrate. While this experiment measures the total thermal resistance, yielding an average MFP, our technique can distinguish the separate interfacial and substrate resistances, enabling us to extract the thermal conductivity contributions from phonons with different MFPs in the substrate. As mentioned earlier, considering the frequency dependence of the MFPs is essential because MFPs vary over such a broad length range. In addition, our approach is based on a standard pump-probe thermoreflectance technique, simplifying the experiment and modeling.

To see how the thermal conductivity spectroscopy technique works, let us examine the transport of phonons in a transient thermoreflectance (TTR) experiment. A sample usually consists of a metal film on top of a substrate which we assume is a dielectric. At $t = 0$ the metal film is impulsively heated by an ultrafast laser pulse of $1/e^2$ diameter D, called the pump pulse. Phonons emitted by electrons diffuse through the film and travel to the interface, where they are transmitted or reflected;

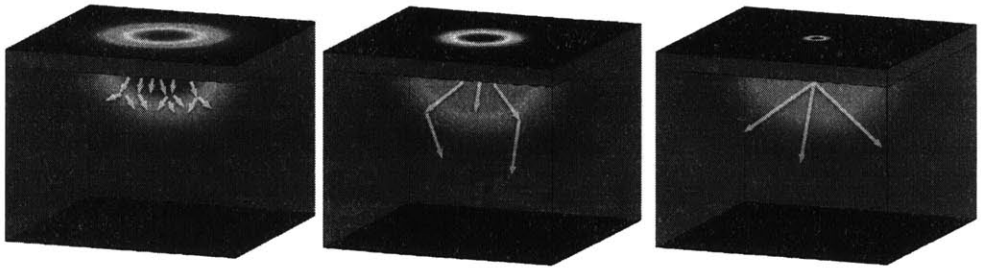

Figure 5-1: Illustration of the change from the diffusive transport regime (left), where the heater size D is much larger than MFPs, to the ballistic regime (right), where the heater size is much smaller than MFPs and a local thermal equilibrium does not exist. The thermal conductivity spectroscopy technique measures the change in thermal resistance as a function of heater size to determine the contributions of different phonon MFPs to the thermal conductivity.

the transmitted phonons then travel through the substrate.

We are concerned with heat transport in the substrate. As the transmitted phonons travel through the substrate, their probability of scattering depends on the value of the phonon MFPs Λ_ω relative to D, where ω is the phonon frequency. If $D \gg \Lambda_\omega$, the transmitted phonons scatter sufficiently to relax to a local thermal equilibrium, allowing the use of Fourier's law. Alternatively, if $D \ll \Lambda_\omega$, phonons will not scatter near the heated region and the transport will be ballistic. It has been shown that in this regime, the actual heat flux is lower than the Fourier's law prediction, which assumes the occurrence of scattering events which are now not taking place.[8,93] This reduction in heat flux is the origin of the ballistic resistance which is observed experimentally.[93] In real materials, the strong frequency dependence of phonon MFPs Λ_ω means that for any value of D comparable to MFPs, the transport will be quasi-ballistic: some phonons will be in the diffusive regime, others in the ballistic regime, and intermediate MFP phonons somewhere in between. The magnitude of the ballistic thermal resistance will depend on the particular value of D relative to the MFPs.

The above discussion shows that a measurement of heat transfer in the quasi-ballistic regime contains information about phonon MFPs. To see why, let us start with the case $D \gg \Lambda_\omega$ and decrease D. For the case of large D, the heat transfer

is diffusive and described by Fourier's law. As D decreases, the ballistic thermal resistance will appear when some phonons have $\Lambda_\omega > D$, with the magnitude of the ballistic resistance depending on the importance of a particular group of phonons to the heat transfer. For example, if the ballistic resistance grows significantly as D decreases from 60 μm to 30 μm, we can conclude that phonons with MFPs 30 $\mu m < \Lambda_\omega < 60$ μm carry a significant portion of the heat. Our thermal conductivity spectroscopy technique consists of systematically varying D and observing the change in ballistic resistance from one value of D to the next, as illustrated in Fig. 5-1. By doing so, we can infer the contribution of different phonon MFPs to the thermal conductivity based on the change in ballistic resistance. The technique is similar to point contact spectroscopy for electrons in which electron transport becomes ballistic when the contact diameter is comparable to the electron MFP.[101]

5.2 Experiment

We experimentally demonstrate this technique using transient thermoreflectance (TTR) because TTR routinely achieves micron spatial resolution and picosecond time resolution, comparable to phonon MFPs and relaxation times in many materials. We study c-Si at $T < 300$ K, because at these temperatures many phonon MFPs are hundreds of microns or larger, making the pump beam waist D between $10 - 60$ μm much smaller than a significant fraction of the phonon MFPs.

We performed a standard TTR experiment on a high-purity ($> 20,000$ Ωm) natural Si wafer coated with 100 nm of Al using electron-beam evaporation. The wafer was cleaned using a piranha solution and the native oxide removed using an HF etch immediately prior to deposition, giving a high interface conductance $G = 3.5 \times 10^8$ W/m^{2}K at $T = 300$ K. The thickness of the film was verified using profilometry. Our experimental setup has been described elsewhere.[95] To obtain quantitative information from TTR it is necessary to fit the experimental data using a thermal model. We use a two-dimensional model based on the heat equation,[95] from which we can obtain the interface conductance G between Al and Si and the thermal conductivity

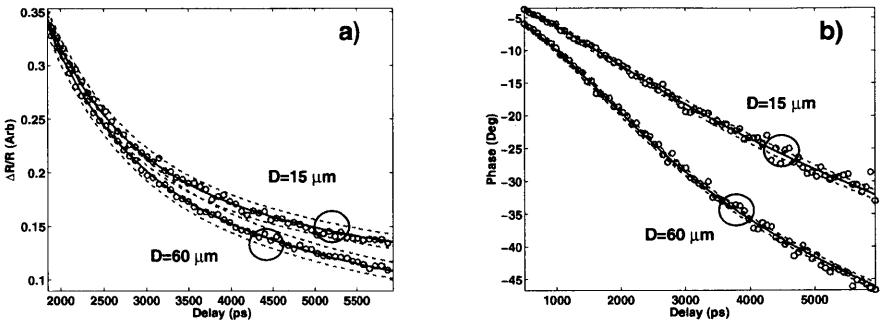

Figure 5-2: Experimental data (symbols) at T = 90 K for pump beam diameters $D = 60\ \mu m$ and $D = 15\ \mu m$, along with the best fit to the a) amplitude and b) phase data from a thermal model (solid lines). To show the sensitivity of the fit, the model prediction for the best fit thermal conductivity values plus and minus 10% are shown as dashed lines. The thermal conductivities obtained from the fits are 630 and 480 W/mK, respectively, different from each other and both far from the accepted thermal conductivity of 1000 W/mK.[102]

k of Si. When the heat transfer is diffusive, this fitting procedure returns accurate thermal properties for a variety of materials.[95] However, for quasi-ballistic transport the experiment will measure an additional ballistic resistance, the magnitude of which depends on the number of modes with MFPs longer than the pump beam diameter.

Figures 5-2(a) and 5-2(b) show representative experimental amplitude and phase signals ($R^2 = X^2 + Y^2$; $\Phi = \tan^{-1}(Y/X)$; where X and Y are the in-phase and out-of-phase signals returned from the lock-in amplifier, respectively), and the fitting curves which are used to extract the thermal conductivity.[95] The data in this figure were taken at T=90 K for pump beam diameters $D = 60\ \mu m$ and $D = 15\ \mu m$. The fits are quite good, but correspond to thermal conductivities of 630 W/mK and 480 W/mK, respectively, different from each other and both far from the accepted thermal conductivity of 1000 W/mK at 90 K.[102] This indicates that the heat transfer in the substrate is significantly smaller than that predicted by Fourier's law.

Figure 5-3(a) shows our TTR measurements of the thermal conductivity of Si versus temperature, along with literature values of the thermal conductivity[102] and modeling results which will be explained later in the chapter. The symbols and error bars represent the average and standard deviation, respectively, of measurements

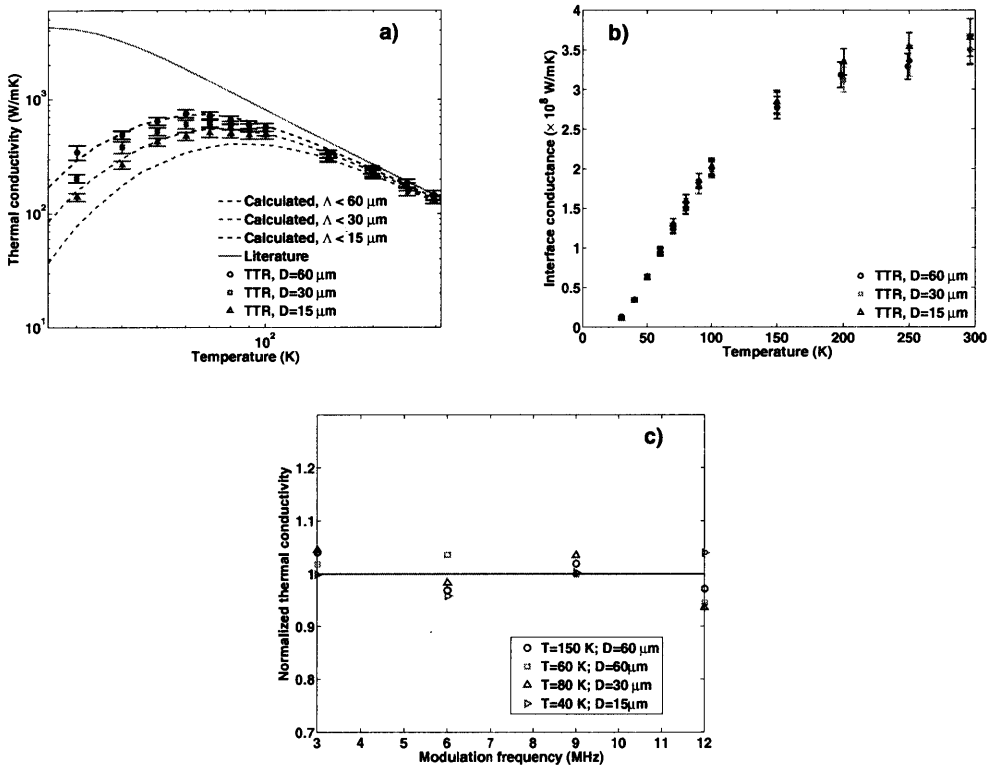

Figure 5-3: (a) Experimental (symbols), calculated by only including the contributions of the indicated MFP or smaller (dashed lines), and the literature (solid line) thermal conductivity of pure c-Si.[102] (b) Measured interface conductance of the Al/Si interface. It is seen that the interface conductance does not depend on beam diameter. (c) Representative measurements of the normalized thermal conductivity versus pump beam modulation frequency for several temperatures and beam diameters. No frequency dependence of the thermal conductivity is observed.

taken at different locations on different samples, prepared at different times, at four different modulation frequencies from 3-12 MHz. Three different pump $1/e^2$ diameters of 60 μm, 30 μm, and 15 μm were used with a constant probe beam diameter of 11 μm. The ellipticities e of the pump and probe beams were $0.8 < e < 1$. The pump beam power was adjusted so that the intensity remained the same for each diameter; the probe power remained constant. Care was taken to ensure that the steady-state and transient temperature rise of the sample did not exceed 2 K. The lateral spreading of heat in the Al film is estimated to be less than 1 μm in the temperature range of the experiment. All measurements were taken under high vacuum (1×10^{-5} torr). The temperature of the sample was monitored using a silicon diode placed next to the sample. At room temperature, where MFPs are shorter, our measurements are independent of diameter and in good agreement with literature values, but our measurements begin to diverge from the literature values below around 200 K and a diameter dependence of the thermal conductivity appears. This discrepancy is because the ballistic thermal resistance measured by the experiment increases as temperature decreases due to the rapid increase in MFPs. A smaller thermal conductivity is measured for smaller pump beam diameters because the ballistic resistance is larger around a smaller heated region.

The thermal interface conductance values between Al and Si measured using different laser beam diameters are shown in Fig. 5-3(b), and no diameter dependence is observed, indicating that ballistic transport in the silicon substrate is responsible for the observed results. In the transient grating experiments in Ref. 93, the total thermal resistance from the interface and substrate was measured, making it difficult to study transport specifically in the substrate.

Koh et al. observed a laser modulation frequency dependence of the measured thermal conductivity of semiconductor alloys in a pump-probe experiment and interpreted the result by assuming that some phonons are ballistic over the cross-plane thermal diffusion length.[94] We did not observe a strong frequency dependence as shown in Fig. 5-3(c), suggesting that the change in radial heat transfer is the dominant effect rather than a one-dimensional thermal penetration effect. The authors of

Ref. 94 also did not observe a frequency dependence of the thermal conductivity in Si at room temperature.

5.3 Discussion

To further understand our measurements, we need to examine how ballistic modes affect the heat flux. In principle the transport in the quasi-ballistic regime can be calculated using the Boltzmann transport equation (BTE).[81] However, solving the BTE is difficult because the distribution function is a function of 5 variables under the isotropic crystal approximation, and a large spatial domain comparable to D is required. More importantly, the solution requires the MFPs, which are generally unknown, to be specified. We would like to measure spectrally resolved properties without any *a priori* assumptions concerning the relaxation times or MFPs.

Therefore, rather than solving the BTE, we make the following approximation which still yields useful results. We divide the phonons in the substrate into two groups, a diffusive group and a ballistic group. The diffusive group has short MFPs $\Lambda_\omega < D$ so that a local thermal equilibrium exists among these modes and diffusion theory is valid. The ballistic group, however, has MFPs $\Lambda_\omega > D$ which are assumed to be effectively infinite. If we examine the BTE,[81] we find that this assumption completely decouples the ballistic group from the rest of the phonons; individual phonon modes in the ballistic group propagate independently of the diffusive group and of each other. As shown earlier, while these ballistic modes still carry heat, due to their ballistic resistance, they carry significantly less heat than is predicted by Fourier's law. Meanwhile, the diffusive group is transporting heat according to Fourier's law. Under this approximation, then, the thermal conductivity measured in the experiment is the thermal conductivity of the diffusive group with MFP $\Lambda_\omega < D$; the ballistic group does not contribute to thermal transport due to the effectively infinite ballistic resistance.[94]

To verify this model we can calculate the expected thermal conductivity if the ballistic group, with $\Lambda_\omega > D$, does not contribute to the measured thermal con-

ductivity. Because there are many different suggested relaxation times for Si in the literature, we compute the phonon MFPs in Si from first principles, following a similar procedure as described in Ref. 86. Briefly, density functional theory is employed to compute the potential energy derivative in Si crystals. Perturbation to the atomic positions is used to extract the third and fourth order anharmonic coefficients of the potentials, and Fermi's golden rule is used to compute relaxation times, while other quantities such as the dispersion and group velocity are computed from the harmonic force constants.[103] Using the computed information, the thermal conductivity can be determined from $k = \sum_q C_q v_{x,q}^2 \tau_q$, where q is the phonon wavevector. The ballistic group can be excluded by removing terms from the sum according to the MFP of the mode. The results of the calculation are shown as the dashed lines in Fig. 5-3(a). The agreement between our measurements and this simple cutoff model is reasonably good. Obtaining quantitative agreement is difficult because at these low temperatures the thermal conductivity is highly sensitive to the isotope concentration, which is not known exactly for our sample. We take a typical isotope concentration value for natural silicon specified in chapter 3; the calculation using this value matches our experimental results reasonably well.

We can now use our measurements to determine the thermal conductivity distribution of silicon as a function of MFP.[104] In our experiment, we have measured the thermal conductivity of the diffusive group of phonons with MFPs shorter than the pump beam diameter. Thus, normalizing the measured thermal conductivities by the true thermal conductivity of Si will give the fraction of the thermal conductivity contributed by phonons with $\Lambda_\omega < D$, which is simply the thermal conductivity accumulation distribution. Our experimental measurements of this distribution, along with that predicted by the first-principles calculations, are shown in Fig. 5-4. The agreement between the experiment and the calculation is again reasonably good. Note that no assumption about the MFPs was used in the analysis of the experimental data: the data were analyzed using the heat equation to determine the apparent thermal conductivity, and this value was compared to the results of the first-principles calculations. The consistency between these two approaches is encouraging, and indicates

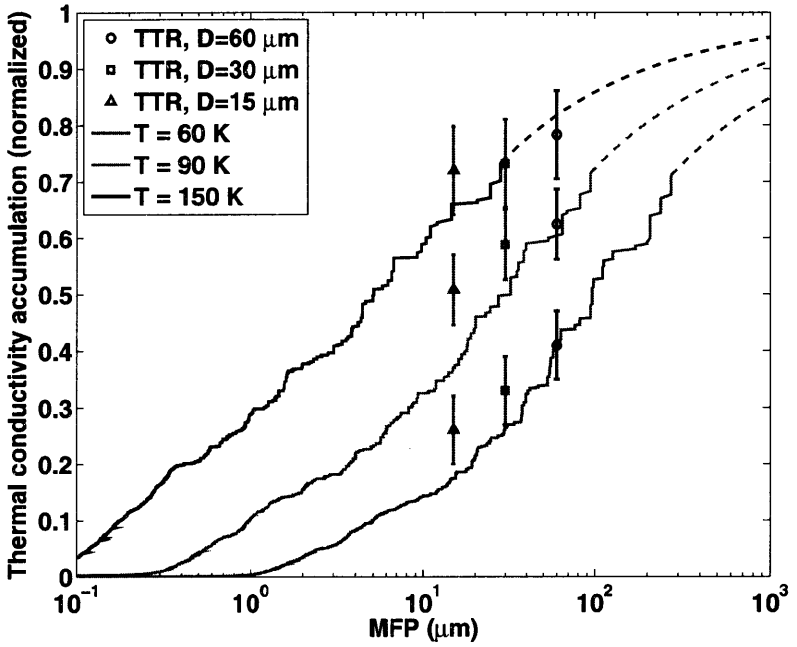

Figure 5-4: Experimental measurements (symbols) and first-principles calculations (lines) of the thermal conductivity accumulation distribution of silicon versus MFP. The symbols and error bars represent the average and standard deviation, respectively, of measurements taken at different locations on different samples, prepared at different times, at four different modulation frequencies from 3-12 MHz. Because of the finite number of reciprocal space points included in the first-principles calculations, the calculated distribution of MFPs is discrete and cannot include some long wavelength (and hence long MFP) modes. We use an extrapolation (dashed lines) to estimate the contribution from these long wavelength modes.

that our technique is accurately measuring the thermal conductivity contributions from different phonon MFPs.

5.4 Conclusion

In summary, we have demonstrated the first experimental technique which can measure the MFPs of phonons relevant to thermal conduction across a wide range of length scales and materials. While empirical expressions and simple relaxation time models have traditionally been the only means to estimate MFPs, our technique enables a direct measurement of how heat is distributed among phonon modes. Although our demonstration of the thermal conductivity spectroscopy technique is based on low temperature experiments where a considerable fraction of the phonons have MFPs longer than tens of microns, the technique can be extended to a much wider length range by creating smaller heat sources. There are many ways to achieve smaller heat sources such as tight focusing of laser beams, transient grating experiments, and lithographically patterned heaters or light absorbers. Considering the crucial importance of the knowledge of MFPs to understanding and engineering size effects, we expect the technique to be useful for a variety of energy applications, particularly for thermoelectrics, as well as for gaining a fundamental understanding of nanoscale heat transport. For example, determining how much heat is carried by which MFPs will allow the design of structures which can most effectively scatter these modes, reducing the thermal conductivity of the material. For thermoelectrics, this would directly translate to an increase in energy conversion efficiency, assuming the electrical properties are minimally affected.

Chapter 6

Measuring mean free paths at the nanoscale

6.1 Introduction

In the last chapter we introduced a thermal conductivity spectroscopy technique which is able to measure phonon MFPs and their contribution to thermal conduction, and we demonstrated the technique by measuring the MFP distribution of silicon at cryogenic temperatures. The technique was successful in this demonstration because phonon MFPs in silicon are hundreds of microns or longer at these low temperatures, much longer than the pump beam diameters of tens of microns. The natural next step is to measure MFPs using the technique in materials of technological relevance, like thermoelectric materials at room temperature. Unfortunately, applying the technique requires creating a heated region of size comparable to the MFPs of the heat-carrying phonons, which are in the tens to hundreds of *nanometers* for many materials. This small length scale is not accessible optically due to diffraction; the minimum beam waist that can be typically achieved is approximately one micron. As discussed in chapter 4, the practical minimum size for the pump and probe beams is much larger, approximately 10 μm, due to restrictions on power density in the film. We therefore have a problem if we wish to probe phonon transport at the nanoscale using this technique.

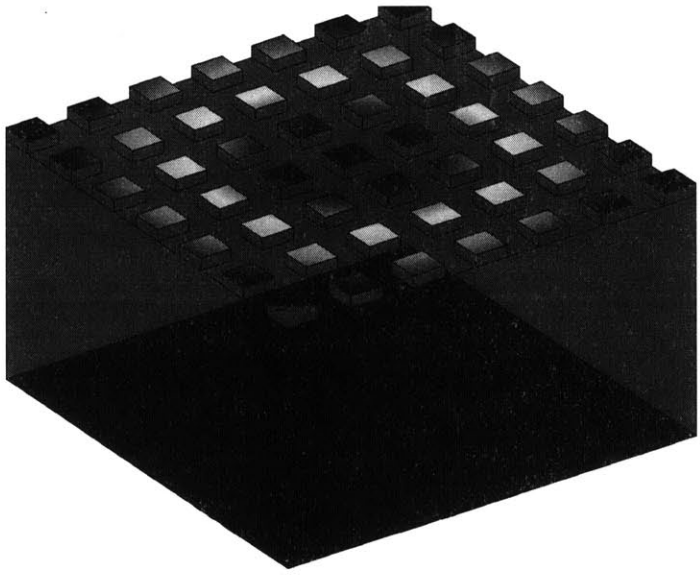

Figure 6-1: Schematic of the metallic nanodot array on a substrate illuminated by a much larger optical heating beam. Because the effective length scale for heat transfer is the dot diameter rather than the optical beam diameter, heat transfer at the nanoscale can be observed, beating the diffraction limit.

In this chapter, we introduce a modification of thermal conductivity spectroscopy which allows us to access these length scales. Rather than heating a continuous metal film, in this modified technique we instead lithographically pattern metallic nanodot arrays on the sample using electron beam lithography (EBL), as shown in Fig. 6-1. Then, we use the pump beam to illuminate the entire dot array and the probe to measure the heat transfer from the dots. In this way, the effective length scale for heat transfer is the dot diameter rather than the optical beam diameters. Because EBL is capable of spatial resolution down to tens of nanometers, we are able to probe heat transfer at length scales far below what is possible optically. Here we study phonon transport in sapphire as this material is transparent to visible light. A similar technique was demonstrated in Ref. [93], where soft x-ray light was used to observe quasi-ballistic transport from thin Ni lines patterned on a sapphire substrate. In this work, we show we can observe quasi-ballistic transport simply by using transient

thermoreflectance (TTR), and use our observations to extract the MFP distribution.

This chapter is organized as follows. First, we introduce the model used to calculate the heat transfer from the dots. Next, we discuss the details of our experiment and the fabrication of the dot arrays. We then present our measurements of the MFP distribution, and discuss the possibilities for future work.

6.2 Heat Transfer Model

6.2.1 Introduction

The heat transfer analysis used for our experiment has been described in detail in Ref. [95] and will be briefly reviewed here. The solution of the heat equation which accounts for radial heat transfer, Gaussian beams, and the high repetition rate of our laser is given in terms of the transfer function Z:[95]

$$Z(t) = \sum_{m=-\infty}^{\infty} H\left(\omega_0 + m\omega_s\right) e^{jm\omega_s t} \tag{6.1}$$

The real and imaginary parts of Z correspond to the in-phase and out-of-phase signal return by the lock-in amplifier, respectively.[95] Here ω_0 is the angular modulation frequency, typically between 1 and 15 MHz; $\omega_s = 80\text{MHz}$ is the angular laser repetition frequency; $j = \sqrt{-1}$, and $H(\omega)$ is the solution of the heat equation.

The solution $H(\omega)$ can be written as the product of the transfer matrices for the layers.[105] The properties at the bottom of a layer can be related to the properties at the top of a layer using a transfer matrix given by:

$$\begin{bmatrix} \theta_b \\ f_b \end{bmatrix} = \begin{bmatrix} \cosh(qd) & \frac{-1}{\sigma_z q}\sinh(qd) \\ -\sigma_z q \sinh(qd) & \cosh(qd) \end{bmatrix} \begin{bmatrix} \theta_t \\ f_t \end{bmatrix} \tag{6.2}$$

where θ is the temperature, f is the heat flux, subscript b and t denote the bottom and top of the layer, respectively, d is the layer thickness, σ_z the cross-plane thermal conductivity, and $q^2 = j\omega/\alpha$, where α is the thermal diffusivity. Multiple layers can

be conveniently treated simply by multiplying the matrices together:

$$\begin{bmatrix} \theta_b \\ f_t \end{bmatrix} = \mathbf{M}_n\mathbf{M}_{n-1}...\mathbf{M}_1 = \begin{bmatrix} A & B \\ C & D \end{bmatrix} \begin{bmatrix} \theta_t \\ f_t \end{bmatrix} \tag{6.3}$$

$\mathbf{M}_i$ is the transfer matrix for layer i. If the bottom layer is semi-infinite or adiabatic, which is usually the case, then the surface temperature at the top of the layers, θ_t, is given in the terms of the heat flux boundary condition f_t as:

$$\theta_t = \frac{-D}{C} f_t \tag{6.4}$$

To account for radial conduction, a zero-order Hankel transform is applied to the heat equation in cylindrical coordinates. It has been shown that the results above apply in this case with only a modification to the definition of q, which now becomes:[95]

$$q^2 = \frac{\sigma_r k^2 + C_v j\omega}{\sigma_z} \tag{6.5}$$

where σ_r is the in-plane thermal conductivity, C_v is the volumetric specific heat, and k is the Hankel transform variable. The heat transfer boundary condition f_t is now a Gaussian function of the radial coordinate r, following the intensity distribution of the pump beam of radius w_0. Weighting this result with the Gaussian intensity distribution of the probe with radius w_1 gives the final solution to the heat equation $H(\omega)$:[95]

$$H(\omega) = \int_0^\infty k \left(\frac{-D}{C}\right) \exp\left(\frac{-k^2(w_0^2 + w_1^2)}{8}\right) dk \tag{6.6}$$

Because the final solution is normalized to facilitate fitting with experimental data, the constants have been omitted from the above equation. This is the model which is used for a typical pump-probe experiment.[95]

6.2.2 Single Dot Heat Transfer Model

The previous analysis models the heat transfer through continuous layers with a Gaussian heating and probing profile. This analysis must be modified to account for

the discontinuous nature of the dot array. We first assume that the heat transfer from a particular dot is independent from the other dots, making the modification is particularly simple. Since the dot radius a is much smaller than the pump and probe radii, both the heating and probing profile can be well described by a radial step function of radius a. The zero-order Hankel transform of a step function is $J_1(ak)/k$,[106] where $J_1(z)$ is a first-order Bessel function of the first kind, and so replacing the exponentials in Eq. 6.6 with this function gives $H(\omega)$ for a circular dot:

$$H(\omega) = \int_0^\infty \frac{1}{k}\left(\frac{-D}{C}\right) J_1^2(ak)dk \tag{6.7}$$

If the dot were square rather than circular, we would obtain a similar mathematical expression but with a two-dimensional integration over a $\mathrm{sinc}(x) \times \mathrm{sinc}(y)$ function.

6.2.3 Dot Array Heat Transfer Model

If the dots are sufficiently close together that the heat transfer from a particular dot is affected by the presence of other dots, then it is necessary to solve for the heat transfer from the entire dot array. Fortunately, the dot array can be incorporated into the transfer matrix method fairly easily. To account for the discontinuous nature of the dots, we model the metal film as a special layer in which the thermal conductivity in the r direction, σ_r, is zero. Then, we apply a heating profile that has the shape of the dot array. In this way, the special film is only heated at the location of the dots, and, because $\sigma_r = 0$, the heat can only diffuse in the z direction. Thus there will be no heat transfer between the heated regions, corresponding precisely to the actual physical system.

The next step is to determine the appropriate heating profile. A square array of circles is difficult to Fourier transform analytically, but a square array of squares, or a two-dimensional square wave, can be represented exactly as a Fourier series. Therefore, we model the heating profile as a two-dimensional square wave with each square having a side length of $w = 2a$ and a period L. It is now more appropriate to solve the heat equation in Cartesian rather than cylindrical coordinates, and so the

definition of q becomes:

$$q^2 = \frac{\sigma_{xy}(k_x^2 + k_y^2) + C_v j\omega}{\sigma_z} \tag{6.8}$$

where σ_{xy} is the in-plane thermal conductivity, and k_x and k_y are the spatial Fourier transform variables in x and y, respectively.

To obtain $H(\omega)$ we can perform the procedure as before; compute the transfer matrices for different values of k_x and k_y, compute the Fourier transform of the heating function f_t, obtain $\theta_t = (-D/C)f_t$, and weight this by the probe function to get $H(\omega)$. Since the square wave heating function is periodic, its Fourier transform consists of discrete multiples of the fundamental spatial frequency $\Omega_0 = 2\pi/L$:

$$f_t(\Omega) = Q \sum_n \sum_m X_{nm} \delta(\Omega - n\Omega_0)\delta(\Omega - m\Omega_0) \tag{6.9}$$

where Q is the energy of the pump beam, Ω is a continuous spatial frequency variable, and X_{nm} are the Fourier components of the square wave, given by:

$$X_{nm} = \begin{cases} w^2/L^2 & n = m = 0 \\ \frac{w/L}{2\pi mj}(1 - \exp(-jm\Omega_0)) & n = 0, m \neq 0 \\ \frac{w/L}{2\pi nj}(1 - \exp(-jn\Omega_0)) & n \neq 0, m = 0 \\ \frac{-(1-\exp(-jm\Omega_0)(1-\exp(-jn\Omega_0)}{4\pi^2 nm} & n \neq m \neq 0 \end{cases} \tag{6.10}$$

Because f_t only contains discrete multiples of Ω_0, $\theta_t = -(D/C)f_t$ only contains these frequencies. It can be shown that weighting θ_t by the same probe profile results in the simple expression for $H(\omega)$:

$$H(\omega) = \sum_n \sum_m |X_{nm}|^2 \left(\frac{-D}{C}\right)_{n,m} \tag{6.11}$$

where the subscripts n and m correspond to evaluating the argument at frequencies $k_x = n\Omega_0$ and $k_y = m\Omega_0$, respectively.

Note that this procedure has neglected the Gaussian intensity variation of the pump and probe beams. To account for this, it is necessary to modify the heating and probing profile by multiplying the square wave by a Gaussian. In the Fourier domain,

the multiplication becomes convolution, and the result is essentially a Dirac comb of Gaussians at each discrete frequency point. The resulting Fourier transform is now a continuous function of frequency because the Gaussian is aperiodic, significantly complicating the analysis.

An approximation can be made if the squares are much smaller than the pump and probe radii. Intuitively, if the pump and probe radii w_0 and w_1 are much larger than the array period L then it is reasonable to approximate the pump and probe radii as infinitely large and with uniform intensity. In the frequency domain, this can be explained because of the mismatch in spatial frequencies. An array with a small period L, relative to w_0 and w_1, will have a high spatial freqency $\Omega_0 = 2\pi/L$. The frequency components in the Gaussian are distributed as $\exp(-w_i^2\Omega^2/8)$, where i=1 or 2 corresponds to the pump or probe radius. Thus if $(w_i/L)^2 \gg 1$, the frequency components of the Gaussian will be confined to a region in frequency space close to the discrete frequency of the square wave. In this case we can simply approximate the function as a delta function and recover the simpler result given in Eq. 6.11. Because the condition for this approximation to hold scales as $(w_i/L)^2$, the approximation is expected to be accurate even for periods approaching the probe radius w_1. As described in the next section, the probe radius is around 5 μm, and we are typically concerned with $L < 2$ μm, and so the approximation is expected to be valid.

Finally, we note that in the previous two sections, we assumed a different shape for each heat transfer model, a circle and a square, due to mathematical convenience for each model. While it is possible that the shape of the nanodot could affect the heat transfer, experimentally we find the heat transfer is a strong function only of the dot size, not the shape.

6.3 Sample Design and Fabrication

The metal nanostructures are fabricated using a standard metal lift-off process. Before discussing the fabrication details we quickly discuss the design of the dot arrays which we found necessary to obtain usable data. Ideally, we would like to make

the dot diameters as small as possible so that we can study heat transfer at the smallest length scales. This requires a dot thickness smaller than the dot diameter so that the dot aspect ratio is not too large and the dots can adhere to the substrate. Motivated by this goal, we initially tried fabricating dots with thicknesses around 20-30 nm but encountered several challenges. First, when the metal layer is so thin the thermal conductivity extracted from the model is extremely sensitive to the metal layer thickness. A difference of only 2-3 nanometers in the dot thickness can change the fitted thermal conductivity value by up to 30 %. Furthermore, because electron-beam evaporation is an inherently random process, spatial variations in the deposition rate and roughness in the film can easily lead to a difference in thickness between dots on the order of a 2-3 nanometers. These two issues make obtaining reliable, quantitative data from thin dots difficult.

Thin dots present another problem. The rate at which the dots cool is linearly related to their volumetric specific heat. If we perform a simple lumped capacitance analysis, we find the time constant for the temperature decay is $\tau = Ct/G$, where C is the volumetric specific heat, t is the thickness of the dot, and G is the interface conductance. If the dots are thin, their temperature, and hence the thermoreflectance signal, quickly decays to a level that is at the noise floor of our experiment. Thus after a certain delay time, we are only able to measure noise rather than the desired signal, making it impossible to extract the thermal conductivity. Increasing the thickness to 70-80 nm increases the thermal time constant and makes the measurement possible.

From these considerations, we focused on obtaining reliable, quantitative results from dots with thicknesses of approximately 70-80 nm and diameters larger than 100 nm. The sample fabrication procedure is as follows. The substrate is a 12.5 mm square, single side polished, single crystalline c-plane sapphire wafer (MTI corporation). Sapphire is chosen because it is transparent to visible radiation and has MFPs in the hundreds of nanometers.[93] The sapphire wafer is rinsed with DI water, then spin-coated at 1000 RPM with 950K PMMA resist (950K A2 from Microchem, A4 can also be used to give a thicker resist layer), giving a resist layer approximately 150 nm thick. The resist layer should be at least twice the desired metal thickness,

but not too thick as this decreases the resolution of the lithography process. Because sapphire is electrically insulating, it is necessary to deposit a 5-10 nm Ti conduction layer for the electron-beam lithography (EBL) process. The dot array is designed using the CleWin4 layout software. The resist is exposed using EBL at 10 kV, permitting feature sizes down to 100 nm to be reliably written. Because the MIT EBL machine often exposes a larger area than specified in the layout, a size matrix of several slightly smaller diameter dots (typically 25-50 nm smaller than the desired diameter) is exposed for each desired diameter. Next, the titanium layer is removed using a 20:1:1 H_2O:HF:H_2O_2 solution, and then the resist is developed with a 3:1 IPA:MIBK solution. The wafer is immediately coated with a 5 nm Ti adhesion layer, followed by 60-70 nm of Al, using electron-beam evaporation. Finally, the remaining resist is removed by soaking the sample in Microstrip (N-Methyl-2-pyrrolidone) at 80 C for two hours, followed by a one minute low power sonication. The thickness of the dots is verified using profilometry.

The final result is shown in optical and SEM images in Fig. 6-2. The nanostructures consist of arrays of closely packed circles or squares of varying diameter. Because the dots are discontinuous and cannot exchange heat as they would in a metal film, the effective length scale for heat transfer is the dot diameter rather than the optical beam diameter. While ideally each dot cools independently of the others, when the separation between the dots is comparable to the thermal penetration length l_{th} the heat transfer from a particular dot will be affected by presence of the other dots. Because $l_{th} \sim \sqrt{\alpha/f_0} \sim 1\ \mu m$ in sapphire, where α is the thermal diffusivity and f_0 is the modulation frequency, it is expected that for dot separations in the hundreds of nanometers the dots will not be independent, necessitating the use of the model derived in section 6.2.3.

When the dot radius becomes comparable to the dominant phonon MFPs in sapphire the transport becomes quasi-ballistic. By observing the increase in ballistic thermal resistance as the dot radius shrinks we can measure the contribution of different phonon MFPs to the thermal conductivity, just as we did to measure the silicon MFP distribution in the previous chapter.

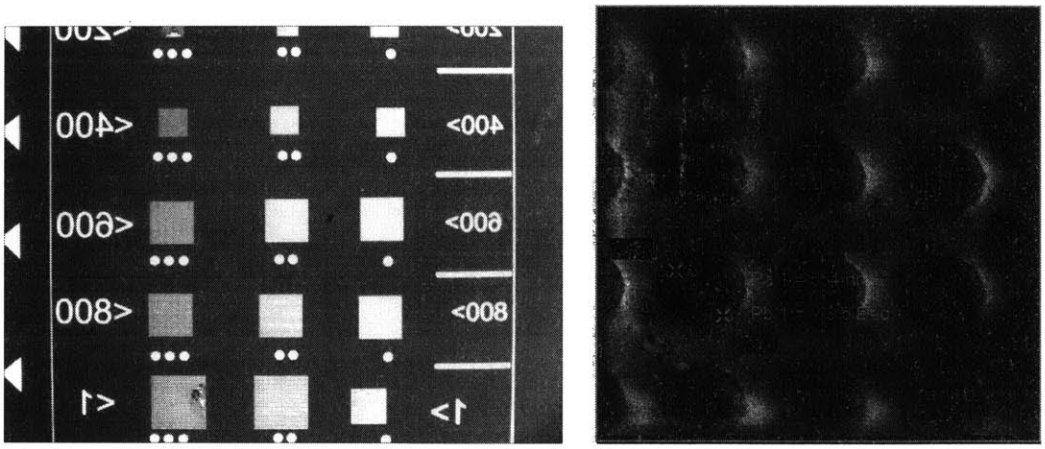

(a) Optical image at 10X magnification.

(b) SEM image at 5 kV, 4000X magnification.

Figure 6-2: Optical image and SEM image of the nanodot array fabricated by electron-beam lithography (EBL). The numbers in the optical image correspond to the diameter of the dot (800 = 800 nm, and so on). Because the MIT EBL machine often exposes a larger area than specified in the layout, a size matrix of several different diameter dots was exposed for each intended diameter; these different sizes are indicated by the number of large dots below each array.

6.4 Results

We created both circular and square individual dots with diameters from 1-10 μm, along with dot arrays containing square dots with diameters from 100 nm - 10 μm. The measurements were taken at a modulation frequency of 12 MHz to shorten the thermal penetration length and minimize the influence of other dots on a particular dot's heat transfer. In order to obtain reliable data with a sufficient signal to noise ratio (SNR), the pump and probe powers and sizes needed to be adjusted. Because the dots occupy 25% of the surface area on the sapphire, only approximately 25% of the reflected light is due to the dots and thus the signal is nominally four times smaller than it would be with a continuous film. In practice, we find that the signal is often up to ten times smaller than in the continuous film case because some probe light is diffracted and does not reach the detector. To offset this decrease, we increased the probe power, which increases the power reaching the detector but also decreases the power in the pump beam. To offset this decrease in pump power, we shrink the pump beam diameter to around 30 μm, increasing the pump beam intensity

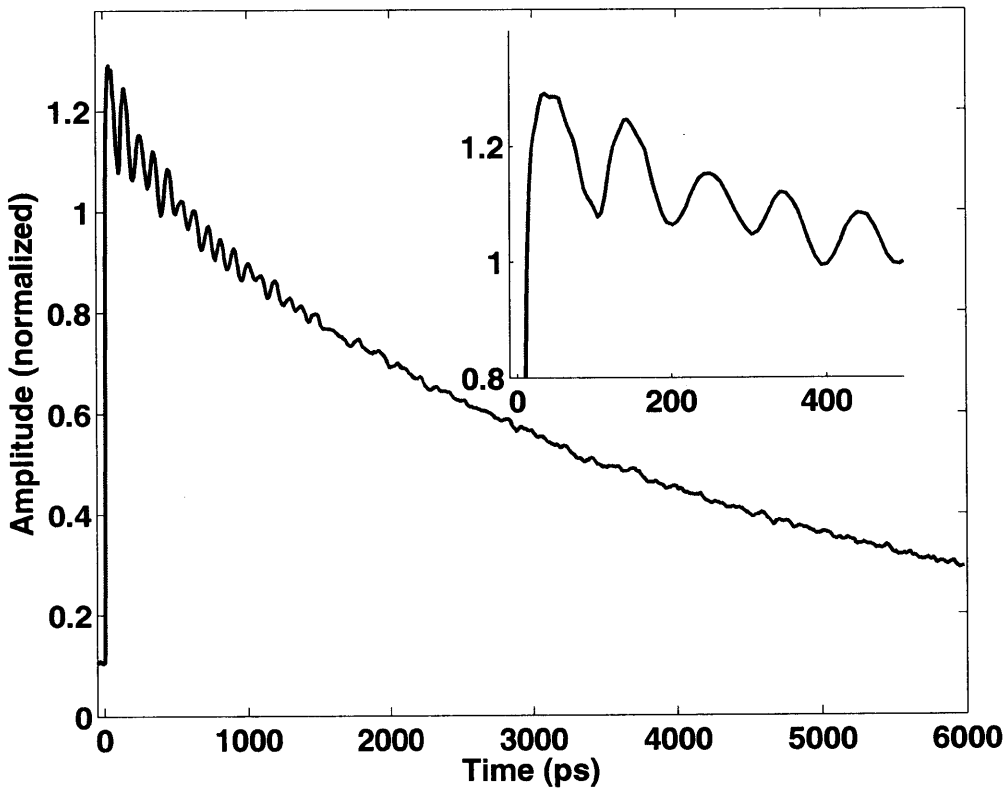

Figure 6-3: Typical amplitude experimental data for D=400 nm Al dots on a sapphire substrate. The inset shows data for shorter delay times, where oscillations in the signal are observed. The oscillations are believed to be due to a transient diffraction grating effect caused by thermal expansion and contraction of the dots.

and therefore the magnitude of the desired signal. These modifications result in a sufficiently high SNR to obtain quantitative measurements of thermal properties. Figure 6-3 shows a typical experimental data curve. The early part of the decay curve, up to approximately 2 ns, shows an interesting oscillation. Examining the period of the oscillation, we find that the period is too long to be caused by acoustic strain waves traveling through the thickness of the dots.[96] Instead, it seems likely that this oscillation is a type of transient grating effect due to thermal expansion and contraction of the dots. The dot array, as a periodic array of objects with a spacing on the order of the laser wavelength, acts as a diffraction grating for the pump and probe beams. When the pump heats up the dots, the dots thermally expand and

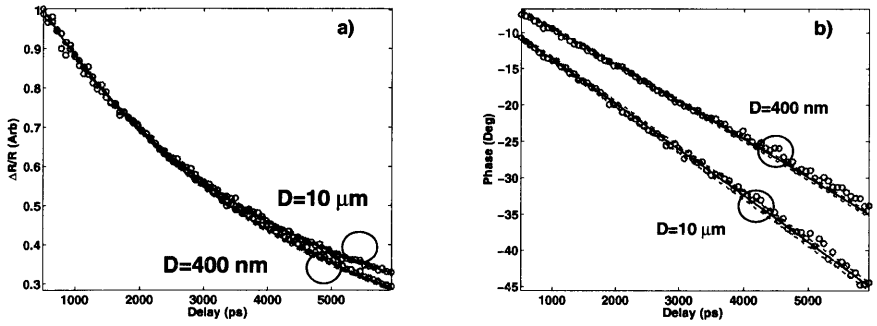

Figure 6-4: Experimental data (symbols) dot diameters $D = 10\ \mu m$ and $D = 400$ nm, along with the a) amplitude and b) phase fit to the data from a thermal model (solid lines) and 10% bounds on the fitted thermal conductivity value (dashed lines). The thermal conductivities obtained from the fits are 37 and 22 W/mK, respectively. The value for the 10 μm dots is in good agreement with the literature value for the thermal conductivity of sapphire, but the value for the 400 nm dots is lower, indicating that MFPs are in the hundreds of nm in sapphire.

subsequently contract in an oscillatory manner, resulting in a small change in the amount of probe light diffracted and thus the amount of light reaching the detector. We estimate that for a 10 K temperature rise the dots expand by only 1-5 Angstroms, a very small change which remarkably appears to produce the oscillating signal shown in Fig. 6-3. After the oscillation damps out, the monotonically decreasing signal is due to the thermal decay of the dots. It is this portion of the signal which contains information about the heat flux from the dots to the substrate and hence the thermal properties of the substrate.

Figures 6-4a and 6-4b shows the data and the model fit for 10 μm and 400 nm dots. Recall that the in-phase signal $X = Re(Z)$, out-of-phase signal $Y = Im(Z)$, amplitude $R^2 = X^2 + Y^2$, and phase $\Phi = \tan^{-1}(Y/X)$, where Z is the transfer function. The model fits both data sets quite well, but the fit for the 400 nm dots corresponds to a smaller thermal conductivity of 21 W/mK rather than the bulk value of 35 W/mK, indicating the heat transfer is in the quasi-ballistic regime for the 400 nm dots.

The measured thermal conductivity for all the diameters is shown in Fig. 6-5. At the largest length scales of 1-10 μm, the heat transport is diffusive and the dots

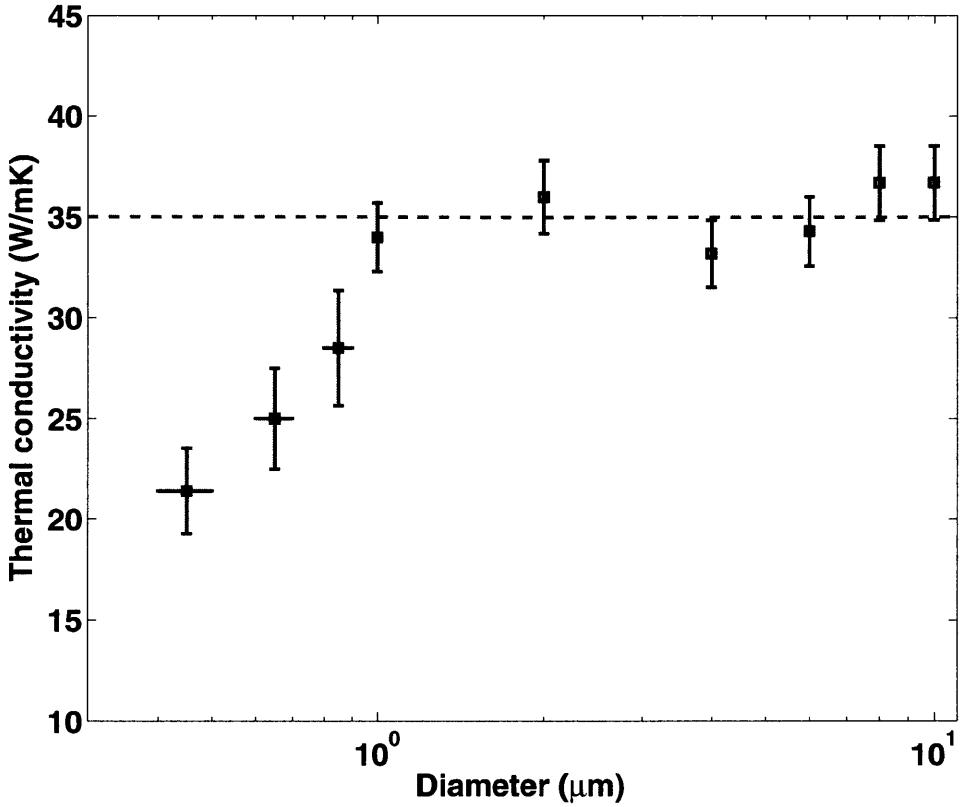

Figure 6-5: Measured thermal conductivity of sapphire versus dot diameter. The measurements indicate that the dominant heat-carrying phonons in sapphire have MFPs < 1 μm.

cool independently; both heat transfer models return the bulk thermal conductivity of sapphire, which is approximately 35 W/mK along the c-axis at room temperature. We also confirm that the shape of the dot has little effect on the heat transfer. Deviations from Fourier's law appear for dot diameters less than 1 μm, where we measure a lower thermal conductivity than the literature value. This indicates that the transport is quasi-ballistic and the experiment is measuring an additional ballistic resistance, exactly as was observed in chapter 5. Our results show that the dominant heat carrying phonons in sapphire have MFPs < 1 μm, which is consistent with previously reported results,[93] and that phonons with MFPs between approximately 400 nanometers and 1 μm contribute slightly under half to the total thermal conductivity.

6.5 Conclusion

In this chapter we have extended the technique of thermal conductivity spectroscopy to the nanoscale. By using electron-beam lithography to pattern nanodot arrays, we are able to observe quasi-ballistic heat transfer and measure the MFP distribution at length scales far below the diffraction limit. In sapphire, we have confirmed that the dominant phonon MFPs are in the hundreds of nanometers. We expect that this combination of ultrafast optical techniques with nanoscale spatial patterning will prove useful in measuring MFP distributions in technologically relevant materials like thermoelectrics, where MFPs may be in the tens or hundreds of nanometers.

Chapter 7

Summary and future directions

7.1 Summary

Nanoscale heat transfer is a fascinating and rapidly growing field which could make substantial contributions to addressing one of our present energy challenges. In particular, nanostructured thermoelectric materials could allow some of the enormous amount of wasted heat to be recovered as electricity, improving the overall efficiency of our energy conversion systems. Despite recent improvements in the figure of merit of nanostructured thermoelectrics, much remains unknown concerning the precise mechanisms by which the heat carriers in thermoelectric materials, electrons and phonons, are affected by nanostructures. This thesis has explored the physics of nanoscale transport in these materials and helped identify how we can use nanoscale effects to engineer more efficient thermoelectric devices. Using a combination of modeling and experiment we were able to better understand electron and phonon transport in nanostructured thermoelectrics, and we introduced a new experimental technique to help us understand fundamental phonon transport in all types of materials.

Chapter 2 studied electron and phonon transport in nanocomposite thermoelectric materials using a newly developed grain boundary scattering model and materials characterization. Using the model we are able to explain how the thermoelectric properties are affected in nanocomposites as well as to identify strategies which could lead to more efficient materials.

The rest of the thesis focused on understanding the quasi-ballistic phonon transport regime, where a lack of scattering results in the loss of local thermal equilibrium, and determining what we can learn from studying this regime. Ultimately, we showed that observations of quasi-ballistic transport can yield extremely useful information about phonon MFPs and their contribution to thermal conduction. In Chapter 3 we numerically investigated this regime using the frequency-dependent phonon Boltzmann transport equation, showing that studying how the transport deviates from diffusion theory can yield information about phonon relaxation times and MFPs. Chapter 4 briefly discussed the modifications that were made to the pump-probe system used in this work to experimentally study quasi-ballistic transport.

Chapters 5 introduced a new thermal conductivity spectroscopy technique which for the first time is able to measure MFPs relevant to thermal conduction across a wide range of length scales and materials. We demonstrated that by systematically changing the size of a focused beam at length scales comparable to MFPs and observing the change in thermal resistance, the thermal conductivity contributions from phonons of different MFPs can be determined. We presented the first experimental measurements of this distribution in silicon at cryogenic temperatures (30 K to 100 K).

In Chapter 6, we extended thermal conductivity spectroscopy to the nanoscale by observing heat transfer from lithographically patterned metallic light absorbers with diameters in the hundreds of nanometers range. Accessing this length range is important because many technologically relevant materials like thermoelectrics have MFPs in the deep submicron regime. We demonstrated this modified technique by measuring phonon MFPs in sapphire.

Considering the crucial importance of the knowledge of MFPs to understanding and engineering size effects, we expect the techniques developed in Chapters 5 and 6 to be useful for gaining a fundamental understanding of nanoscale heat transport, and for applications involving nanoscale thermal engineering such as thermoelectric materials and heat transfer in microelectronic devices.

7.2 Future work

One important conclusion of this thesis is that studying transport at the length and time scales of heat carriers yields far more detailed and useful information than can be obtained from a typical macroscopic measurement. In a sense, then, the work presented here is only the beginning because it describes the development and demonstration of one experiment which studies phonons at the MFP length scale, our thermal conductivity spectroscopy technique. With this particular technique, there is no shortage of interesting materials, both bulk and nanostructured, to which the technique can be applied; and there are many possibilities to study electrons, phonons, and photons at these same small scales to reveal interesting and useful results.

The future work for thermal conductivity spectroscopy consists of measuring MFPs for increasingly complex materials. The simplest next step would be to perform a similar analysis as was done for silicon to other materials which have suitably long MFPs at low temperatures. Ideally, the material would be simple enough to permit a comparison of first-principles calculations and experimental results. III-V materials such as GaAs would be suitable for this purpose. Analyzing the differences between the MFP distributions of different materials can yield information about the scattering mechanisms such as phonon-phonon scattering in pure semiconductors.

Next, one can consider the effect of alloying or doping on the MFP distribution. For alloys, it is generally accepted that high frequency modes are strongly scattered and a larger fraction of the heat is conducted by low frequency, long MFP modes. Our technique should be able to confirm this picture and give an idea which MFPs are carrying the heat in alloys. This type of information would be very useful for thermoelectrics as they are almost always alloys.

After this, nanostructured materials can be investigated. It is believed that grain boundaries are effective in scattering long MFP phonons, but exactly which phonons are still carrying the heat in nanocomposite materials is not known. This type of investigation could give results which are very useful for thermoelectrics. By determining which phonon modes carry how much heat, we will be better able to determine

how to effectively scatter these modes and reduce the thermal conductivity. As discussed in chapter 1, a reduction in thermal conductivity will lead to an increase in energy conversion efficiency, assuming a minimal reduction in electrical properties.

At this point, when we start investigating materials with low thermal conductivities and short MFPs, an additional modification of the technique will be necessary. As discussed in Chapter 6, accessing short length scales optically requires using lithographically patterned nanodot absorbers. We used this technique to measure submicron MFPs in sapphire. An important detail of this technique is that these nanodot absorber arrays typically cover at most 25% of the sample surface area, assuming a 50% duty cycle in the X and Y directions. The reason this technique worked for sapphire is that sapphire is transparent to visible radiation, meaning the 75% of the pump and probe light which reached the sapphire was not absorbed and thus did not contribute to the measured signal. However, most materials of interest are opaque to visible radiation. If we apply this technique to silicon, for example, 75% of the signal will be due to silicon and only 25% will be due to the nanodot arrays. Since we do not know *a priori* what the signal from silicon will be, it is difficult to extract the desired dot signal from the total signal.

To overcome this problem, we have been investigating designing special nanodot arrays which are suitable for studying heat transfer but also have special optical properties which prevent the laser radiation from being absorbed by the substrate. One idea is to design a structure which has has a very high reflectance for a particular wavelength and polarization so that the incoming light is reflected before it can be absorbed by the substrate. Determining how we can achieve strongly confined heating despite the presence of a possibly absorbing substrate is an important hurdle which must be overcome.

For electrons, a technique called point contact spectroscopy,[101] similar to what has been developed here for phonons, may yield information about electron MFPs. This technique measures electrical conduction from nanometer-sized contacts which are shorter than electron MFPs. By analyzing the deviations in the resistance from the Ohm's law prediction, information about MFPs can be extracted. This technique

may be helpful in determining more directly than the models presented in Chapter 2 how electrons are affected by grain boundaries.

Apart from investigations of electron and phonon transport for thermoelectrics applications, an important result of this thesis is that the pump-probe technique is versatile and can be applied to many different experimental configurations. Traditionally, pump-probe for heat transfer applications was employed only to measure thermal conductivities and interface conductances of different bulk materials using the familiar metal film on substrate geometry; in chapter 6, we modified this geometry to measure heat transfer at the nanoscale using dot arrays. In this spirit, there are myriad possibilities for how the same experiment can be applied to yield novel and useful results. Some of the possibilities are using pump-probe to measure heat transport down ultra-drawn polymer chains, measuring boiling and condensation heat transfer at ultrafast timescales, and using AFM techniques with pump-probe to achieve true nanoscale spatial and ultrafast time resolution.

These are just a few of the possibilities which could yield important and useful information about nanoscale transport. As the length scales of technology continue to shrink, our ability to understand and engineer transport at these scales will become the enabling factor for future innovation. We hope that this thesis has given insight into thermal transport at the nanoscale and will be useful for engineering the next generation of nanostructured materials.

Appendix A

Numerical constants used in the nanocomposite model

Values of the parameters used for the calculation of the electronic and thermal properties using the Boltzmann transport equation in Chap. 2 are given here. All data are from Ref. [60] unless otherwise noted. While most values are taken directly from the literature, four parameters require some modification. The low frequency dielectric constant ϵ_{0r} needs to be increased from its literature value to reduce the strength of ionized impurity scattering. This is a common adjustment when ionized impurity scattering is a dominant scattering mechanism, and Vining[51] also performed this adjustment.

The second adjusted parameter is the non-parabolicity α of the X conduction band. This parameter is not known with certainty and is often adjusted to obtain a better fit. In this case, a value of $\alpha = 0.5\ eV^{-1}$ has been reported,[107] but we find that a higher value of $1.25\ eV^{-1}$ is necessary to explain the data.

The final adjusted parameters are the valence band deformation potential D_v and hole effective mass m_h^*. For the deformation potential, here is no clear consensus on the precise value, and reported values vary from 2.94 eV in Ref. [51] to 5 eV in Ref. [49]. We find that a value in the middle of these, 4.0 eV, is required to fit the data for our model.

The hole effective mass is difficult to define due to the warped shape of the heavy

hole band and perturbations from the split-off band. We find a value of $m_h^* = 1.2m_e$ is necessary to fit the data, similar to the value of $1.4m_e$ used by Vining[51] and consistent with Slack and Hussain's discussion.[52] As discussed in Sec. 2.5, a higher value of 1.55 m_e is necessary to explain the nanocomposite data.

The temperature dependence of the band gap $E_g(T)$ was accounted for using a curve fit from Ref. [108]. The fit is given as follows:

$$\begin{aligned} E_{g,Si} &= 1.1695 - 4.73 \times 10^{-4} T^2/(T + 636) \\ E_{g,Ge} &= 0.85 - 4.774 \times 10^{-4} T^2/(T + 235) \\ E_g(T) &= E_{g,Si}(1 - x) + E_{g,Ge}x - 0.4x(1 - x) \end{aligned} \tag{A.1}$$

Here T is in K and E_g is in eV.

Table A.1: Lattice parameters for $Si_{1-x}Ge_x$ used to calculate the lattice thermal conductivity.

Property	Symbol (Units)	Value	Comment
Lattice constant	a ($\AA$)	$5.431(1-x)+5.658x$	
Bulk modulus	C_1 (10^{10} N/m^2)	$9.8-2.3x$	
Debye temperature	Θ_D (K)	$640-266x$	
Density	ρ (kg/m^3)	$2329+3493x-499x^2$	
Ratio of normal to umklapp scattering	β	2.0	Ref. [65]
Anharmonicity (n-type)	γ	1.0	Ref. [65]
Anharmonicity (p-type)	γ	0.7	
Strain parameter	ϵ	100	Ref. [65]
Higher-order phonon scattering exponent	n	1.4	

Table A.2: Band structure parameters for $Si_{1-x}Ge_x$ used to calculate electrical properties.

Property	Symbol (Units)	Value	Comment
Electron longitudinal/transverse effective mass (X)	m_l^*/m_t^* (m_e)	0.92/0.19	
Electron longitudinal/transverse effective mass (L)	m_l^*/m_t^* (m_e)	1.59/0.082	
Energy gap between X and L	E_L (eV)	0.8	
Hole DOS effective mass (bulk/nano)	m_h^* (m_e)	1.2/1.55	Ref. [52]
Non-parabolicity of X	α (eV^{-1})	1.25	Ref. [107]: 0.5
Low frequency dielectric constant	ϵ_{0r} (ϵ_0)	21	Ref. [60]: $11.7 + 4.5x$; Ref. [51]: 27
Electron Acoustic Deformation Potential	D_A (eV)	9.0	Ref. [107]
Hole Acoustic Deformation Potential	D_v (eV)	4.0	Ref. [51]: 2.94; Ref. [49]: 5.0
Electron Optical Deformation Potential	D_o ($\times 10^{10} eV/m$)	$2.2(1-x)+5.5x$	Ref. [109]
Hole Optical Deformation Potential	D_{vo} ($\times 10^{10} eV/m$)	$2.2(1-x)+5.5x$	Ref. [109]
Optical phonon energy	$\hbar\omega_{op}$ (eV)	$0.0612(1-x)+0.03704x$	Ref. [109]

Appendix B

Derivation of the relation between transmissivity and interface conductance

Here we derive a relation between the transmission and reflection coefficients of an interface and the interface conductance G, defined as:

$$G = \frac{q}{\Delta T} \tag{B.1}$$

where q and ΔT are the heat flux and temperature drop across the interface, respectively. Assuming that the incoming distributions to the interface (or forward-going phonons at the left of the interface, and backward-going phonons at the right of the interface) have temperatures T_{e1} and T_{e2}, we can use the Landauer formalism to find the heat flux:

$$q = \frac{\int_0^{\omega_1} T_{12}(\omega) C_{\omega 1} v_{\omega 1} d\omega}{4} (T_{e1} - T_{e2}) \tag{B.2}$$

However, it is inconsistent to define the interface conductance based on the emitted phonon temperature. We instead need the equivalent equilibrium temperature of all the phonons, both forward- and backward-going, at each side of the interface. Once the equivalent equilibrium temperature is obtained, a consistent interface conductance

can be defined. Here we derive the necessary relations while accounting for the frequency dependence of the transmission coefficients.

Several approximations are necessary for this derivation. First, the known, incoming fluxes to the interface must have a thermal distribution characterized by temperatures T_{e1} and T_{e2}. These will be the emitted phonon temperatures. Second, we must linearize the equilibrium distribution; otherwise, there is no way to extract the temperature drop from the Bose-Einstein distribution. Finally, we assume elastic, diffuse scattering and neglect any type of mode conversion: phonons do not change frequency or polarization as they cross the interface, but are scattered equally in all directions.

The equilibrium distribution f_ω^0 is given by

$$f_\omega^0(T) = \frac{\hbar\omega D(\omega) f_{BE}(T)}{4\pi} \tag{B.3}$$

where $f_{BE}(T) = (\exp(\hbar\omega/k_B T) - 1)^{-1}$ is the Bose-Einstein distribution function, and T is the temperature of the distribution. The linearized relation is:

$$f_\omega^0(T) = \frac{\hbar\omega D(\omega) f_{BE}(T)}{4\pi} \approx f_\omega^0(T_0) + \frac{\hbar\omega D(\omega)}{4\pi} \left.\frac{\partial f_{BE}}{\partial T}\right|_{T_0} \cdot (T - T_0) = f_\omega^0(T_0) + \frac{C_\omega}{4\pi}\Delta T \tag{B.4}$$

We will define $f_{0\omega}^0 = f_\omega^0(T_0)$ and drop the Δ from ΔT. By the first approximation, the incoming distribution to the interface are:

$$f_{\omega 1}^+ = f_{0\omega 1}^0 + \frac{C_{\omega 1} T_{e1}}{4\pi} \tag{B.5}$$

$$f_{\omega 2}^- = f_{0\omega 2}^0 + \frac{C_{\omega 2} T_{e2}}{4\pi} \tag{B.6}$$

We can express the outgoing distributions $f_{\omega 2}^+$ and $f_{\omega 1}^-$ as the transmitted and reflected components of these distributions. We can write the energy balance as:

$$\int_0^1 f_{\omega 2}^+ v_{\omega 2} \mu d\mu = T_{12}(\omega) \int_0^1 f_{\omega 1}^+ v_{\omega 1} \mu d\mu - R_{21}(\omega) \int_{-1}^0 f_{\omega 2}^- v_{\omega 2} \mu d\mu \tag{B.7}$$

$$\int_{-1}^0 f_{\omega 1}^- v_{\omega 1} \mu d\mu = T_{21}(\omega) \int_{-1}^0 f_{\omega 2}^- v_{\omega 2} \mu d\mu - R_{12}(\omega) \int_0^1 f_{\omega 1}^+ v_{\omega 1} \mu d\mu \tag{B.8}$$

Because the incoming distributions are independent of angle and we assume diffuse scattering, none of the distributions are angle-dependent. The angle integration will just give a factor of 1/2 which will cancel. The minus sign in front of the reflection coefficients accounts for the fact that the reflected heat flux changes direction. Inserting the thermal distributions and carrying out the angle integrations gives:

$$f^{+}_{\omega 2} v_{\omega 2} = T_{12}(\omega)\left(f^{0}_{0\omega 1} + \frac{C_{\omega 1} T_{e1}}{4\pi}\right) v_{\omega 1} + R_{21}(\omega)\left(f^{0}_{0\omega 2} + \frac{C_{\omega 2} T_{e2}}{4\pi}\right) v_{\omega 2} \quad \text{(B.9)}$$

$$f^{-}_{\omega 1} v_{\omega 1} = T_{21}(\omega)\left(f^{0}_{0\omega 2} + \frac{C_{\omega 2} T_{e2}}{4\pi}\right) v_{\omega 2} + R_{12}(\omega)\left(f^{0}_{0\omega 1} + \frac{C_{\omega 1} T_{e1}}{4\pi}\right) v_{\omega 1} \quad \text{(B.10)}$$

We now have expressions for both the forward- and backward-going fluxes at each side of the interface, which are highly non-equilibrium. The next step is to find the equivalent equilibrium temperature on each side of the interface. To do this, we first find the total energy density on each side of the interface. For side 1:

$$\frac{1}{2}\int_0^{\omega_1}\int_{-1}^{1} f_{\omega 1} v_{\omega 1} d\mu d\omega = \frac{1}{2}\int_0^{\omega_1}\left[\left(f^{0}_{0\omega 1} v_{\omega 1} + \frac{C_{\omega 1} v_{\omega 1} T_{e1}}{4\pi}\right)\right. \quad \text{(B.11)}$$

$$\left. + \frac{1}{2}\left(R_{12}(\omega) f^{0}_{0\omega 1} v_{\omega 1} + \frac{R_{12}(\omega) C_{\omega 1} v_{\omega 1} T_{e1}}{4\pi}\right) + \frac{1}{2}\left(T_{21}(\omega) f^{0}_{0\omega 2} v_{\omega 2} + \frac{T_{21}(\omega) C_{\omega 2} v_{\omega 2} T_{e2}}{4\pi}\right)\right] d\omega$$

To simplify this expression, we can use the principle of detailed balance and conservation of energy, which restricts the values of the transmission and reflection coefficients. The principle of detailed balance requires:

$$T_{12}(\omega)\left(f^{0}_{0\omega 1} + \frac{C_{\omega 1} T}{4\pi}\right) v_{\omega 1} = T_{21}(\omega)\left(f^{0}_{0\omega 2} + \frac{C_{\omega 2} T}{4\pi}\right) v_{\omega 2} \quad \text{(B.12)}$$

Conservation of energy requires:

$$R_{12}(\omega) = 1 - T_{12}(\omega) \quad \text{(B.13)}$$

$$R_{21}(\omega) = 1 - T_{21}(\omega) \quad \text{(B.14)}$$

These equations apply at each frequency. We can use $R_{12}(\omega) = 1 - T_{12}(\omega)$ in the second term of eq. B.11 and the principle of detailed balance in the third term. Now,

we also introduce the equivalent equilibrium temperature of the distribution of side 1 of the interface:

$$f_{\omega 1} = f^0_{0\omega 1} + \frac{C_{\omega 1} T_1}{4\pi} \tag{B.15}$$

Using these 3 relations, eq. B.11 becomes:

$$\int_0^{\omega_1} \left(\underline{f^0_{0\omega 1}} + \frac{C_{\omega 1} T_1}{4\pi} \right) v_{\omega 1} d\omega = \frac{1}{2} \int_0^{\omega_1} \left[\left(\underline{f^0_{0\omega 1} v_{\omega 1}} + \frac{\overbrace{C_{\omega 1} v_{\omega 1} T_{e1}}}{4\pi} \right) \right. \tag{B.16}$$

$$\left. + \frac{1}{2} \left((\underbrace{1 - T_{12}(\omega)}) f^0_{0\omega 1} v_{\omega 1} + \frac{(\overbrace{1} - T_{12}(\omega)) C_{\omega 1} v_{\omega 1} T_{e1}}{4\pi} \right) + \frac{1}{2} \left(\underbrace{T_{12}(\omega) f^0_{0\omega 1} v_{\omega 1}} + \frac{T_{12}(\omega) C_{\omega 1} v_{\omega 1} T_{e2}}{4\pi} \right) \right] d\omega$$

The underscored terms cancel while the overscored terms combine. This gives:

$$\int_0^{\omega_1} \frac{C_{\omega 1} v_{\omega 1} T_1}{4\pi} d\omega = \int_0^{\omega_1} \left[\frac{C_{\omega 1} v_{\omega 1} T_{e1}}{4\pi} - \frac{1}{2} \frac{T_{12}(\omega) C_{\omega 1} v_{\omega 1}}{4\pi} (T_{e1} - T_{e2}) \right] d\omega \tag{B.17}$$

$$T_1 = T_{e1} - \frac{1}{2} \frac{\langle T_{12}(\omega) C_1 v_1 \rangle}{\langle C_1 v_1 \rangle} (T_{e1} - T_{e2}) \tag{B.18}$$

The procedure for side 2 of the interface is exactly the same, giving an equation for the equivalent equilibrium temperature T_2:

$$T_2 = T_{e2} + \frac{1}{2} \frac{\langle T_{21}(\omega) C_2 v_2 \rangle}{\langle C_2 v_2 \rangle} (T_{e1} - T_{e2}) \tag{B.19}$$

To get the interface conductance G, we need to get the equivalent equilibrium temperature difference, obtained by subtracting the above equations:

$$T_1 - T_2 = (T_{e1} - T_{e2}) \left[1 - \frac{1}{2} \left(\frac{\langle T_{12}(\omega) C_1 v_1 \rangle}{\langle C_1 v_1 \rangle} + \frac{\langle T_{21}(\omega) C_2 v_2 \rangle}{\langle C_2 v_2 \rangle} \right) \right] \tag{B.20}$$

If the transmission coefficients are frequency-independent this formula reduces to that given in previous works.

The final step is to eliminate either $T_{12}(\omega)$ or $T_{21}(\omega)$ from the equation, leaving the interface conductance as a function of a single transmission coefficient. This can be achieved using the principle of detailed balance. In order for this procedure to be possible, it is necessary to use the principle of detailed balance at a single temperature

T_0, giving

$$T_{12}(\omega) f^0_{0\omega 1} v_{\omega 1} = T_{21}(\omega) f^0_{0\omega 2} v_{\omega 1} \tag{B.21}$$

While this relation does depend on temperature, the temperature differences considered here are so small that it is almost exact to assume the form given above. Then,

$$\int_0^{\omega_2} T_{21}(\omega) C_{\omega 2} v_{\omega 2} d\omega = \int_0^{\omega_2} T_{12}(\omega) \frac{f^0_{0\omega 1}}{f^0_{0\omega 2}} v_{\omega 1} C_{\omega 2} d\omega = \int_0^{\omega_2} T_{12}(\omega) C_{\omega 1} v_{\omega 1} d\omega \tag{B.22}$$

since $C_{\omega 1} = f^0_{0\omega 1} / f^0_{0\omega 2} C_{\omega 2}$. The transmissivity $T_{12}(\omega)$ restricts the range of the integration to those frequencies common between the two materials, making the limit of integration irrelevant. Now, we can relate G and $T_{12}(\omega)$:

$$q = \frac{\langle T_{12}(\omega) C_1 v_1 \rangle}{4} \frac{\Delta T}{1 - \frac{1}{2}\left(\frac{\langle T_{12}(\omega) C_1 v_1 \rangle}{\langle C_1 v_1 \rangle} + \frac{\langle T_{12}(\omega) C_1 v_1 \rangle}{\langle C_2 v_2 \rangle} \right)} = G \Delta T \tag{B.23}$$

Solving for $T_{12}(\omega)$:

$$\langle T_{12}(\omega) C_1 v_1 \rangle = \frac{2}{\frac{1}{<Cv>_1} + \frac{1}{<Cv>_2} + \frac{1}{2G}} \tag{B.24}$$

If we let $T_{12}(\omega)$ be a constant for those frequencies that transmit and zero otherwise, we arrive at the final formula:

$$T_{12}(\omega) = \frac{2 / \langle Cv \rangle'_1}{\frac{1}{<Cv>_1} + \frac{1}{<Cv>_2} + \frac{1}{2G}} \tag{B.25}$$

where $\langle Cv \rangle'_1$ denotes integration over only those frequencies which have non-zero transmissivity. The transmissivity is a constant for those frequencies in common between the two sides and zero otherwise. However, $T_{21}(\omega)$ is in general frequency dependent because of the principle of detailed balance at each frequency.

Bibliography

[1] David G. Cahill, Wayne K. Ford, Kenneth E. Goodson, Gerald D. Mahan, Arun Majumdar, Humphrey J. Maris, Roberto Merlin, and Simon R. Phillpot. Nanoscale thermal transport. *Journal of Applied Physics*, 93(2):793–818, 2003.

[2] M. S. Dresselhaus, G. Chen, M. Y. Tang, R. G. Yang, H. Lee, D. Z. Wang, Z. F. Ren, J.-P. Fleurial, and P. Gogna. New directions for low-dimensional thermoelectric materials. *Advanced Materials*, 19(8):1043–1053, 2007.

[3] L.D. Hicks and M. Dresselhaus. Thermoelectric figure of merit of a one-dimensional conductor. *Physical Review B*, 47:16631–16634, 1993.

[4] G. Chen and A. Shakouri. Heat transfer in nanostructures for solid-state energy conversion. *Journal of Heat Transfer*, 124(2):242–252, 2002.

[5] R. Venkatasubramanian. Phonon blocking electron transmitting superlattice structures as advanced thin film thermoelectric materials. In *Recent Trends in Thermoelectric Materials Research III*, volume 71 of *Semiconductors and Semimetals*, pages 175–201. Academic Press, 2001.

[6] G. Chen. Phonon transport in low-dimensional structures. In *Recent Trends in Thermoelectric Materials Research III*, volume 71 of *Semiconductors and Semimetals*, pages 203–259. Academic Press, 2001.

[7] Gang Chen. Thermal conductivity and ballistic phonon transport in cross-plane direction of superlattices. *Physical Review B*, 57(23):14958–14973, 1998.

[8] G. Chen. Nonlocal and nonequilibrium heat conduction in the vicinity of nanoparticles. *Journal of Heat Transfer*, 118(3):539–545, 1996.

[9] G. D. Mahan and J. O. Sofo. The best thermoelectric. *Proceedings of the National Academy of Sciences of the United States of America*, 93(15):7436–7439, 1996.

[10] Rama Venkatasubramanian, Edward Siivola, Thomas Colpitts, and Brooks O'Quinn. Thin-film thermoelectric devices with high room-temperature figures of merit. *Nature*, 413(6856):597–602, 2001.

[11] T. C. Harman, P. J. Taylor, M. P. Walsh, and B. E. LaForge. Quantum dot superlattice thermoelectric materials and devices. *Science*, 297(5590):2229–2232, 2002.

[12] Allon I. Hochbaum, Renkun Chen, Raul Diaz Delgado, Wenjie Liang, Erik C. Garnett, Mark Najarian, Arun Majumdar, and Peidong Yang. Enhanced thermoelectric performance of rough silicon nanowires. *Nature*, 451(7175):163–167, 2008.

[13] Akram I. Boukai, Yuri Bunimovich, Jamil Tahir-Kheli, Jen-Kan Yu, William A. Goddard III, and James R. Heath. Silicon nanowires as efficient thermoelectric materials. *Nature*, 451(7175):168–171, 2008.

[14] Bed Poudel, Qing Hao, Yi Ma, Yucheng Lan, Austin Minnich, Bo Yu, Xiao Yan, Dezhi Wang, Andrew Muto, Daryoosh Vashaee, Xiaoyuan Chen, Junming Liu, Mildred S. Dresselhaus, Gang Chen, and Zhifeng Ren. High-thermoelectric performance of nanostructured bismuth antimony telluride bulk alloys. *Science*, 320(5876):634–638, 2008.

[15] Yi Ma, Qing Hao, Bed Poudel, Yucheng Lan, Bo Yu, Dezhi Wang, Gang Chen, and Zhifeng F Ren. Enhanced thermoelectric figure-of-merit in p-type nanostructured bismuth antimony tellurium alloys made from elemental chunks. *Nano Lett.*, 8(8):2580–2584, 2008.

[16] X. W. Wang, H. Lee, Y. C. Lan, G. H. Zhu, G. Joshi, D. Z. Wang, J. Yang, A. J. Muto, M. Y. Tang, J. Klatsky, S. Song, M. S. Dresselhaus, G. Chen, and Z. F. Ren. Enhanced thermoelectric figure of merit in nanostructured n-type silicon germanium bulk alloy. *Applied Physics Letters*, 93(19):193121–3, 2008.

[17] Giri Joshi, Hohyun Lee, Yucheng Lan, Xiaowei Wang, Gaohua Zhu, Dezhi Wang, Ryan W. Gould, Diana C. Cuff, Ming Y. Tang, Mildred S. Dresselhaus, Gang Chen, and Zhifeng Ren. Enhanced thermoelectric figure-of-merit in nanostructured p-type silicon germanium bulk alloys. *Nano Letters*, 8(12): 4670–4674, 2008.

[18] George S. Nolas, Jeffrey Sharp, and H.J. Goldsmid. *Thermoelectrics: Basic Principles and New Materials Developments.* Springer, New York, 2001.

[19] D.M. Rowe, editor. *Thermoelectrics Handbook: Macro to Nano.* CRC Press, Boca Raton, 2006.

[20] Terry M. Tritt and M. A. Subramanian. Thermoelectric materials, phenomena, and applications : A bird's eye view. *MRS Bulletin*, 31(3):188–194, 2006.

[21] Terry M. Tritt, editor. *Recent Trends in Thermoelectric Materials Research*, volume 69-71 of *Semiconductors and Semimetals.* Academic Press, San Diego, 2001.

[22] G. Chen, M. S. Dresselhaus, G. Dresselhaus, J. P. Fleurial, and T. Caillat. Recent developments in thermoelectric materials. *International Materials Reviews*, 48:45–66, 2003.

[23] A. J. Minnich, M. S. Dresselhaus, Z. F. Ren, and G. Chen. Bulk nanostructured thermoelectric materials: Current research and future prospects. *Energy & Environmental Science*, 2(5):466 – 479, 2009.

[24] Lon E. Bell. Cooling, heating, generating power, and recovering waste heat with thermoelectric systems. *Science*, 321(5895):1457–1461, 2008.

[25] J. Yang. Potential applications of thermoelectric waste heat recovery in the automotive industry. In *24th International Conference on Thermoelectrics*, pages 170–174, 2005.

[26] http://upload.wikimedia.org/wikipedia/commons/5/54/llnl_us_energy_flow_2009.png. accessed december 2010.

[27] H. Scherrer, L. Vikhor, B. Lenoir, A. Dauscher, and P. Poinas. Solar thermolectric generator based on skutterudites. *Journal of Power Sources*, 115(1): 141–148, 2003.

[28] Hongxia Xi, Lingai Luo, and Gilles Fraisse. Development and applications of solar-based thermoelectric technologies. *Renewable and Sustainable Energy Reviews*, 11(5):923–936, 2007.

[29] S. Maneewan, J. Hirunlabh, J. Khedari, B. Zeghmati, and S. Teekasap. Heat gain reduction by means of thermoelectric roof solar collector. *Solar Energy*, 78 (4):495–503, 2005.

[30] S. Maneewan, J. Khedari, B. Zeghmati, J. Hirunlabh, and J. Eakburanawat. Investigation on generated power of thermoelectric roof solar collector. *Renewable Energy*, 29(5):743–752, 2004.

[31] Pierre F. P. Poudeu, Jonathan D'Angelo, Adam D. Downey, Jarrod L. Short, Timothy P. Hogan, and Mercouri G. Kanatzidis. High thermoelectric figure of merit and nanostructuring in bulk p-type $na_{1-x}pb_msb_yte_{m+2}$. *Angewandte Chemie International Edition*, 45(23):3835–3839, 2006.

[32] J. Androulakis, C. H. Lin, H. J. Kong, C. Uher, C. I. Wu, T. Hogan, B. A. Cook, T. Caillat, K. M. Paraskevopoulos, and M. G. Kanatzidis. Spinodal decomposition and nucleation and growth as a means to bulk nanostructured thermoelectrics: Enhanced performance in $pb_{1-x}sn_x$te-pbs. *J. Am. Chem. Soc.*, 129(31):9780–9788, 2007.

[33] Joseph P. Heremans, Vladimir Jovovic, Eric S. Toberer, Ali Saramat, Ken Kurosaki, Anek Charoenphakdee, Shinsuke Yamanaka, and G. Jeffrey Snyder. Enhancement of thermoelectric efficiency in pbte by distortion of the electronic density of states. *Science*, 321(5888):554–557, 2008.

[34] Joseph R. Sootsman, Huijun Kong, Ctirad Uher, Jonathan James D'Angelo, Chun-I Wu, Timothy P. Hogan, Thierry Caillat, and Mercouri G. Kanatzidis. Large enhancements in the thermoelectric power factor of bulk pbte at high temperature by synergistic nanostructuring. *Angewandte Chemie*, 120(45):8746–8750, 2008.

[35] Allon I. Hochbaum, Renkun Chen, Raul Diaz Delgado, Wenjie Liang, Erik C. Garnett, Mark Najarian, Arun Majumdar, and Peidong Yang. Enhanced thermoelectric performance of rough silicon nanowires. *Nature*, 451(7175):163–167, 2008.

[36] G. Pernot, M. Stoffel, I. Savic, F. Pezzoli, P. Chen, G. Savelli, A. Jacquot, J. Schumann, U. Denker, I. Mönch, Ch Deneke, O. G. Schmidt, J. M. Rampnoux, S. Wang, M. Plissonnier, A. Rastelli, S. Dilhaire, and N. Mingo. Precise control of thermal conductivity at the nanoscale through individual phonon-scattering barriers. *Nature Materials*, 9(6):491–495, 2010.

[37] M. M. Mandurah, K. C. Saraswat, and T. I. Kamins. A model for conduction in polycrystalline silicon;part i: Theory. *Electron Devices, IEEE Transactions on*, 28(10):1163–1171, 1981.

[38] D. P. Joshi and R. S. Srivastava. A model of electrical conduction in polycrystalline silicon a model of electrical conduction in polycrystalline silicon. *Electron Devices, IEEE Transactions on*, 31(7):920–927, 1984.

[39] M. K. Sharma and D. P. Joshi. Electrical conduction model for polycrystalline gaas films. *Journal of Applied Physics*, 102(3):033704–7, 2007.

[40] Daryoosh Vashaee and Ali Shakouri. Electronic and thermoelectric transport in semiconductor and metallic superlattices. *Journal of Applied Physics*, 95(3): 1233–1245, 2004.

[41] Joseph Callaway. Model for lattice thermal conductivity at low temperatures. *Phys. Rev.*, 113(4):1046–1051, Feb 1959.

[42] M. G. Holland. Analysis of lattice thermal conductivity. *Phys. Rev.*, 132(6): 2461–2471, Dec 1963.

[43] Ronggui Yang, Gang Chen, and Mildred Dresselhaus. Thermal conductivity modeling of core-shell and tubular nanowires. *Nano Letters*, 5:1111, 2005.

[44] Ronggui Yang, Gang Chen, and Mildred Dresselhaus. Thermal conductivity of simple and tubular nanowire composites in longitudinal direction. *Physical Review B*, 72:125418, 2005.

[45] J. R. Sootsman, R. J. Pcionek, H. Kong, C. Uher, and M. G. Kanatzidis. Strong reduction of thermal conductivity in nanostructured pbte prepared by matrix encapsulation. *Chem. Mater.*, 18(21):4993–4995, 2006.

[46] Kuei Fang Hsu, Sim Loo, Fu Guo, Wei Chen, Jeffrey S. Dyck, Ctirad Uher, Tim Hogan, E. K. Polychroniadis, and Mercouri G. Kanatzidis. Cubic agpbms-bte2+m: Bulk thermoelectric materials with high figure of merit. *Science*, 303 (5659):818–821, 2004.

[47] Gang Chen. *Nanoscale Energy Transport and Conversion.* Oxford University Press, New York, 2005.

[48] Mark Lundstrom. *Fundamentals of Carrier Transport.* Cambridge University Press, Cambridge, 2nd edition, 2000.

[49] Jasprit Singh. *Physics of Semiconductors and their Heterostructures.* McGraw-Hill, Singapore, 1996.

[50] B. R. Nag. *Electron Transport in Compound Semiconductors*, volume 11 of *Springer Series in Solid-State Sciences.* Springer, New York, 1980.

[51] Cronin B. Vining. A model for the high-temperature transport properties of heavily doped n-type silicon-germanium alloys. *Journal of Applied Physics*, 69 (1):331–341, 1991.

[52] Glen A. Slack and Moayyed A. Hussain. The maximum possible conversion efficiency of silicon-germanium thermoelectric generators. *Journal of Applied Physics*, 70(5):2694–2718, 1991.

[53] A. F. Mayadas and M. Shatzkes. Electrical-resistivity model for polycrystalline films: the case of arbitrary reflection at external surfaces. *Physical Review B*, 1(4):1382, 1970.

[54] B. M. Askerov. *Electron Transport Phenomena in Semiconductors.* World Scientific Publishing Co., Singapore, 1994.

[55] Yu. I. Ravich, B. A. Efimova, and V. I. Tamarchenko. Scattering of current carriers and transport phenomena in lead chalcogenides. *Physica Status Solidi (b)*, 43(1):11–33, 1971.

[56] V. S. Shukla and D. M. Rowe. Precipitation of boron from silicon-germanium alloy and its effect in the thermoelectric transport properties. *Physica Status Solidi (a)*, 66(1):243–248, 1981.

[57] D. M. Rowe and N. Savvides. The reversal of precipitation in heavily doped silicon-germanium alloys. *Journal of Physics D Applied Physics*, 12:1613–1619, September 1979.

[58] N Savvides and D M Rowe. Precipitation of phosphorus from solid solutions in si-ge alloys and its effect on thermoelectric transport properties. *Journal of Physics D: Applied Physics*, 14(4):723–732, 1981.

[59] Austin Minnich. Modeling the Thermoelectric Properties of Bulk and Nanocomposite Thermoelectric Materials. Master's thesis, Massachusetts Institute of Technology, Cambridge, MA, May 2008.

[60] http://www.ioffe.rssi.ru/sva/nsm/semicond/index.html. accessed april 2008.

[61] Yu. I. Ravich, B. A. Efimova, and I. A. Smirnov. *Semiconducting Lead Chalcogenides*, volume 5 of *Monographs in Semiconductor Physics*. Plenum Press, New York, 1970.

[62] Simon Sze. *Physics of Semiconductor Devices*. John Wiley and Sons, Inc., New York, 2nd edition, 1981.

[63] D. L. Rode. Electron mobility in direct-gap polar semiconductors. *Physical Review B*, 2(4):1012, 1970.

[64] Andreas Schenk. *Advanced Physical Models for Silicon Device Simulation*. Computational Microelectronics. Springer, New York, 1998.

[65] E. F. Steigmeier and B. Abeles. Scattering of phonons by electrons in germanium-silicon alloys. *Physical Review*, 136(4A):A1149, 1964.

[66] J. P. Dismukes, L. Ekstrom, E. F. Steigmeier, I. Kudman, and D. S. Beers. Thermal and electrical properties of heavily doped ge-si alloys up to 1300[degree]k. *Journal of Applied Physics*, 35(10):2899–2907, 1964.

[67] T. I. Kamins. Hall mobility in chemically deposited polycrystalline silicon. *Journal of Applied Physics*, 42(11):4357–4365, 1971.

[68] John Y. W. Seto. The electrical properties of polycrystalline silicon films. *Journal of Applied Physics*, 46(12):5247–5254, 1975.

[69] C. R. M. Grovenor. Grain boundaries in semiconductors. *Journal of Physics C: Solid State Physics*, 18(21):4079–4119, 1985.

[70] Mildred S Dresselhaus, Gang Chen, Zhifeng F Ren, Jean-Pierre Fleurial, Pawan Gogna, Ming Y Tang, Daryoosh Vashaee, Hohyun Lee, Xiaowei Wang, Giri Joshi, Gaohua Zhu, Dezhi Wang, Richard Blair, Sabah Bux, and Richard Kaner. Nanocomposites to enhance zt in thermoelectrics. In *Proceedings of the MRS Fall Meeting*, pages 1044–U02–04, 2007.

[71] Ming-Shan Jeng, Ronggui Yang, David Song, and Gang Chen. Modeling the thermal conductivity and phonon transport in nanoparticle composites using Monte Carlo simulation. *Journal of Heat Transfer*, 130(4):042410–11, 2008.

[72] Ravi Prasher. Thermal conductivity of composites of aligned nanoscale and microscale wires and pores. *Journal of Applied Physics*, 100:034307, 2006.

[73] Ravi Prasher. Transverse thermal conductivity of porous materials made from aligned nano- and microcylindrical pores. *Journal of Applied Physics*, 100: 064302, 2006.

[74] Woochul Kim, Joshua Zide, Arthur Gossard, Dmitri Klenov, Susanne Stemmer, Ali Shakouri, and Arun Majumdar. Thermal conductivity reduction and thermoelectric figure of merit increase by embedding nanoparticles in crystalline semiconductors. *Physical Review Letters*, 96(4):045901–4, 2006.

[75] A. Khitun, K. L. Wang, and G. Chen. Thermoelectric figure of merit enhancement in a quantum dot superlattice. *Nanotechnology*, 11(4):327, 2000.

[76] Austin Minnich and Gang Chen. Modified effective medium formulation for the thermal conductivity of nanocomposites. *Applied Physics Letters*, 91(7): 073105–3, 2007.

[77] S.K. Chun and K.L. Wang. Effective mass and mobility of holes in strained $si_{1-x}ge_x$ layers on (001) $si_{1-y}ge_y$ substrate. *Electron Devices, IEEE Transactions on*, 39(9):2153–2164, Sep 1992.

[78] R. J. von Gutfeld and A. H. Nethercot. Heat pulses in quartz and sapphire at low temperatures. *Phys. Rev. Lett.*, 12(23):641–644, Jun 1964.

[79] Eric Pop and Kenneth E. Goodson. Thermal phenomena in nanoscale transistors. *Journal of Electronic Packaging*, 128(2):102–108, 2006.

[80] David G. Cahill. Analysis of heat flow in layered structures for time-domain thermoreflectance. *Review of Scientific Instruments*, 75(12):5119–5122, 2004.

[81] A. Majumdar. Microscale heat conduction in dielectric thin films. *Journal of Heat Transfer*, 115(1):7–16, 1993.

[82] A. A. Joshi and A. Majumdar. Transient ballistic and diffusive phonon heat transport in thin films. *Journal of Applied Physics*, 74(1):31–39, 1993.

[83] Sreekant V. J. Narumanchi, Jayathi Y. Murthy, and Cristina H. Amon. Submicron heat transport model in silicon accounting for phonon dispersion and polarization. *Journal of Heat Transfer*, 126(6):946–955, 2004.

[84] S. Sinha and K.E. Goodson. Thermal conduction in sub-100 nm transistors. *Microelectronics Journal*, 37(11):1148 – 1157, 2006.

[85] Qing Hao, Gang Chen, and Ming-Shan Jeng. Frequency-dependent monte carlo simulations of phonon transport in two-dimensional porous silicon with aligned pores. *Journal of Applied Physics*, 106(11):114321, 2009.

[86] A. Ward and D. A. Broido. Intrinsic phonon relaxation times from first-principles studies of the thermal conductivities of si and ge. *Phys. Rev. B*, 81(8):085205, Feb 2010.

[87] Arun Majumdar and Pramod Reddy. Role of electron–phonon coupling in thermal conductance of metal–nonmetal interfaces. *Applied Physics Letters*, 84(23): 4768–4770, 2004.

[88] Per G. Sverdrup, Y. Sungtaek Ju, and Kenneth E. Goodson. Sub-continuum simulations of heat conduction in silicon-on-insulator transistors. *Journal of Heat Transfer*, 123(1):130–137, 2001.

[89] P. G. Klemens. Anharmonic decay of optical phonons. *Phys. Rev.*, 148(2): 845–848, Aug 1966.

[90] E. T. Swartz and R. O. Pohl. Thermal boundary resistance. *Rev. Mod. Phys.*, 61(3):605–668, Jul 1989.

[91] Asegun S. Henry and Gang Chen. Spectral phonon transport properties of silicon based on molecular dynamics simulations and lattice dynamics. *Journal of Computational and Theoretical Nanoscience*, 5:141–152, 2008.

[92] http://refractiveindex.info/?group=metals&material=aluminium. accessed september 2010.

[93] Mark E. Siemens, Qing Li, Ronggui Yang, Keith A. Nelson, Erik H. Anderson, Margaret M. Murnane, and Henry C. Kapteyn. Quasi-ballistic thermal transport from nanoscale interfaces observed using ultrafast coherent soft x-ray beams. *Nature Materials*, 9(1):26–30, 2009.

[94] Yee Kan Koh and David G. Cahill. Frequency dependence of the thermal conductivity of semiconductor alloys. *Physical Review B (Condensed Matter and Materials Physics)*, 76(7):075207, 2007.

[95] Aaron J. Schmidt, Xiaoyuan Chen, and Gang Chen. Pulse accumulation, radial heat conduction, and anisotropic thermal conductivity in pump-probe transient thermoreflectance. *Review of Scientific Instruments*, 79(11):114902, 2008.

[96] Aaron Schmidt. *Optical Characterization of Thermal Transport from the Nanoscale to the Macroscale.* PhD thesis, Massachusetts Institute of Technology, 2008. Accumulation formulae: starting p56 Filter in front of detector if probably FGL495.

[97] *SR844 Lock in Manual.*

[98] William S. C. Chang. *Principles of Lasers and Optics.* Cambridge University Press, 2005.

[99] A. D. Christianson, M. D. Lumsden, O. Delaire, M. B. Stone, D. L. Abernathy, M. A. McGuire, A. S. Sefat, R. Jin, B. C. Sales, D. Mandrus, E. D. Mun, P. C. Canfield, J. Y. Y. Lin, M. Lucas, M. Kresch, J. B. Keith, B. Fultz, E. A. Goremychkin, and R. J. McQueeney. Phonon density of states of $lafeaso_{1-x}f_x$. *Phys. Rev. Lett.*, 101(15):157004, Oct 2008.

[100] M. Highland, B. C. Gundrum, Yee Kan Koh, R. S. Averback, David G. Cahill, V. C. Elarde, J. J. Coleman, D. A. Walko, and E. C. Landahl. Ballistic-phonon heat conduction at the nanoscale as revealed by time-resolved x-ray diffraction and time-domain thermoreflectance. *Phys. Rev. B*, 76(7):075337, Aug 2007.

[101] Guy Deutscher. Coherence and single-particle excitations in the high-temperature superconductors. *Nature*, 397(6718):410–412, 1999.

[102] A. V. Inyushkin, A. N. Taldenkov, A. M. Gibin, A. V. Gusev, and H. J. Pohl. On the isotope effect in thermal conductivity of silicon. *physica status solidi (c)*, 1(11):2995–2998, 2004.

[103] Keivan Esfarjani and Harold T. Stokes. Method to extract anharmonic force constants from first principles calculations. *Phys. Rev. B*, 77(14):144112, Apr 2008.

[104] C. Dames and G. Chen. Thermal conductivity of nanostructured thermoelectric materials. In D. Rowe, editor, *CRC Thermoelectrics Handbook: Macro to Nano.* CRC Press, 2005.

[105] H.S. Carslaw and J.C. Jaeger. *Conduction of Heat in Solids.* Oxford University Press, Oxford, 2nd edition, 1959.

[106] Larry C Andrews and Bhimsen K Shivamoggi. *Integral Transforms for Engineers.* SPIE Optical Engineering Press, 1999.

[107] M. V. Fischetti and S. E. Laux. Monte carlo study of electron transport in silicon inversion layers. *Physical Review B*, 48(4):2244, 1993.

[108] Vassil Palankovski. *Simulation of Heterojunction Bipolar Transistors.* Phd, Technical University of Wien, 2000. URL `http://www.iue.tuwien.ac.at/phd/palankovski/node37.html`.

[109] http://www.iue.tuwien.ac.at/phd/smirnov/node54.html. accessed january 2009.